Title
The effect of constituent microstructure on the mechanical properties of bone

Author
Catanese, Joseph,

Publication Date
1998

Peer reviewed|Thesis/dissertation

The Effect of Constituent Microstructure on the Mechanical Properties of Bone

by

Joseph Catanese, III

B.S. (Cornell University, Ithaca, NY) 1993

DISSERTATION

Submitted in partial satisfaction of the requirements for the degree of

DOCTOR OF PHILOSOPHY

in

BIOENGINEERING

in the

GRADUATE DIVISIONS

of the

UNIVERSITY OF CALIFORNIA SAN FRANCISCO

and

UNIVERSITY OF CALIFORNIA BERKELEY

Date University Librarian

Degree Conferred: .....

Acknowledgments

This dissertation was completed with the help of many people, and I am grateful to all of them. I am especially indebted to my research advisor, Prof. Tony Keaveny, who has constantly challenged and encouraged me. Other faculty members of the joint bioengineering program have also provided valuable advice and support, especially Prof. John Featherstone, who advised me in the ultrastructural analysis in Chapter 3, and Professors Lisa Pruitt, Raj Bhatnagar, and Dr. Claude Arnaud. Special thanks is also due to Prof. Don Bartel of Cornell University, who introduced me to bioengineering and Debra Harris, who was a constant source of support during my tenure at the University of California.

My peers in both the Berkeley Orthopaedic Biomechanics Laboratory and the joint bioengineering program have also helped me in many ways. In particular, Erika Iverson has been very helpful in executing experiments and providing editorial advice on the manuscript. Additionally, discussions with Eric Nauman, Yves Arramon and Oscar Yeh, have provided valuable insight, especially into the continuum damage model. A number of undergraduates have also helped in various aspects of this work. Brian Canfield, Ramford Ng, Jim Sicurello and Steven Zadesky deserve special thanks for their efforts.

The ribose treatment and HPLC analysis included in chapters 5 and 6 was performed by Ruud Bank and Johan te Koppele at the Gaubius Laboratory at the Netherlands Organization for Applied Scientific Research. Their work was essential in completing this dissertation and I thank them both.

Much thanks is also due to my parents; for they have loved, encouraged, and supported me through all of my endeavors, and taught me how to learn.

Finally, thanks to Brandi, for helping me keep everything in perspective.

Abstract

The Effect of Constituent Microstructure on the Mechanical Properties of Bone

Joseph Catanese, III

Bone is a hierarchical composite material. Individual collagen molecules and hydroxyapatite crystals comprise the smallest hierarchical composite level, while dense cortical bone and highly porous trabecular bone together form whole bones, the largest hierarchical composite level. Many authors have investigated the role of the composite structure in the mechanical properties of bone, but the source of the elastic-plastic stress-strain behavior has not been explicitly identified. Understanding the structure-function relationship for bone tissue could have a substantial impact on drug design and diagnostics for bone health.

It has long been suggested that the elastic properties of bone are due to the hydroxyapatite component, while the ductility is due to the collagen component. The four experiments described in this dissertation demonstrate that this true. Bone with most of the organic component removed had the same elastic modulus as intact bone in both tension and compression, although the strength and ductility were compromised, especially in tension. Conversely, the ductility of both demineralized and intact bone was reduced by increasing the pentosidine cross-link density *in vitro*. Pentosidine cross-link density was also found to increase with age. This result indicates that collagen plays an important role in determining the ductility of bone and, more specifically, that age-related increases in collagen cross-linking may reduce the ductility of bone, thereby degrading bone quality.

A continuum damage model of cortical bone was also developed and used to investigate the role of microstructural elements such as osteons, Haversian canals and porosity, on the mechanical properties of bone. The model agreed with experimental

findings and indicated that 1) all mechanical properties decreased with increasing porosity; 2) elastic-plastic components (osteons and interstitial bone) were required in order to model the elastic-plastic behavior of cortical bone; and 3) the mechanical properties of osteons and interstitial bone may be substantially higher than the apparent properties measured experimentally.

Table of Contents

List of Tables

List of Figures

Chapter One. Introduction

Historical perspective

The importance of understanding the structure of the skeletal system was recognized by the early anatomists (1). Da Vinci was perhaps the first to investigate the relationship between the structure and function of the musculo-skeletal system. His dissections and observations lead him to conclude that the long bones acted like levers, amplifying forces generated by the muscles. Da Vinci also noted that the internal structure of some bones was spongy while that of others was not and suggested that this structure should be investigated further (2). Light and electron microscopy in combination with other analytical techniques have enabled the study of the structure of bone on smaller and smaller size scales over the last 300 years.

We now know that the spongy bone da Vinci observed was trabecular bone, which is a porous network of small rods and plates found in the ends of long bones such as the femur, in flat bones such as the ribs and in the vertebral bodies. The solid bone da Vinci observed was cortical bone, also called compact bone because it appears solid when observed without magnification, as da Vinci did. The orientation of the rods and plates within trabecular bone follows the principal orientation of the external loads applied to the whole bone (3). The mechanical properties of the tissue are greatest in the principal direction (4), indicating that the structure of trabecular bone at each anatomical site is optimized for the particular applied loads. In this sense, trabecular bone can be thought of as a structure of rods and plates, and the structure depends on parameters such as age, species and anatomic site. Both cortical and trabecular bone are built from a common material, referred to as bone tissue. Since cortical bone is dense and relatively free of pores, mechanical testing of small samples is generally considered to provide results representative of bone tissue.

The structure of cortical bone is still not completely understood (see Chapter 2) but it is known that it is a hierarchical composite material. The highest composite level of cortical bone—microstructure—is that of the thin sheets or lamellae which are arranged in

parallel and may be further arranged into concentric cylinders called osteons (5, 6). Many authors have used variations in bone microstructure to explain the natural variation in the mechanical properties of the tissue (7-16). Additionally, a smaller scale—ultrastructure, where mineral crystals are embedded in an array of collagen molecules—has also been used to explain variations in the mechanical properties of bone (17-19). At the ultrastructural level, it has been shown that the *amount* of mineral (as a fraction of the total mass of a test specimen) affects the mechanical properties (17-19). Thus it is reasonable to assume that the mechanical properties of bone will also depend on other features of the ultrastructure, including the mechanical properties and the spatial arrangement of the hydroxyapatite crystals and the collagen molecules.

Clinical need for understanding the mechanical properties in light of the structure

The current trend in pharmaceutical treatments for osteoporosis and other bone diseases involves increasing bone mass, but alternative strategies may be more effective. Drug-related increases in bone mass are often too small to significantly affect the mechanical properties of the bone and are generally lost soon after treatment ends. An alternative approach is to alter the quality of the tissue rather then its quantity. In this approach, the aim is to alter the structure of the collagen and hydroxyapatite that constitute the bone tissue in order to improve the response to mechanical loading.

Fundamental to this alternative approach is the understanding of both the structure and the mechanical properties of bone and, more importantly, how they relate. Aging causes changes in the amount and type of cross-linking in bone collagen (20) as well as the amount (21, 22) and stoichiometry (22) of bone hydroxyapatite. Additionally, the stiffness, strength, ductility and energy absorption of cortical bone all decrease with age (23). Since changes in the structure of a material often lead to changes in the mechanical properties, it is likely that these changes in bone or constituent structure will affect its mechanical properties. Thus, the aim of this dissertation is to elucidate the age-related changes in the

structure of the collagen and the hydroxyapatite and how these changes are manifested in the mechanical properties of bone tissue.

By understanding how the aging of bone constituents is manifested in the overall bone tissue properties, we can determine the mechanisms by which bone ages and by which drugs either increase or decrease the strength and ductility of bone tissue. For example, the hydroxyapatite is thought to determine the strength of bone, if this is true, then any drug treatment that adversely affects the strength of hydroxyapatite will have a substantial effect on overall strength. By contrast, treatments that affect the collagen may have little effect on the strength but play an important role in the ductility. The knowledge gained from understanding these mechanisms should: 1) enable development of more powerful drugs in the treatment of bone disease; 2) improve the characterization of new drug treatments before their use in clinical trials; 3) suggest new diagnostics to determine patients with a high risk of fracture; and 4) aid in the design of artificial bone substitutes which mimic the complex structure of natural bone.

Overview

The overall goal of this work is to relate changes in the constituent structure of bone to changes in the mechanical properties. There are six specific objectives to this work. One will be addressed in each subsequent chapter, they are:

1. Review the structure of cortical bone.
2. Compare the structure and mechanical properties of intact vs. deorganified bone in tension and compression.
3. Compare the mechanical properties of isolated bone collagen from different species and anatomical sites.
4. Compare the mechanical properties of untreated vs. cross-link enhanced isolated bovine and human bone collagen.
5. Compare the mechanical properties of untreated vs. cross-link enhanced human bone.

6. Develop and interpret a model of the mechanical properties of intact cortical bone based on its composite structure.

After addressing each of these objectives, I will discuss the implications of the results from both the experiments and the model, and propose experiments that can provide additional insight into the structure-function relationship of bone.

Chapter Two. The Structure of Bone

Introduction

Mammalian bone is one of the most complex structural materials in nature, with many different levels of organization. A detailed knowledge of the structure of bone is required to correctly interpret variations in measurements from mechanical testing experiments and to accurately model the mechanical properties of bone. In that context, the overall goal of this chapter is to review what is known about the different organizational levels of human cortical bone.

The extracellular matrix of bone is a hierarchical composite material. The basic constituents are: carbonated hydroxyapatite, a biomineral that provides strength and stiffness; collagen, an abundant fibrous protein responsible for the tensile properties of most load-bearing tissues; water; and small amounts of lipids, carbohydrates and non-collagenous proteins (Table 2.1). At the lowest composite level collagen acts as a matrix, surrounding hydroxyapatite crystals. The collagen molecules are arranged in a highly organized manner into fibrils, which become impregnated with and possibly surrounded by the hydroxyapatite crystals which stiffen and strengthen the collagenous matrix. At the next higher composite level, the mineralized collagen fibril acts as the fiber and is embedded in a matrix of non-collagenous organic components and additional mineral. These mineralized fibrils are arranged into parallel sheets (lamellae), which are stacked to form a plywood-like structure to form the third composite level. The stacked lamellae are arranged in different ways creating additional levels of composite structure, depending on the type of bone tissue. In mature human bone, the lamellae are often further arranged into concentric cylinders to form osteons.

Since the objective of this review is to describe bone structure in order to guide the development of a mechanical model of bone that is based on its structure, emphasis will be on the smallest level of composite structure, the collagen matrix embedded with mineral crystals. Thus, this review will focus on the structures of hydroxyapatite crystals and collagen molecules, and how they are arranged into mineralized fibrils. The arrangement of mineralized fibrils into lamellar sheets and osteons will also be described.

The Structure of Bone Mineral

The mineral in bone is an imperfect form of hydroxyapatite: $Ca_{10}(PO_4)_6(OH)_2$ (24). The large number of different ions that are substituted for those found in pure hydroxyapatite has made defining the structure of biological hydroxyapatite controversial. In addition to identifying the stoichiometry of biological apatite, much work has been devoted to determining the structure, shape and size of the crystals. Surprisingly little work has been directed at describing bone mineral at the polycrystalline level. There is little direct evidence to support either a monolithic (*i.e.* contiguous) or a discrete mineral phase, although most authors consider the mineral phase to be discreet.

Stoichiometry

The chemical structure for pure hydroxyapatite is $Ca_{10}(PO_4)_6(OH)_2$ (24), but biological hydroxyapatite differs considerably. The most commonly found ions substituted in bone mineral are sodium and potassium for calcium; carbonate and acid phosphate for phosphate; and fluoride and chloride for hydroxyl groups (Figure 2.1) (25). In particular, four carbonate ions often replace three phosphate ions, with the additional loss of two hydroxyl groups to preserve charge balance and for spatial concerns

(26). This substitution, combined with the common substitutions of fluoride and chloride for hydroxyl groups, has made it difficult to detect hydroxyl groups in bone mineral. It is thought therefore that hydroxyl ions are not present in measurable quantities in bone mineral (27). An alternative stoichiometry for bone mineral is $Ca_{8.3}(PO_4)_{4.3}(CO_3)_X(HPO_4)_Y(OH)_{0.3}$ where Y decreases and X increases with age but always sum to 1.7 (22). For example, the chemical formula of rat bone at birth is $Ca_{8.3}(PO_4)_{4.3}(CO_3)_{0.7}(HPO_4)_{1.0}(OH)_{0.3}$ compared to the carbonate rich formula obtained for one year old rats: $Ca_{8.3}(PO_4)_{4.3}(CO_3)_{1.2}(HPO_4)_{0.5}(OH)_{0.3}$ (22). Given the most common substitutions, a more appropriate name for bone mineral is "carbonate apatite containing acid phosphate groups" or simply "biological apatite" (28). For consistency however, the terms hydroxyapatite, bone mineral and mineral, will be used interchangeably throughout this dissertation to indicate biological apatite.

Crystallinity

Crystallinity is a general measure of non-stoichiometry, imperfections, and size of individual crystals (29). Crystallographically, bone mineral is a hexagonal rhombic prism (Figure 2.2) with symmetry in the a and b directions. X-ray diffraction measurements have demonstrated that the lattice spacing of apatite is between 9.37 Å (30) and 9.43 Å (24) in the a and b directions and 6.88 Å in the c direction (24). More recent transmission electron microscopy data agreed with the earlier x-ray diffraction measurements of the c direction spacing but revealed a lattice spacing of 8.17 Å in the a and b directions (Figure 2.3)(31). This discrepancy arises from the different definitions of the unit cell used in these studies (Figure 2.4). The earlier x-ray diffraction study considered a hexagonal unit

cell with hydroxyl groups in the center and on each corner of the unit cell (24, 30). Later studies using a transmission electron microscope revealed a simpler unit cell, a rhombic cell which is one-third of the volume of the original hexagonal cell (31).

Bone apatite differs from most other minerals, even other biominerals—like that found in mollusk shells—in that it has a high frequency of lattice imperfections. Most crystals have lattice imperfections (vacancies, substitutions or dislocations) approximately once in every 1000 lattice spaces; in bone mineral imperfections occur as frequently as once in every five to ten lattice spaces (29). In addition, the high level of imperfections in bone mineral increases its solubility, which allows rapid release of ions when they are needed for physiological processes.

Bone crystals are among the smallest biominerals known (32). Even though many investigators have viewed bone crystals with various methods, there is still controversy over the average size and shape of individual mineral crystals (Table 2.2). Knowledge of the size and shape of bone mineral crystals is important for mechanical modeling, since the hydroxyapatite crystals are thought to act as a short-fiber reinforcements embedded in a matrix of collagen, and fiber dimensions play an important role in determining the mechanical properties of a composite material (33-35). For a long time bone mineral crystals were thought to be long slender rods (36-38), although some authors did observe plate-shaped crystals (30, 39). More recent studies have demonstrated that crystals which appear as rods are actually plate-shaped crystals viewed edge-on (40-44). However, some authors have observed rod-shaped crystals in both longitudinal and cross-section (45) suggesting that both types of crystals may exist. The best estimates of average

crystal size are 350-500 Å long (in the crystallographic c direction), about 150 Å wide, and only 20-50 Å thick (Table 2.2). Since the a lattice spacing is 9.37 Å, the mineral crystals are only 2-5 unit cells thick.

Many of the discrepancies in crystal dimensions arise from artifacts associated with the different measurement techniques. The two greatest difficulties in measuring crystal sizes are preparing mineralized tissue for viewing in an electron microscope or other apparatus (which often involves dissolving the organic matrix surrounding the mineral) and ensuring correct alignment of the crystals (viewing a crystal off-axis will result in a two-dimensional projection that is a different size than any on-axis view of the same crystal). With these limitations in mind, the four different techniques that have been used to quantify the size of bone mineral crystals will be reviewed in an attempt to better understand the morphology of bone mineral in the context of bone as a composite material.

The first method used to prepare and view bone mineral crystals was to liberate the crystals from the collagenous matrix and view them in an electron microscope (29, 40, 46, 47). Mechanical grinding followed by chemical processing to denature the collagen fibrils is used to isolate the hydroxyapatite crystals. Sodium hypochlorite (household bleach) and various organic solvents are commonly used to denature the collagen. In this technique, the aqueous solvents used may lead to mineral phase dissolution and phase transformations (48). This would lead to larger average crystal sizes being reported since smaller crystals (*i.e.* those with a higher surface area to volume ratio) would be preferentially dissolved. Conversely, mechanical grinding and crystal selection in the

electron microscope may lead to an underestimation of the average crystal size since the grinding may break some crystals into smaller pieces (29). Overall, this technique is probably the most precise since different experiments have yielded reasonably consistent results that range from 200-1100 Å for the length, 100-200 Å for the width, and 15-60 Å for the thickness dimensions of bone mineral crystals (Table 2.2).

The second method used to prepare bone mineral is embedding in an acrylic resin, cutting thin sections, and viewing in a transmission electron microscope (36, 38, 47, 49). Thin sectioning has the advantage of preserving, to some degree, the spatial relationship of the crystals with respect to each other and to the collagenous matrix surrounding them, but this advantage is often negated by artifacts specific to this technique. Cutting thin sections on a water filled diamond knife results in the same problems mentioned above regarding processing in aqueous solutions. This can be eliminated by filling the knife with a non-aqueous solution such as ethylene-glycol. There are two additional difficulties associated with this technique: the cutting process usually leads to compression of the tissue in the cutting direction, and thin sections fix the plane of view of the tissue. The first limitation compresses crystals together and makes visualizing individual crystals difficult while the second limitation leads to off-axis views of crystals and thus underestimated values of crystal length and width and overestimated values of crystal thickness. Because of these artifacts, average crystal length measured with this technique is 170 Å (49), about half of that reported with other techniques.

A third and newer technique used to measure crystal size is x-ray diffraction line width broadening (29, 50-52). This technique relies on an assumption first made by

Guinier (53), that for small crystals, the crystal size corresponds with the coherence length (dislocation spacing). Using line broadening analysis, the width of the x-ray reflection line correlates with the coherence length. Thus, one can estimate crystal size by analyzing x-ray diffraction patterns, but since bone mineral has many imperfections the assumption underlying this method is questionable. Furthermore, in a comparative study, electron microscopy of liberated bone crystals provided more repeatable measurements of crystal size (29) indicating that the precision of this technique is relatively poor.

A fourth method used for measuring crystal size is similar to the first one described, except that instead of using dense bone tissue, mineral crystals are liberated from partially mineralized turkey leg tendon is used (42, 54-56). Turkey leg tendon is partially mineralized with crystals similar to those found in bone(49). The main advantage of this technique is that crystals can be viewed *in situ* so that the mineral-collagen spatial relationship is preserved (Figure 2.5). Disadvantages of this technique are that the crystals are not packed as densely as they are in bone and there may be subtle differences from bone mineral crystals. This technique has been used to study the structure of the mineralized collagen fibril as a composite structure in addition to the mineral itself.

Although all of the techniques used to measure crystal dimensions have some artifact associated with them, viewing liberated crystals in the TEM is most reliable. Despite wide variations in reported crystal lengths (200-1030 Å average length), crystal widths and thicknesses are relatively constant (average dimensions of 120-180 Å and 15-30Å, respectively). At the smallest level bone can be viewed as a composite material of short hydroxyapatite fibers embedded in a matrix of collagen. In this context crystal shape

and size are important parameters for modeling the mechanical properties of bone since the dimensions and the mechanical properties of the fiber determine the mechanical properties of short-fiber reinforced composite(33-35).

Polycrystalline Structure

The polycrystalline structure of bone mineral is not well characterized. Nearly all of the work on the structure of bone mineral published during the last twenty-five years assumes *a priori* that the mineral phase is discrete, *i.e.* crystals are not directly connected, but rather held in place by the surrounding matrix alone. Thus, the polycrystalline structure, like crystal shape and size, is an important parameter for theoretical models of the mechanical properties of bone. If the crystals are discrete, then a short-fiber reinforced composite model may be a useful tool in understanding bone mechanics. Alternatively, if the mineral crystals are contiguous (either completely or in part) a short fiber model may not be able to completely describe the mechanics of the material. Many different techniques to remove the organic component of bone *en bloc* have been investigated. Much of this work was motivated by a clinical need for non-load bearing bone substitutes, and thus biocompatibility was the primary concern, although a few authors did investigate the physical, chemical and mechanical properties of this "anorganic bone". Only the work related to the latter will be described here, since our interest is in the description of the mineral phase and not its biocompatibility. Although some of the techniques used to isolate bone mineral may slightly damage its structure, they do result in a contiguous mineral phase. The variety of techniques that can be used to arrive at isolated monolithic mineral component suggest that there is some contiguity of bone

mineral crystals *in situ* and therefore a short-fiber reinforced composite model, if considered, must address this characteristic.

Six different techniques have been used to remove the organic components of bone: extraction with potassium hydroxide (57-59); ethylene diamine (60-63), hydrazine degradation (64, 65), heat treatment at various temperatures (45, 66-69), sodium hypochlorite denaturation of proteins (40, 68, 70, 71), and hydrazine degradation coupled with plasma ashing (46). Most of these techniques are performed subsequent to mechanical grinding to substantially reduce the size of the bone particles and thus reduce the time required for the treatment. The end products of some of these treatments have been used for direct crystal size measurements in a transmission electron microscope as described above. Without mechanical grinding, though, some of these treatments lead to contiguous, solid blocks of bone mineral, possibly indicative of the *in situ* state (Figure 2.6)(57, 58, 60, 61, 63).

The first technique used to extract the organic components from bone was gentle boiling in potassium hydroxide for one to two hours (57-59). This technique does not yield as much of the mineral component as ethylene diamine extraction (58) which was the second technique used to deorganify bone. Additionally, potassium hydroxide damages the bone mineral (72). Thus, ethylene diamine extraction is preferred over potassium hydroxide.

Bone sections treated with ethylene diamine are contiguous and look similar to untreated bone (Figure 2.6). To extract the organic material from a 5 to 10 gram sample of trabecular bone, 100 ml of aqueous (80% ethylene diamine; (63, 73)) or anhydrous (60,

73) ethylene diamine is boiled in a soxhlet apparatus for 30-50 hours. A 5 gram sample of cortical bone can be extracted in 32-36 hours using 150 ml of ethylene diamine (61). Following the extraction, the mineral should be rinsed in distilled water to remove residual solvent. This method of extraction has been performed on both intact (60, 61, 63) and mechanically ground (60, 73) samples of cortical and trabecular bone.

X-ray diffraction and elemental analysis data suggest that anhydrous (95%) ethylene diamine extraction alone does not convert the amorphous mineral phase to a crystalline phase but subsequent rinsing in hot water does (60). Rinsing the resultant mineral in cold water (60) preserves the unit cell size (60), but not the amorphous phase (73). Thus, the preferred extraction method is anhydrous ethylene diamine followed by vacuum drying at 100°C (73). Comparing ashed bone with ethylene diamine extracted ashed bone indicates that a small (approximately 0.1%) but measurable decrease in the unit cell size of the mineral crystals occur with ethylene diamine extraction (60).

Although it was originally thought that ethylene diamine extraction removed all of the organic matter when calculated by weight loss (Figure 2.7), rejected grafts of extracted bone in dogs prompted a more thorough study. In three different species (human, mouse, dog) from 0.0109% to 0.173% nitrogen (per weight of extracted bone) remained after extraction and half of the nitrogen was present as amino acids (62). It was suggested that the residual amino acids were not extracted because they were bound to the mineral. This provides an alternative explanation to the large, contiguous mineral structures that result from ethylene diamine extraction. Specifically, if the extraction can not remove the organic component completely, the trace amounts of remaining amino acids may act to bind

discrete mineral crystals together and form a contiguous structure. In addition to physical and structural studies of extracted bone, two sets of mechanical tests have been performed on ethylene diamine extracted bone (74, 75). While these data indicate that the isolated mineral is much weaker and less stiff than intact bone (see Chapter 3), it is uncertain whether the mechanical properties measured were of a contiguous mineral structure, or a discrete array of crystals connected with trace amounts of non-extractable amino acids.

As an alternative to ethylene diamine extraction, hydrazine was employed as a method of digesting protein from bone to avoid the damaging affects of the former treatment. Anhydrous (95%) hydrazine, H_2NNH_2, successfully removed nearly 99% of the protein from rat cortical bone (65) and results in a contiguous product (64). This treatment has been performed at 40°C and 60°C, with the lower temperature doubling the time required to digest all of the protein from 3 gram sample of cortical bone (64). Compared to lyophilized controls, hydrazine treatment slightly reduces carbonate and acid phosphate content, but overall the Ca:P ratio and unit cell size remain constant (65). Similar results are seen for calcified arterial deposits (76).

High temperature ashing (600-700°C) has been used to measure the mineral content of bone for many years (25, 65, 72, 73, 77-79). High temperatures sinter the crystals and result in a material without the structural detail of the original tissue, although it is macroscopically similar (67). More recently, lower temperatures have also been used to deorganify bone. Bone samples treated to either 300°C or 500°C retain the osteonal structure, complete with Haversian canals and lacunae reminiscent of the original

material (67). Additionally, the macroscopic contiguity and relatively high load bearing capability of bone after heating to these lower temperatures will be shown later in this dissertation (Chapter 3).

TEM investigation reveals that the cross-banded pattern seen in mineralized collagen fibrils (Figure 2.5) persists in low temperature treated bone (Figure 2.8) which suggests that no sintering occurs at low temperatures (67). Furthermore, x-ray diffraction patterns show no change when bone is heated to 350° C 400° C or 600° C for two hours as compared to unheated bone (Figure 2.9) (45). Bone treated at 700° C or higher has substantially altered diffraction patterns, peaks become sharper and more distinct (Figure 2.9) indicating that sintering occurs between 600° C and 700° C (45).

Specimens heated at a variety of temperatures (300, 500, 700, 900 or 1200°C) were all described as "protein free" as assessed by calorimetric determination of hydroxyproline (67). Hydroxyproline is not common in non-collagenous proteins. Thus the absence of hydroxyproline does not necessarily imply a complete absence of protein, but rather an absence of collagen. More specifically, the absence of hydroxyproline does not necessarily imply that all of the collagen has been removed, but only that the hydroxyproline has either been damaged or removed; some other portions of the collagen chain may remain after heat-treatment. Furthermore, it will be shown later in this dissertation that as much as 15% of the organic material persists after heating at 350° C for 48 hours (Chapter 3). This suggests that some of the organic material is tightly coupled to the mineral phase and is not affected by heat treatment. Although it is more abundant, this may be the same material that remains after ethylene diamine extraction,

providing further indirect evidence that the mineral crystals are held together by small amounts of organic matter.

Differential thermal analysis of bovine dentin indicated that a large exothermic peak exists around 320°C for intact but not deorganified dentin (Figure 2.10). The absence of the peak at 320°C for deorganified bone indicates that this peak is attributed to the burn off of organic material (68). Studies on synthetic apatite indicate that in air, temperatures as high as 400°C have no effect on stoichiometry (80). Collectively, these data indicate that there is little change in the structure of bone mineral at any level: macroscopic, microscopic, crystal or atomic, with heat treatments at or below 400°C although the composition and role of the remaining organic material are still unknown.

Sodium hypochlorite (household bleach) is another chemical used to isolate the mineral component of bone. This is a relatively new technique and has been used successfully on finely ground particles of bone (40, 70, 71) and dentin (68). It has the disadvantages that it is not effective on larger samples and results in calcite (68), a mineral phase that is different from the hydroxyapatite found in bone.

The sixth technique used to remove the organic components from bone is a nonaqueous method that couples hydrazine treatment with subsequent low power plasma ashing (46). This method was developed to overcome the dissolution of the mineral that is thought to occur with aqueous methods. The first step in this procedure is milling the bone to 75-150μm powder and soaking in chloroform and methanol to remove the lipids. Second, the particles are treated with hydrazine (for three 12 hour periods) or subjected to a low power plasma ashing (5-10 W for 5-15 minutes) or both. Bone mineral crystals

from four different species have been successfully extracted with this method and all have resulted in discrete crystals. X-ray diffraction, infrared spectroscopy and TEM analysis indicate that bone mineral isolated with this method is not different from bone crystals isolated from the surface of bone tissue by sonication in ethanol only (Figure 2.11). This suggests that the former method does not alter the mineral and provides more evidence that: a) the bone crystals are discrete *in situ*; and b) other methods (ethylene diamine extraction and heat treatment) leave some trace of organic material which binds discrete crystals into a contiguous structure.

Of the six different techniques available to remove the organic components from bone, all but one leave some amount of contiguous mineral. In particular, ethylene diamine and low temperature heating have no adverse effects on the mineral crystal size or x-ray diffraction pattern. The contiguous nature of the material resulting from these techniques suggests some of the mineral phase of bone is contiguous *in situ*. An alternative and more likely explanation is that a small amount of organic material remains bound to the mineral after ethylene diamine or low-temperature heat treatment and acts as a glue to hold the mineral component together. This seems more plausible, since our data suggest that about 15% of the organic material remains after heat-treatment (see Chapter 3). Our attempts to extract this organic material from 350° C heat-treated bone with ethylene diamine and chloroform methanol however, have been unsuccessful. The discreet nature of the mineral phase is also supported by the individual crystals observed after hydrazine treatment and plasma ashing (46). Identification of the composition of the heat- and ethylene diamine-resistant organic material and its spatial relationship to the mineral crystals are other

important parameters for composite modeling of bone. Future work is needed to determine the composition, location and mechanical role of this material.

The Structure of Bone Collagen

Collagen is the most abundant protein in the body, accounting for nearly one third of all proteins by weight. The collagens are a family of at least 13 different proteins which all have a similar structure consisting of a superhelix of three different peptide chains. In most types of collagen the molecules are arranged in a highly ordered array to create a fibril. While a two-dimensional model of the molecular arrangement of collagen is widely accepted, the three-dimensional arrangement is not yet clear.

Molecular Structure

The collagen molecule is comprised of three distinct peptide chains. In bone collagen, which is type I, two of the peptide chains ($\alpha 1$) are from the same gene and one ($\alpha 2$) is from a second gene, thus type I collagen is labeled: $[\alpha 1]_2\alpha 2$. Each chain forms a left-handed helix with 3.6 residues per turn. The three chains are then intertwined to form a right-handed super helix (81, 82) (Figure 2.12). Each left-handed helix is made of 338 triplet repeats with nearly every third residue being glycine (83) . Glycine occupies the central positions in the super helix, where steric hindrance would prevent other larger residues (Figure 2.12). The imino acids, proline and hydroxyproline, follow glycine in the primary structure (*i.e.* Gly-Pro-Hyp) throughout approximately one third of the collagen molecule. The ring structures found in the imino acids favor the triple helical conformation. On each end of the 338 triplet repeat chain, short (10-30 residue)

telopeptides help stabilize the intermolecular structure (Figure 2.13). The super helix is a rod shaped molecule 294 nm long (84) and 15 Å in diameter (85).

Collagen Fibril Structure

Extracellular collagen molecules are arranged into fibrils. A model of the fibril structure was proposed in 1963 by Hodge and Petruska (86) and is now widely accepted. In this model, individual collagen molecules are stacked head (carboxyl terminus) to tail (amino terminus) with a short gap between them. Side-to-side, molecules are arranged in a quarter-staggered array (87) (Figure 2.14). The quarter-staggered array results in alternating dark and light sections when negatively stained and viewed with an electron microscope. The dark bands are at cross-sections where there is a hole or gap every fifth molecule (called the h-zone or g-zone); the light bands correspond to overlap regions where no hole zones exist (o-zone). The repeat period of the collagen fibril is called the D period and consists of one dark and one light band. The length of the D period is 66.8 nm, the gap between molecules is 0.52 D periods (35 nm).

Much less is known about the three-dimensional arrangement of collagen molecules within the fibrils. In bone, fibrils range from 20 to 40 nm in diameter, suggesting 200 to 800 molecules in the cross-section of a fibril. No data on fibril lengths has been reported. Most models of the three-dimensional collagen arrangement include a discussion of the location of the mineral crystals, since the total mineral volume is substantial (43% of wet bone) (88) and affects how the collagen is packed. The next section contains a more detailed discussion of structure of the collagen fibril, in the context of the mineralized fibril, which is the building block of bone.

Composite Structure of Bone

Mineralized Collagen Fibril Structure

As discussed above, the three-dimensional structure of the collagen fibril remains elusive. Models of the three-dimensional structure of bone collagen fibrils must account for the inclusion of the mineral phase within the fibrils. This fact has been used to exclude some early models. Many different models for the three-dimensional packing of collagen molecules have been proposed; most are slight variations on others. Three representative structural models are discussed here. In the first and simplest model, there is no order to the planes of quarter-staggered molecules. Consequently, there is not necessarily any alignment between hole zones. In this model the hole zones may be as small in cross-section as a single collagen molecule, about 1.5 nm in diameter which is too small to accommodate the mineral crystals and therefore not a likely configuration for bone collagen.

In the second model, quarter-staggered planes of molecules are also offset in a quarter staggered array . This results in hole zones which are in line but not contiguous (Figure 2.15f). Again, these hole zones would be about 1.5 nm in diameter, too small for mineral crystals, suggesting this is not a possible arrangement for bone collagen. Additionally, this model assumes hexagonal packing. Although the lateral packing of collagen molecules in rat tail tendon is hexagonal (89), it may not be in other tissue types since x-ray diffraction patterns are different (90, 91), and because hexagonal packing would be too tight to accommodate the mineral phase of bone (92).

The third model proposes that the quarter-staggered planes are stacked side-by-side with no offset (93) (Figure 2.15e). This results in hole zones which are in line and contiguous. Although this model also assumes hexagonal lateral packing, the alignment of the hole zones provides for large channels where the mineral crystals can reside. This model is the most accepted, because it is the only model with hole zones large enough for the mineral crystals (42). Studies on cross-link locations (94) also suggest that this model is the most accurate. Analysis of the cross-link pattern also shows that all the collagen molecules are azimuthally aligned (94). Of course, many other stacking arrangements (most non-hexagonal) could be proposed. It has also been suggested that the lateral packing may change during mineralization (92, 95). This would indicate that one spatial model can only be correct before or after mineralization, but not both.

Lamellar Structure

The lamellar structure of bone was first recognized by Havers, over three hundred years ago (5). Specifically, Havers observed structures composed of concentric cylinders, each cylinder had a central canal for blood and nervous supply and from five to twenty layers, or lamellae, surrounding each canal (5). These cylindrical structures are called osteons and will be described in more detail in the next section. Lamellae are present in osteons, in the periphery of long bone diaphyses (as circumferential lamellae), and between osteons (as interstitial bone) (Figure 2.16). The exact structure of the lamellae that Havers observed is still unclear. The collagen fibers within each lamella are usually considered to have a single principal orientation, but even this is controversial (96). Many different models of lamellar structure have been proposed but only three are unique; these three will be discussed here (Figure 2.17).

The first model, proposed by Gebhardt (97-99), claims that there are no structural differences in different lamellae, only differences in principal orientation as determined by the orientation of the collagen fibrils (97-101). The second model proposes that there is a structural difference in different lamellae in addition to changes in the collagen orientation between lamellae, the packing density of the collagen fibrils is low in one lamellae and high in the next (102-105). The third and most recent model suggests that there is no principal orientation to the collagen fibers within each lamella, but that only the amount of mineralization and collagen packing density distinguish different lamellae (96, 106-108). While Gebhardt's model is commonly found in histology textbooks, there are recent studies supporting each model (54, 96, 106, 108, 109).

Gebhardt's observations of thinly ground transverse sections of undecalcified bone through polarized light suggested that lamellae in osteons have alternating orientations, with the collagen fibers arranged along the length of the osteon in one lamella and circumferentially around the osteon in the next (97, 98). Thus the orientation of neighboring lamellae differ by approximately 90°. Different lamellae are distinguished by assuming that lamellae with longitudinally oriented collagen fibers will appear dark when observed between crossed polarizing filters while lamellae with transversely (or circumferentially) oriented collagen fibers will appear bright (Figure 2.18). This effect is due to the fact that polarized light is extinguished in materials that are isotropic in the plane of the section but it is transmitted in materials that are anisotropic (oriented) in the plane of the section. An important limitation of polarized light microscopy is the assumption that dark lamellae have only longitudinally oriented fibers and bright lamellae have only transverse or in-the-plane fibers. As noted by Marotti (96), the lamellae which appear bright may contain other fibers which are not in the plane of the section and are therefore extinguished. Conversely, the lamellae which appear dark may not be longitudinally oriented but rather afibrillar, that is, lacking fibers altogether, or made up of randomly arranged fibers (96). These types of lamellae would also appear dark since they are

isotropic in the plane of the section (and in all planes). This limitation has lead to the use of the scanning electron microscope as a tool to study the lamellar structure of bone (100, 101, 107, 110).

A recent variation on the Gebhardt's model is the twisted or rotated plywood model (100, 101). This model is similar to Gebhardt's model in that different lamellae are considered to have different orientations. It differs from Gebhardt's model however, in that the collagen orientation is not constant throughout an entire lamella but rather it can vary through the thickness (110). A series of nested arcs was observed in some thin sections of undecalcified bone (101) and these arcs were interpreted as a twisted plywood architecture, in which the angle between neighboring layers of collagen fibers is much less than 90°. These layers were observed within a single lamellae, suggesting that there is a continuous shift in the orientation of the collagen fibers through each lamellae which appears as series of nested arcs when viewed in an oblique section (Figure 2.19). Further observations suggested that there are five planes or arrays of fibers within each lamellae, each differing by 30° such that the fourth array is perpendicular to the first and the collagen orientation varies from 0° to 120° in each lamella of this type (Figure 2.21). In addition to the nested arc structure, other sections showed a herringbone pattern, indicative of the traditional Gebhardt model with a 90° angle between successive lamellae. These observations of bone in a scanning electron microscope thus confirmed a refined version of the Gebhardt model of lamellar structure.

A second model of lamellar structure supposes that the main difference between lamellae is in the collagen packing density and the amount of "ground substance" which fills the void space. In this model the lamellae alternate between a narrow, compact, collagen-dense structure (called fibrous, striped or compact lamellae) and a broad, diffuse mineral rich structure (called homogeneous, intermediate or diffuse lamellae). Variations of this model have been proposed by several authors (102-105) but it was most fully developed by Ruth (102). In addition to the differences in fibril packing density, the fibril

orientation was alternated between radial and circumferential; no longitudinal fibrils were observed (102). These studies were based solely on images obtained through transmitted and polarized light microscopy, although 5-10 μm thick sections did reveal differences in radioopacity in alternating lamellae suggesting that some differences in mineral density do exist (111). Recent studies, in particular, those which utilize the scanning electron microscope, have not reported any radially aligned fibrils, but have confirmed the loose-dense-loose arrangement of successive lamellae (107, 108).

The third, and most recent, model of the lamellar structure of bone incorporates the loose-dense-loose packing of successive lamellae but contends that there in no principal orientation in any lamellae (96, 106-108). Viewing bone in a scanning electron microscope at 11,000 X magnification, Marotti demonstrated that there are mostly randomly arranged fibrils in both the thick (previously called diffuse or transverse) and thin (previously called compact or longitudinal) lamellae although some small packets of oriented fibrils were observed (106-108) as previously reported(110). If this model is correct, it would suggest that bone is an isotropic material, at least with respect to the organic component.

Although there is a great discrepancy between these models, some of the differences can be explained by looking closely at the interpretation of images observed with polarized light microscopy. The argument follows that first made by Marotti (96, 107, 108). Specifically, the images that originally lead to both Gebhardt's and Ruth's original models were at the light microscopic level, from 200-1,000 X magnification and employed polarized light microscopy. These authors, and many others, assumed *a priori*, that lamellae which appear bright, or birefringent, must contain only fibers which lie in the plane of the section, *i.e.* transverse fibers in a transverse section or longitudinal fibers in a longitudinal section. This may not have been the case (Figure 2.18). Other fibers, not in the plane of the section may have been present, but were not seen since they were isotropic and thus extinguished. Thus lamellae which were considered transverse because they were birefringent in a transverse section may also have contained longitudinal or oblique fibers

which were extinguished under polarized light. Additionally, since fibrils viewed in cross-section are round and thus isotropic in the plane, extinguished lamellae were assumed to be comprised only of fibers perpendicular to the section. An alternative explanation of this finding is that these lamellae may have lacked fibers or had a random arrangement of fibers of which would lead to an isotropic and thus extinguished appearance under polarized light. While this is a strong argument that polarized light microscopy may not be an accurate method for determination of collagen fibril orientation, the bulk of the data obtained from electron microscopy still supports the rotated plywood (revised Gebhardt) model (100, 101).

The parallel sheets of lamellae is another composite level of bone. In this level, each group of lamellae is considered a stacked laminate, where each laminae is embedded with mineralized collagen fibrils aligned in one direction. Modeling the mechanical properties of bone with this type of composite structure is usually done in the context of osteonal bone, which will be described in the next section.

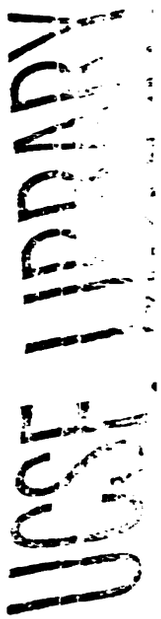

Osteonal Structure

Two types of osteons, or Haversian systems, have been described according to when they were created. Primary osteons, as their name implies, are the first osteons created. They replace woven bone, which is the first bone created in mammals and has randomly oriented collagen fibrils. Primary osteons are, in turn, replaced by secondary osteons. Primary osteons are replaced as early as the sixth month of fetal development (112); osteons found in human adults are secondary osteons and thus most studies have focused on these. All osteons are comprised of a central (Haversian) canal which houses blood supply and nerves and from five to 20 concentric lamellae surrounding the canal. Primary and secondary osteons are distinguished by the cement sheath which surrounds secondary osteons as a result of the change in cellular activity from resorbing to creating bone. The cement sheath, or cement line as it is often called, is a layer of calcified

mucopolysaccharides with very little collagen (113, 114) and a lower mineral fraction than the osteons they surround (115, 116).

The highest of the hierarchical composite levels of bone is that in which the osteons act as continuous fiber reinforcements in a matrix of interstitial bone. The interstitial bone is comprised of lamellar bone and the remains of osteons that have been replaced by newer ones. Thus it tends to be older and more highly mineralized compared to osteons themselves. Modeling the mechanical properties of bone with this type of composite structure requires knowledge of the dimensions of osteons and possibly the lamellae that comprise them. Osteons are typically 150-300 μm in diameter (64); Haversian canals are 75-150 μm diameter (64); each lamella is 5-10 μm thick (64); and there are approximately 10-20 lamellae per osteon. The exact length of osteons is difficult to measure since they bifurcate and connect along the length of the bone, but an average length of 10 mm has been suggested (117).

Most authors have described osteons according to the principal orientation of the constituent lamellae even though the structure of the lamellae themselves is still somewhat controversial as discussed previously. Generally, either the original or revised Gebhard (rotated plywood) model is assumed to be correct, and then osteons can be characterized according to their appearance between crossed-polarizers (Figure 2.23). Osteons viewed in longitudinal cross-section between crossed-polarizers are classified as light, dark or intermediate. Light osteons contain mostly circumferentially oriented lamellae; dark osteons mostly longitudinally oriented lamellae; and intermediate osteons some of each (118-120). Different types of osteons withstand mechanical loads differently; light osteons are stronger

in compression and dark osteons are stronger in tension (118, 121). This suggests that there is some level of fiber alignment within lamellae, as described by the original or revised Gebhardt model, since randomly arranged fibers would all be stronger in compression like larger samples of bone.

Summary

Overall, there are four identifiable hierarchical levels of the composite structure of bone: mineral crystals acting as short-fiber reinforcements in a matrix of collagen; mineralized collagen fibrils acting as continuous-fiber reinforcements in a matrix of mineral and non-collagenous proteins; groups of lamellae acting as a stacked laminate reinforced with mineralized collagen fibrils; and osteons acting as continuous-fiber reinforcements embedded in a matrix of interstitial bone. Different models have been proposed to describe the anatomy at each level of composite structure. These structural models, together with observations and data from x-ray diffraction, spectroscopy, light and electron microscopy, then provide input parameters and guidelines for developing theoretical models that aim to explain the mechanical properties of bone tissue. Mechanical models may include one or more of the composite levels of bone tissue. Models which include only one composite level are easily interpreted but may lack accuracy. Conversely, more complex models may be more accurate but will be more difficult to interpret. Theoretical models of different hierarchical levels will be proposed and discussed in more detail in future chapters.

Table 2.1. Composition of cortical bone. Entries in italics are percentage of organic matter. Data from (122) and (123).

	Weight %		Volume %	
	dry	wet	dry	wet
Mineral	77	69	57	43
Organic matter	23	21	43	32
Collagen (Type I)	*90-94*	*90-94*	*NA*	*NA*
Glycosaminoglycans	*1*	*1*	*NA*	*NA*
Other proteins	*5-9*	*5-9*	*NA*	*NA*
Lipids	*0.5*	*0.5*	*NA*	*NA*
Water	NA	10	NA	25

Table 2.2. Bone mineral size as measured by various authors using different techniques.

References	Species	Tissue	Crystal Habit	Length† (Å)	Width† (Å)	Thickness† (Å)	Preparation Method	Measurement Method
Wolpers (1949)			rod	(400-1000)		(30-60)		TEM
Fernández-Morán & Engström (1957)			rod	200		(30-60)		TEM, XRD
Speckman & Norris (1957)	Human/ Canine		rod	(600-700)		50		TEM
Engström (1966)	Turkey	tendon		350	(40-50)	NA	grinding	XRD
Höhling (1974)	Rat	tail bone	rod			(15-20)	embed, section	TEM
Weiner & Price (1986)	Human	femur	plate	535 (225-1100)	285 (150-600)	NA	grinding, NaOCl	TEM
Weiner & Traub (1986)	Turkey	tendon	plate	334±106	185±63		shredding	TEM
Arsenault & Grynpas (1988)	Rat	tibia	plate	168±4	56±1	NA	NaOH	XRD
Weiner & Traub (1989)	Rat	tibia	plate	(180-366)	(104-187)	(20-25)	grinding, NaOCl	TEM
Holden, Clement & Phakey (1995)	Human	femur	rod	252±23	64±11	NA	none	XRD line broad.
Holden, Clement & Phakey (1995)	Human	femur	rod	267±9	83±16	NA	400°C heat	XRD line broad.
Kim, Rey & Glimcher (1995)	Bovine	tibia & femur	plate	273±72	158±72	(15-20)	nonaqueous	TEM
Kim, Rey & Glimcher (1995)	Mouse	tibia & femur	plate	212±72	120±43	(15-20)	nonaqueous	TEM
Kim, Rey & Glimcher (1995)	Chicken	tibia & femur	plate	233±84	122±48	(15-20)	nonaqueous	TEM
Kim, Rey & Glimcher (1995)	Herring	bones	plate	373±190	154±100	(15-20)	nonaqueous	TEM
Kim, Rey & Glimcher (1996)	Chicken	cartilage	plate	1030±260 (700-1600)	680±160 (400-1000)	NA	nonaqueous	TEM

† Dimensions given in mean ± SD (range) as reported.

Blank cells indicate that the data were not reported.

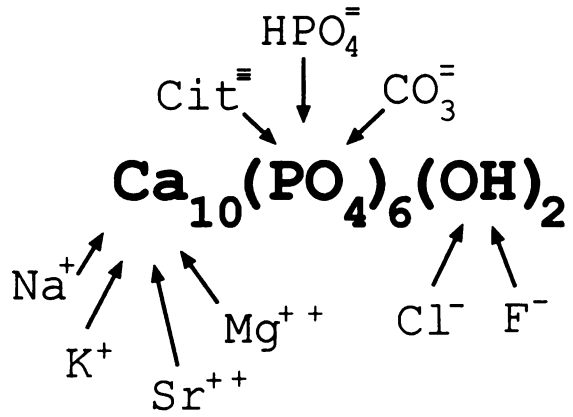

Figure 2.1. Stoichiometry of hydroxyapatite and the substitutions found in bone. Substitutions affect chemical properties of the mineral, especially solubility, which may have important biological implications. An alternative stoichiometry which accounts for the most common substitutions has been proposed: $Ca_{8.3}(PO_4)_{4.3}(CO_3)_X(HPO_4)_Y(OH)_{0.3}$ where Y decreases and X increases with age but always sum to 1.7 (22).

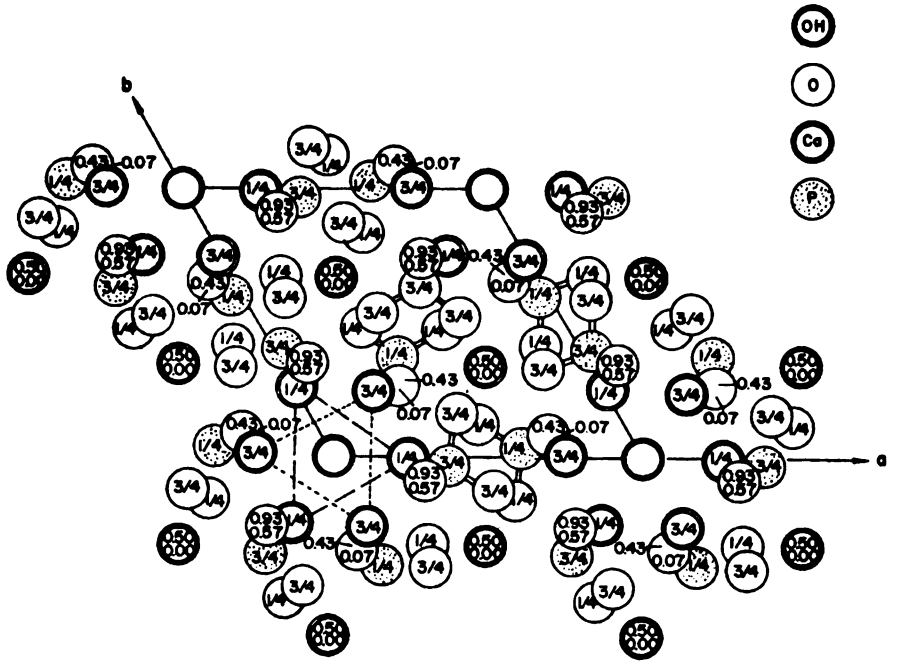

Figure 2.2. Hydroxyapatite structure projected down the c-axis on the basal plane. From (124), figure 9-7; data originally from (24).

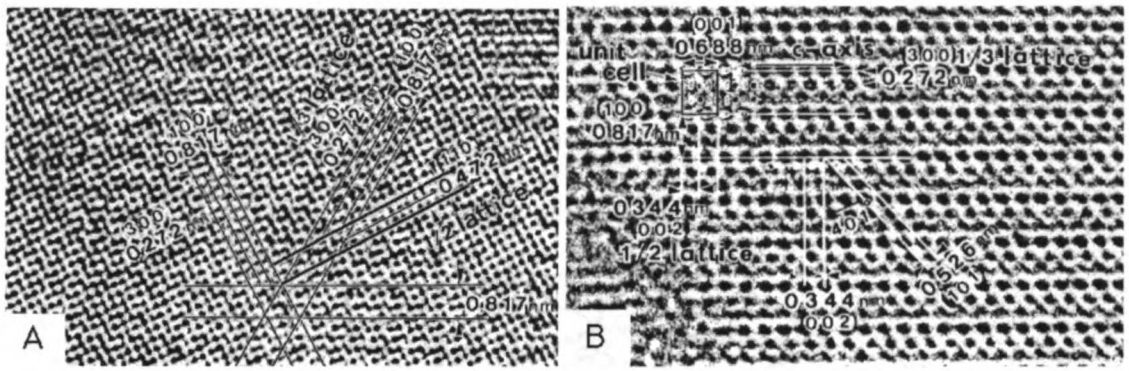

Figure 2.3. Transmission electron microscope cross-sectional images of a bone mineral crystal. A: The a-b plane with lattice dimensions (8.17 Å in a and b directions) and a unit cell indicated. B: A longitudinal section showing the a-c (or b-c) plane with lattice dimensions (8.17 Å X 6.88 Å) and a unit cell indicated. From (31), Figures 16 and 17.

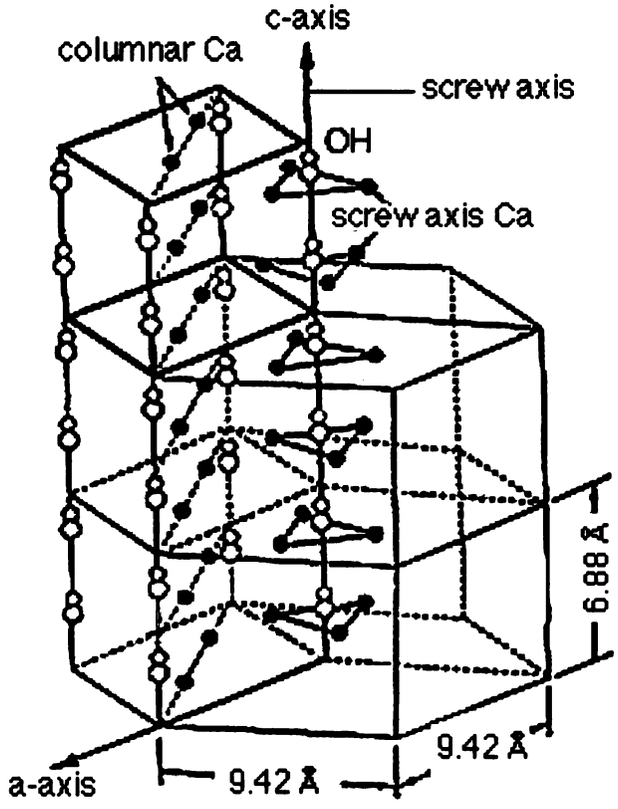

Figure 2.4. Definition of unit cell of bone mineral. Parallelepiped unit cell is in bold, dimensions shown for hexagonal unit cell only. From (31), Figure 4.

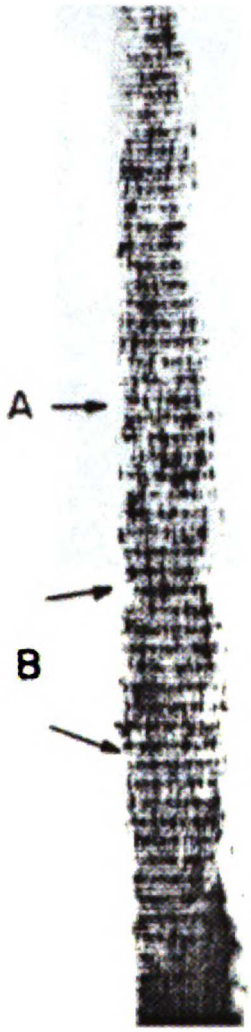

Figure 2.5. Unstained collagen fibril extracted from turkey leg tendon, more mineralized areas appear darker in the image. The fibril is unmineralized at the top and substantially mineralized at the bottom. Near A, crystals are generally confined to gap regions, whereas near B the crystals look longer and extend into the overlap regions. From (42), Figure 3.

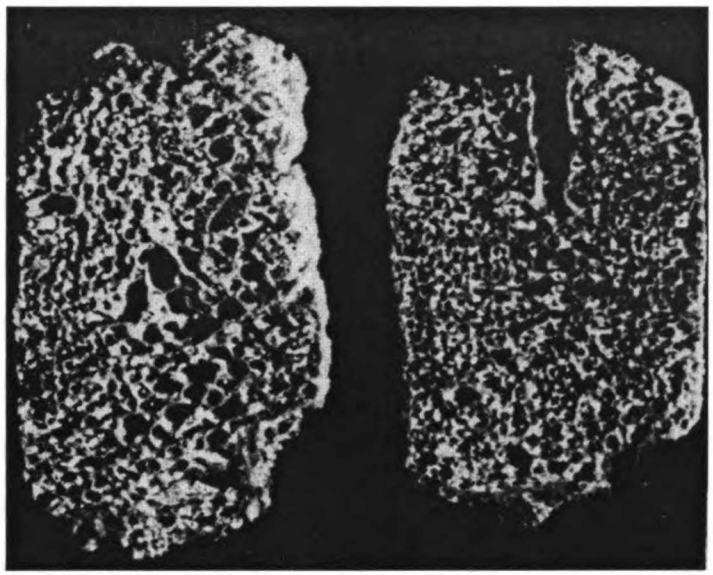

Figure 2.6. Cross-sections of two of a child's vertebrae after extraction in ethylene diamine. Note the contiguous nature of the bone tissue. Kjeldahl analysis indicated that less than 0.1%, by weight, nitrogen remained, indicating that all of the organic material had been removed. From (63), Figure 1.

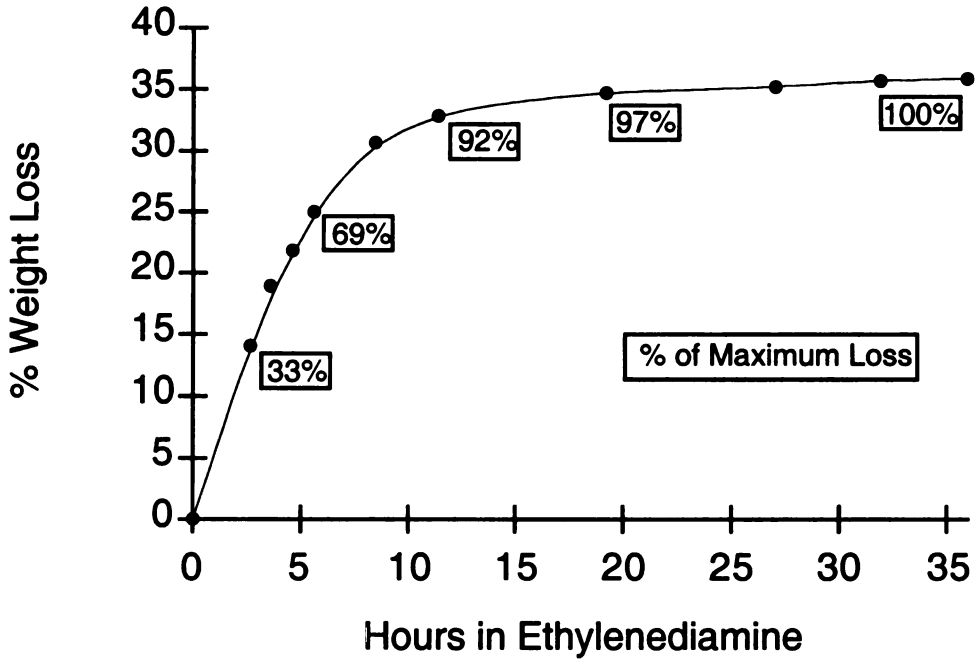

Figure 2.7. Weight loss in human bone during ethylene diamine extraction. Percent of maximum loss was calculated assuming that bone is 65% mineral by weight. Adapted from (61), Figure 1.

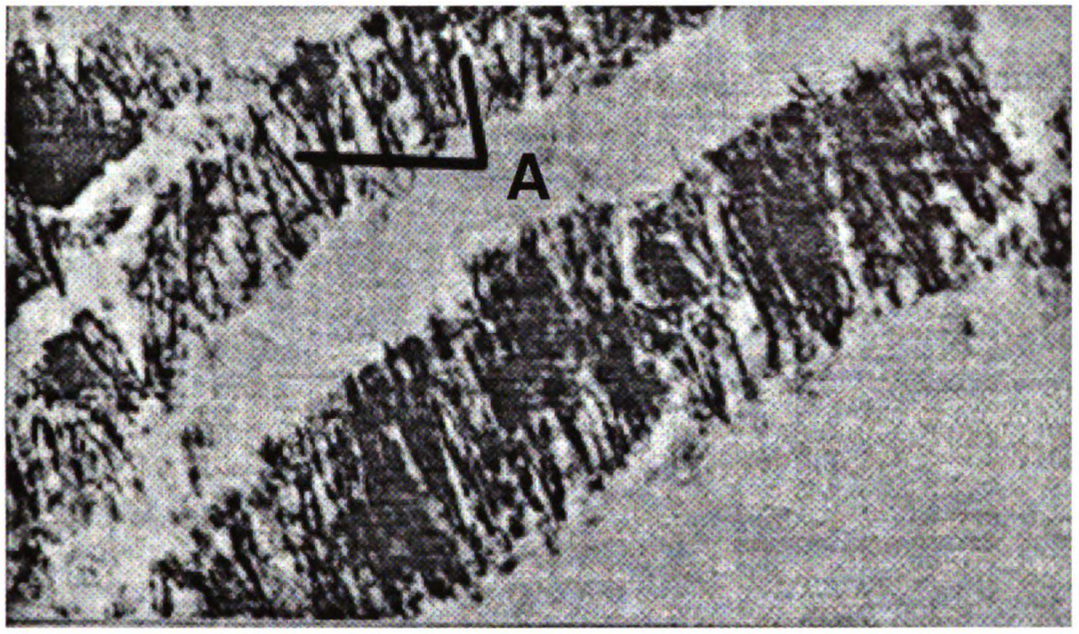

Figure 2.8. TEM micrographs of bone heated overnight at 500°C, mineral appears dark in the images. The cross-banding of collagen fibrils is revealed by the electron density of the mineral phase (top, 20,000 X). The mineral phase can be resolved into needle shaped crystals aligned with the fibril axis (A). From (67), Figure 7.

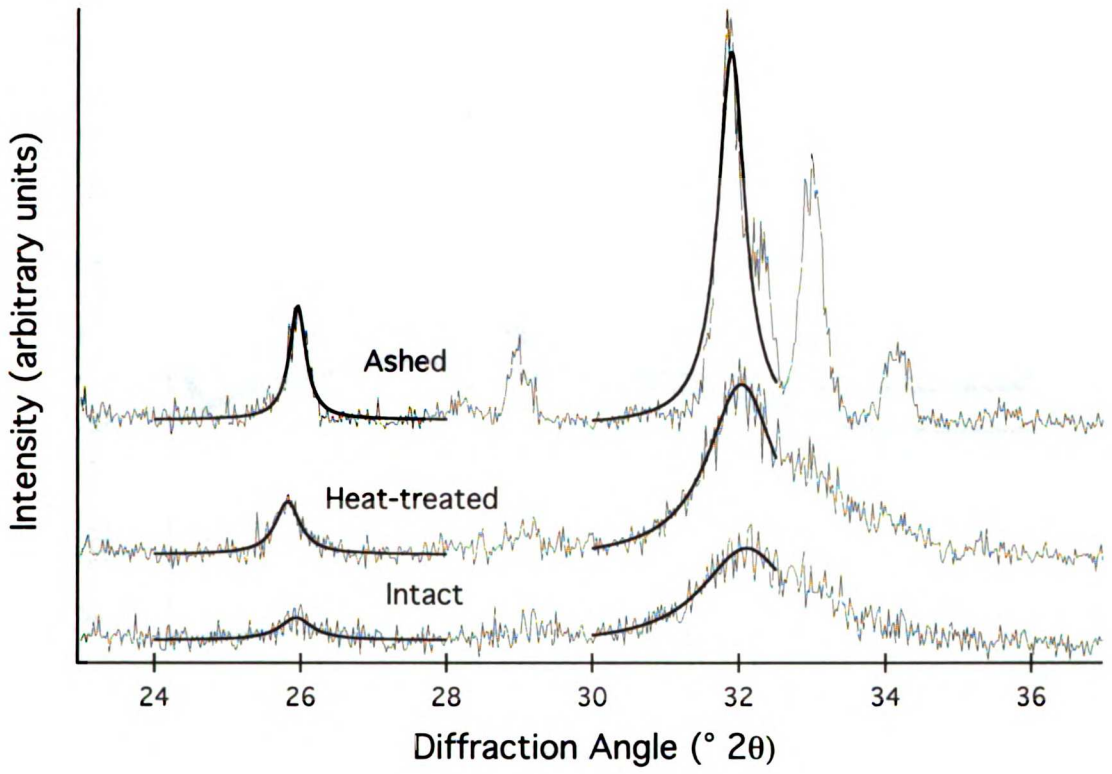

Figure 2.9. X-ray diffraction patterns of intact, heat-treated (350° C) and ashed (700° C) human bone. Heating at 700° C or above substantially affect the diffraction pattern, peaks become more distinct and sharper, temperatures below 400° C do not induce this effect (see Chapter 3).

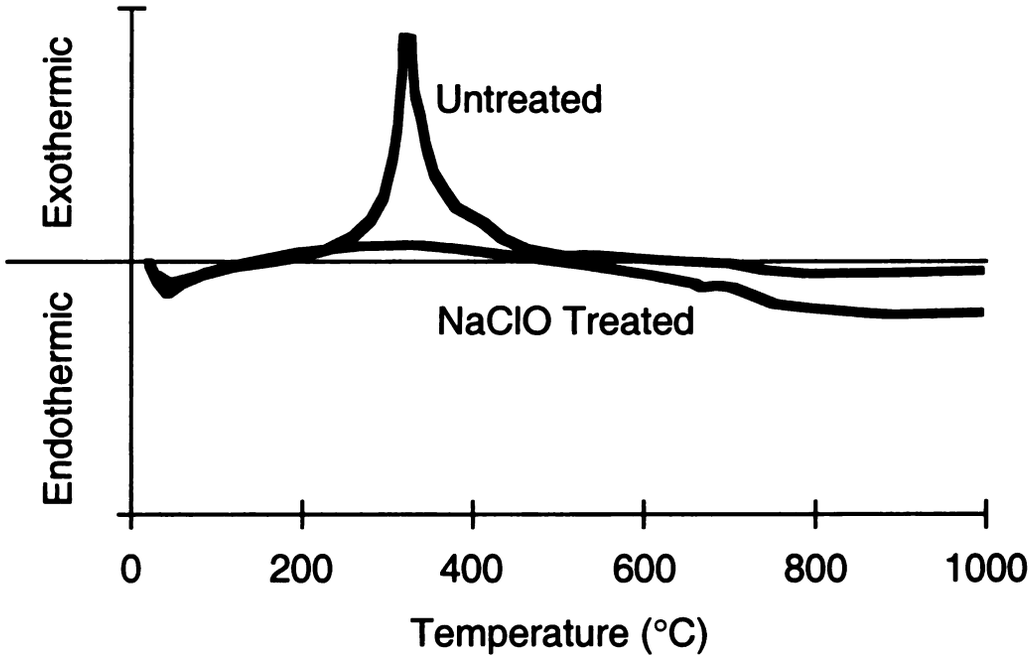

Figure 2.10. Differential thermal analysis curves for untreated and sodium hypochlorite (NaClO) treated samples of human dentin. The existence of a large peak near 350° C in untreated dentin but not in the NaClO treated bone indicates that the organic material is removed at 350° C. Modified from (68), Figure 1.

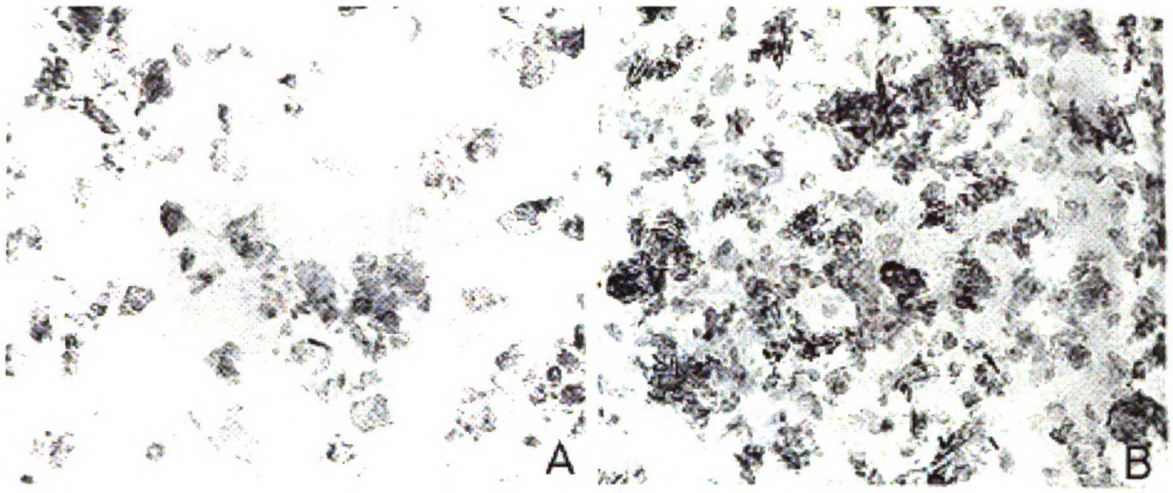

Figure 2.11. Electron micrographs of crystals of bovine bone isolated by sonication in ethanol (A) or by nonaqueous washing and low power plasma ashing (B). The crystals liberated with both methods are similar indicating that low power plasma ashing did not damage the mineral crystals. From (46), Figure 3.

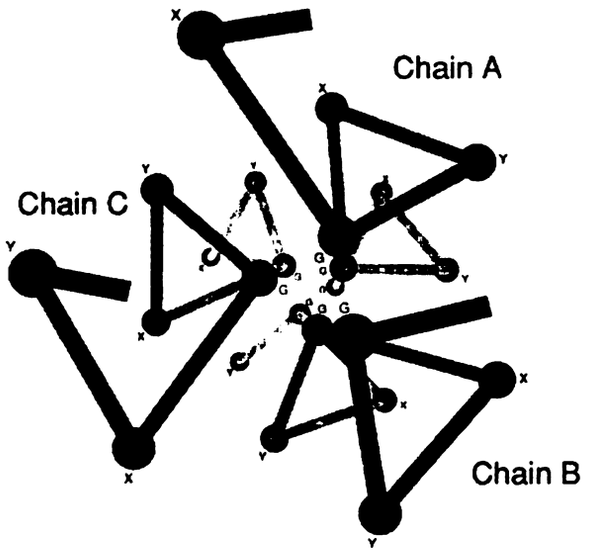

Figure 2.12. Diagrammatic representation of a cross-section through a collagen molecule showing three separate chains, labeled A, B & C. Glycine (G) usually occupies every third position, proline (Y) and hydroxyproline (X) follow glycine in about one third of the collagen molecule. Since there are 3.6 residues per turn of each peptide chain, the small glycine residues reside along the central axis of the triple helix. From (125), Chapter 6, Figure 1.

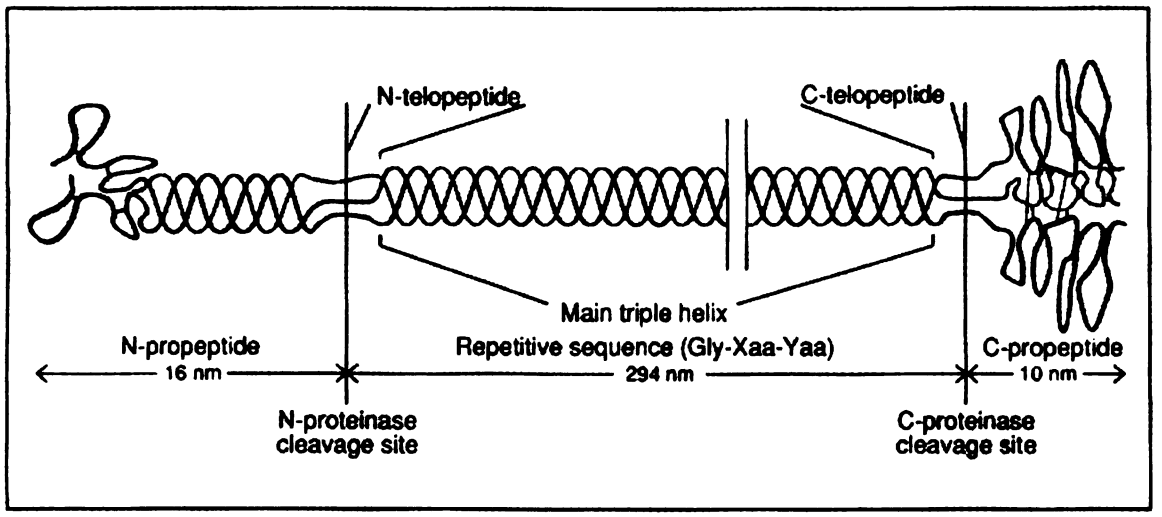

Figure 2.13. Diagrammatic representation of a collagen molecule, complete with N- and C-propeptides and the central super helix, with 337 triple repeats. Part of each propeptide is cleaved after the molecule leaves the cell. From (125) Chapter 6, Figure 2.

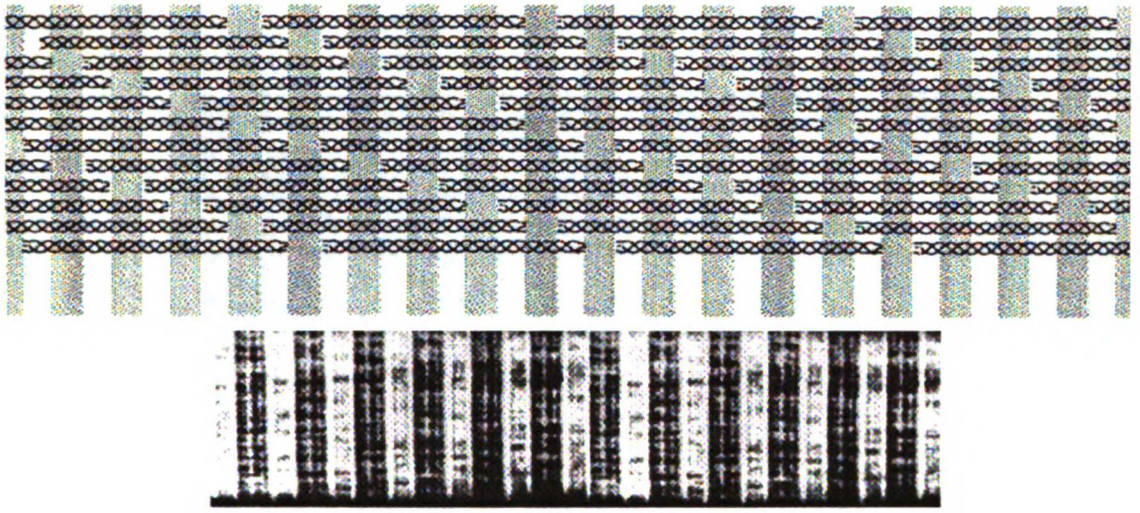

Figure 2.14. Diagrammatic representation of an array collagen molecules arranged in a quarter-stagger arrangement (top); negatively stained electron micrograph of collagen fibril (bottom). The scales along the molecules are the same, (one molecule is 294 nm long) but the thickness is magnified in the top view (one molecule is 1.5 nm thick). One D-period consists of one dark and one light band (66.8 nm). From (125) Chapter 6, Figure 3.

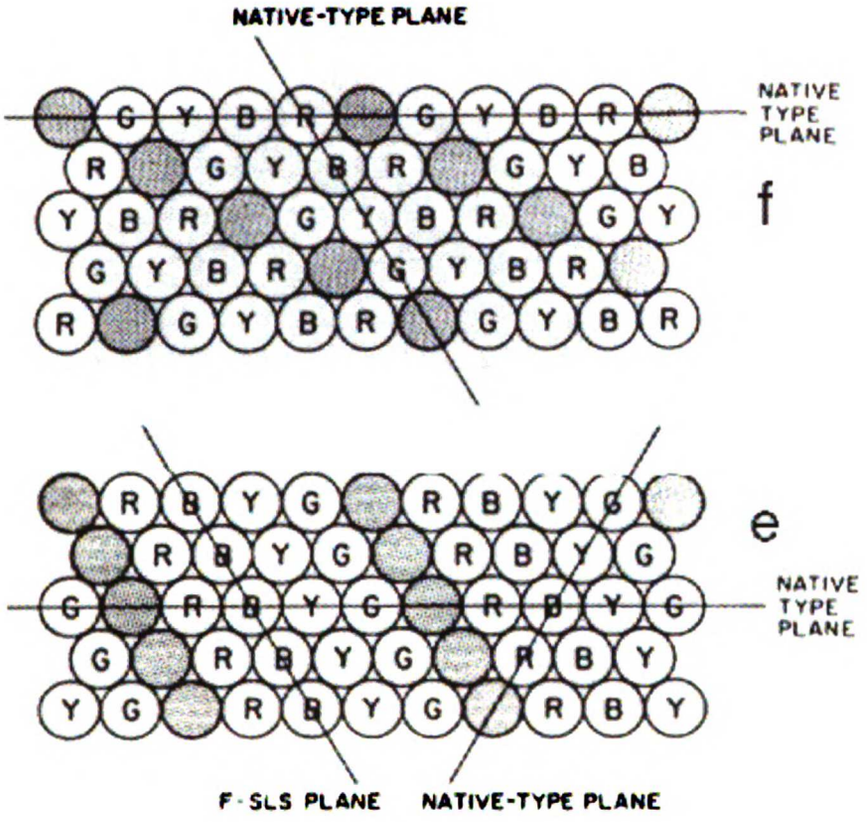

Figure 2.15. Top: schematic cross-section of one model of the three-dimensional stacking of collagen molecules. This arrangement was made by creating a quarter staggered pattern in both hexagonal directions. The hole zones are not adjoining; this is unfavorable for accommodating wide mineral crystals. Bottom: schematic cross-section of an different model. This arrangement was made by stacking the quarter-staggered planes with no lateral offset. The hole zones are contiguous, a favorable scenario for mineral deposition and growth. The letters indicate color bands on the plastic model that was built to visualize the model; each color represents a fixed location along the length of the collagen molecules. Modified from (126), Figures 7 and 8.

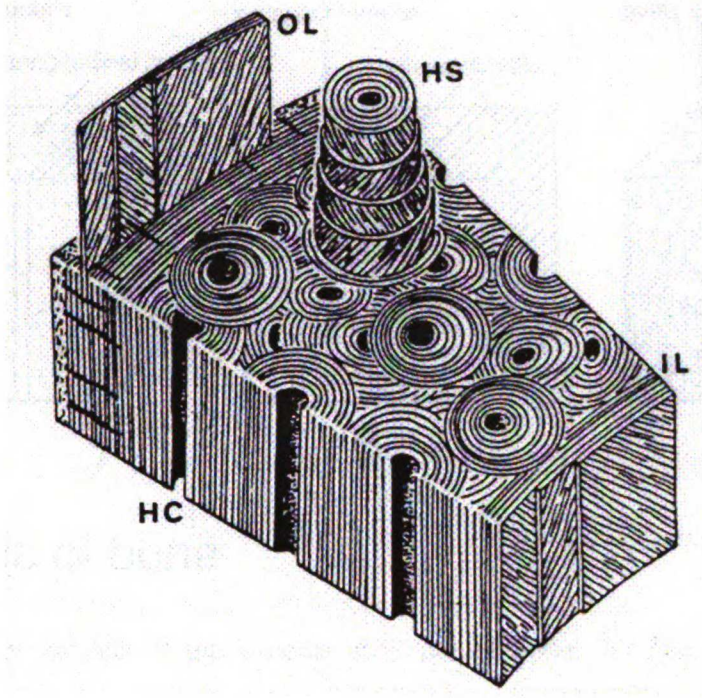

Figure 2.16. Diagram of a sector of the shaft of a long bone. The osteons (Haversian system: HS) are located between the outer and inner circumferential lamellae (OL, IL, respectively). The lamellae that form osteons are arranged concentrically around a central Haversian canal (HC). Cement lines separate the osteons from interstitial bone, which is comprised of the remnants of partially resorbed osteons. From (101).

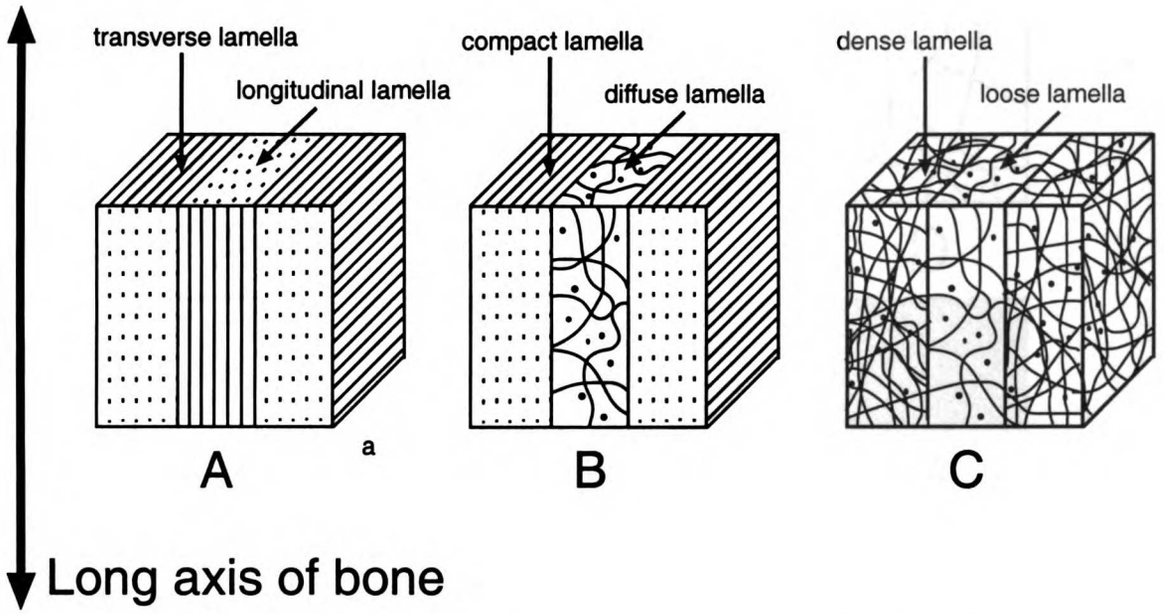

Figure 2.17. Three models of the lamellar structure of bone. A) The original and most accepted model proposed that the collage fibers in each lamellae were aligned and that the orientation alternated between longitudinal and transverse (99). B) A second unique model proposed that the osteonal lamellae were either diffuse and radially aligned or dense and circumferentially aligned, the main difference being the collagen packing density (102). C) The most recent model denies any principal orientation in lamellae and proposes instead that all fibers are randomly arranged and collagen packing density is the only difference in alternating lamellae (108). Based on figure from (108).

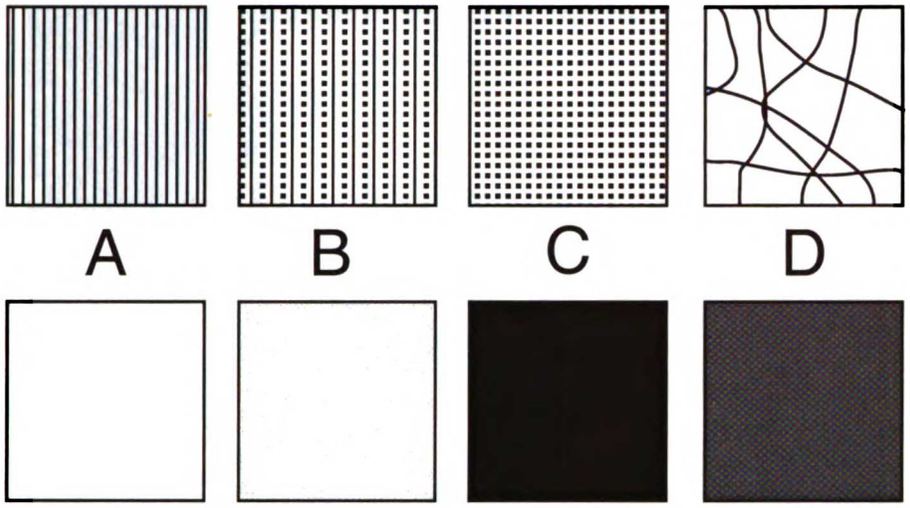

Figure 2.18. Schematic diagram to illustrate different structures (top) and their theoretical appearance between crossed polaroids (bottom). In each section, lines and curves represent fibrils in the plane of the section, dots indicate fibrils lying perpendicular or at oblique angles to the plane of the page. The structure in A appears bright since it is anisotropic (highly oriented) in the plane of the section. The structure in B also appears bright, since it too is anisotropic. It does contain some fibrils not in the plane, however. The structure in C appears dark since it is isotropic in the plane of the section. The structure in D also appears dark even though it does not contain any fibrils normal to the plane of the section.

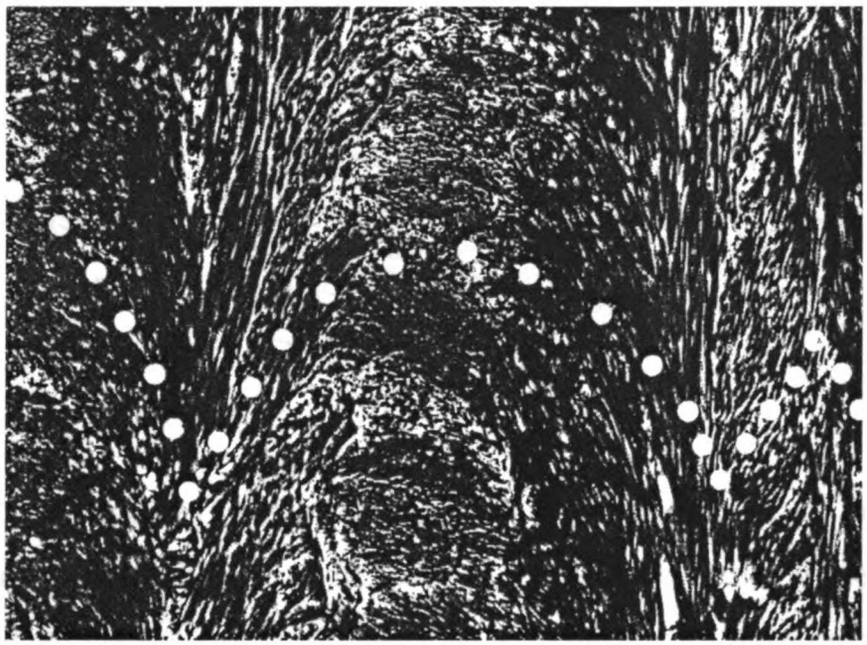

Figure 2.19. An oblique section through decalcified human cortical bone, 7,650 X. Small changes in angles between arrays of collagen fibrils results in a nested arc structure, indicated by the dotted line. From (101).

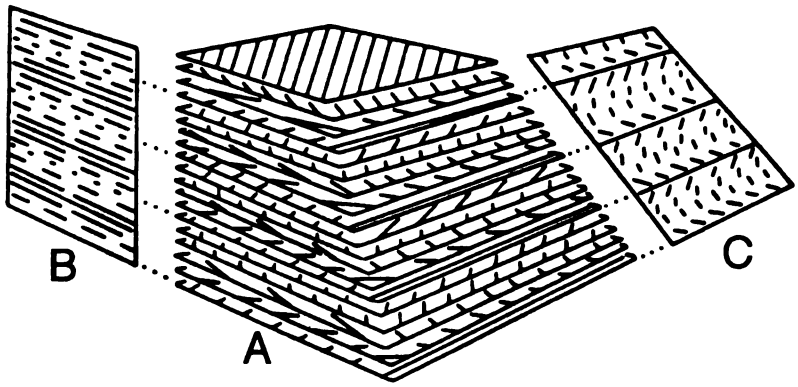

Figure 2.20. Schematic of twisted plywood structure of lamellae. A. On each parallel plane, lines indicate the direction of the fibrils. B. A transverse section where the fibrils appear as short or long segments, depending on the angle that the plane makes with the fibrils in each layer. C. An oblique plane results in a series of nested arcs. From (101).

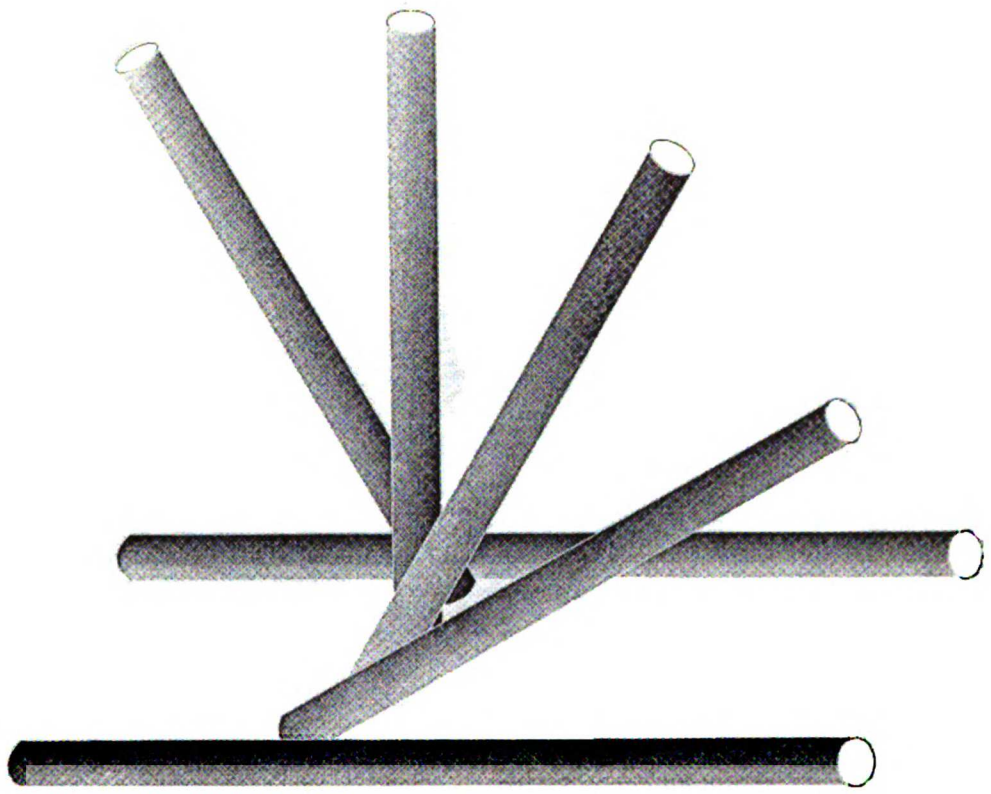

Figure 2.21. Schematic model of the collagen orientations in five arrays of parallel fibrils that together comprise one lamellar unit. Each cylinder represents a single array. The horizontal array in the foreground is repeated in the background. The latter represents the first array in the adjacent lamella. The angle between each array is 30°, and so the fourth array is orthogonal to the first and the arrays in each lamella span 120°. From (100).

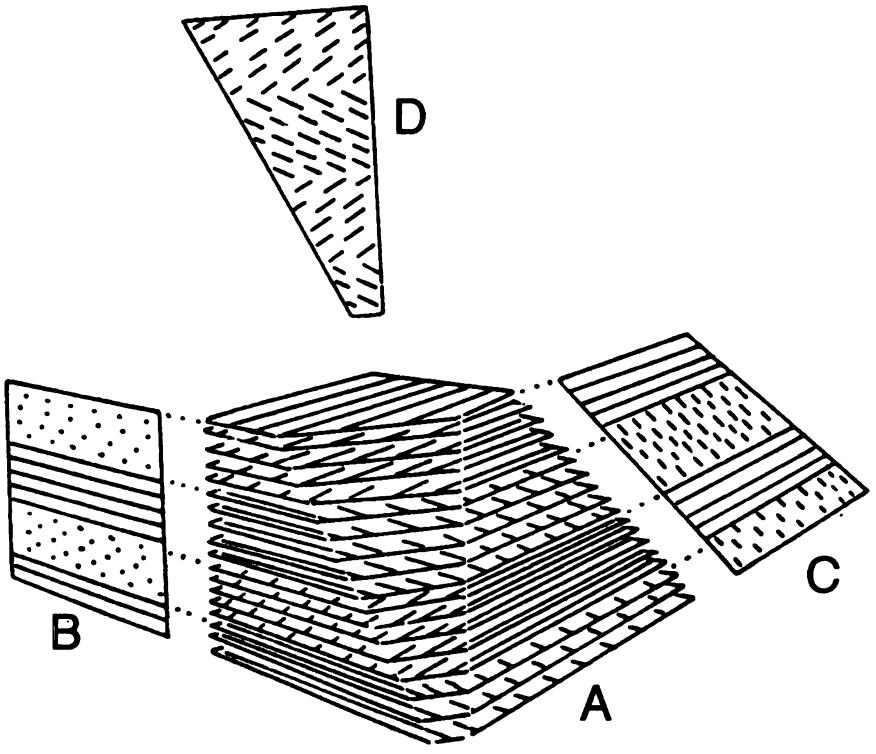

Figure 2.22. Schematic of orthogonal plywood structure of lamellae. A. On each parallel plane, lines indicate the direction of the fibrils. B. A transverse section aligned with the fibrils in some planes and perpendicular to others. C. An oblique plane with one direction parallel to the fibrils in some planes. D. An oblique plane with no directions in common with the collagen fibrils results in a herringbone pattern. From (101).

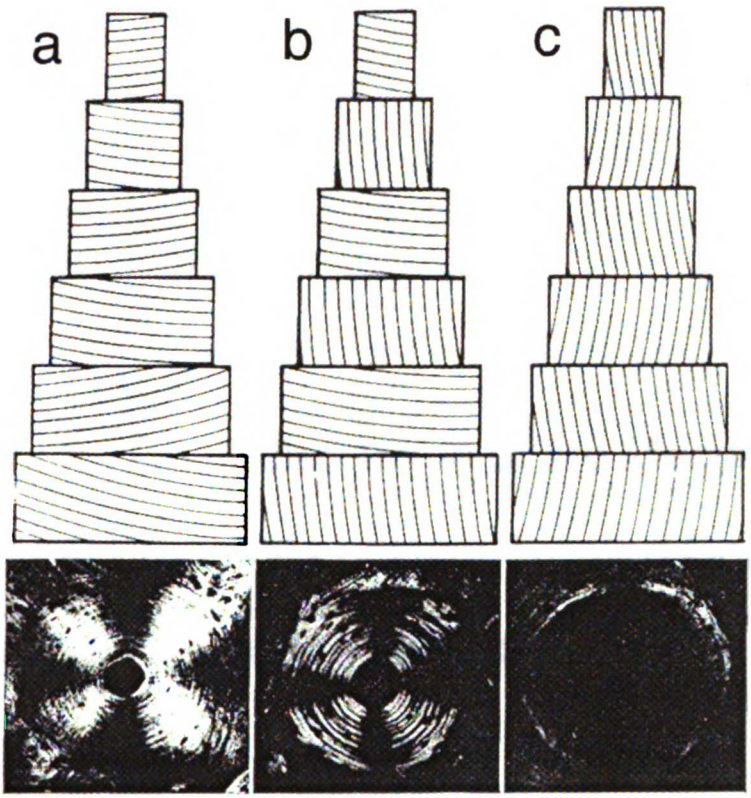

Figure 2.23. Diagrams and polarized light micrographs of light (a), intermediate (b), and dark (c) osteons illustrating the principal orientation of the lamellae in each type of osteon. From (118).

Chapter Three. Characterization of the Mechanical and Ultrastructural Properties of Heat-Treated Cortical Bone for Use as a Bone Substitute

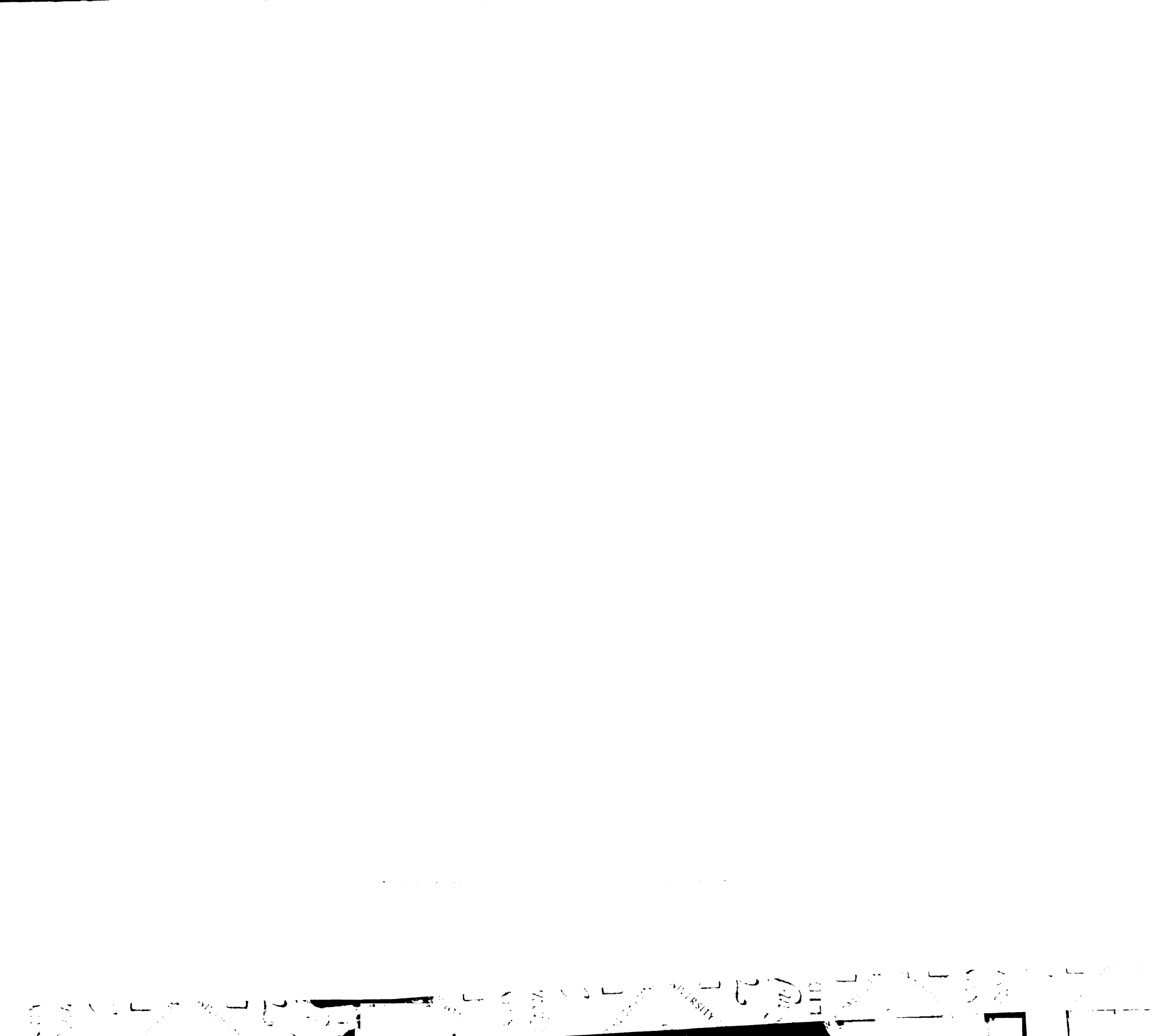

Introduction

While autografts are the most common replacements for human bone tissue, their limited volume and requisite additional surgery indicate a need for alternative strategies (127). The traditional alternatives, allograft and xenograft, overcome these limitations but introduce risks of rejection and disease transfer (128-131). Synthetic biomaterials overcome these limitations but they often lack the osteoinductive properties that real bone offers (132-134), differ structurally from real bone, resorb too slowly after implantation (132, 133, 135, 136), and lack the initial strength required for load bearing applications (137). One strategy to improve non-autograft bone transplant materials is to process natural bone in some manner that eliminates the risks associated with allografts and xenografts while maintaining their advantageous biological and mechanical properties. Toward this end, heat-treated cortical bone has been suggested as an alternative bone transplant material (66, 67, 79).

Although collectively the evidence suggests that heat-treated bone may be an excellent substitute for both bone grafts and synthetic bone substitutes, a complete mechanical and ultrastructural characterization of heat-treated bone has not been performed, thereby undermining its clinical usage. Studies of bone deorganified with methods other than heating (74, 75) have indicated that deorganified bone may have mechanical properties suitable for situations where load is shared between the implant and the surrounding host tissue. The tensile stiffness of ethylene diamine deorganified bone matches that of intact bone (75), which in theory should reduce stress shielding and subsequent resorption from the surrounding tissue compared to a stiffer implant (138). Ultimate compressive strengths ranging from 37 to 47 MPa have been reported for ethylene diamine deorganified bone (74, 75). These values are lower than the strength of cortical bone (139) but much greater than that of trabecular bone (140) or synthetic bone substitutes (137) and are probably high enough for compressive functional loading (141, 142). Taken together, these findings suggest that heat-deorganified bone may be a viable alternative to current bone substitutes

in certain load bearing situations, although a complete mechanical characterization is needed to confirm this.

Electron microscope studies have shown that Haversian canals and other microstructural features are preserved at 500° C (67) and x-ray diffraction studies have shown similar patterns at 400° C (45). These findings suggest that the both microstructure and ultrastructure are unaltered by heat treatment at 400–500° C, which should be advantageous from a biological perspective. However, these previous studies have been qualitative and it is possible that subtle differences existed between intact and heated bone but were not detected. For example, the carbonate content of synthetic apatite, which is similar in chemical composition and crystal size to bone mineral, is changed subtly at 400° C, and this can only be detected by quantitative analysis (143, 144).

The overall goal of this study was to better characterize heat-treated bone for potential use as a bone substitute. Low temperature (400° C and lower) heat treatments were considered since they should minimize microstructural and ultrastructural changes to the bone mineral, remove most of the organic component, and eliminate risk of disease transfer. If the mechanical properties and ultrastructure of this type of heat-treated bone are similar to those of intact bone, this would provide a more confident basis for the clinical use of heat-treated bone in load-bearing situations. Our specific objectives were to: a) Select the heat-treatment protocol (time and temperature) which removes the largest amount of the organic component of bone in the shortest time; b) Compare the elastic and failure properties of intact vs. heat-treated bovine bone in both compression and tension; and c) Compare the ultrastructure of intact vs. heat-treated human bone using infrared spectroscopy and analytical x-ray diffraction. Bovine bone was used in the mechanical analyses since this is the likely source of clinical bone substitute material. Human bone was used in the ultrastructural analysis to add generality to the results since our pilot studies indicated that the effects of heat treatment on ultrastructure were the same for bovine and human bone.

Methods

Specimen Preparation

A preliminary study was performed to determine the time and temperature required to remove the organic component of bone. For this, thirty discs (5 mm diameter, 1.5 mm thick) of bovine cortical bone were machined and assigned to one of five treatment groups (n = 6 per group): 50° C (control), 300° C, 350° C, 400° C and 700° C. Dry weights were measured for all samples after drying at 50° C until the daily change in weight was less than 1%.

For mechanical testing, ten cylindrical samples (5 mm diameter, 22 mm long) were cored from ten bovine humeri (approximately 2 years old) along the diaphyseal axis and then cut in half (11 mm long) to produce 10 pairs of specimens (10 each for intact and heat-treated; Figure 3.1). The ends of each specimen were then ground parallel using a commercial grinding wheel[1] and a custom fixture to hold the specimens. Grinding resulted in specimens approximately 10 mm long and 5 mm diameter for subsequent compression testing between parallel stainless steel platens. Specimens were machined to dimensions comparable to the dimensions and aspect ratios listed in ASTM standards for ceramics and concrete (145, 146) in order to minimize the non-linear toe associated with platens compression testing. Slabs from a different set of 12 fresh bovine humeri were cut into two different specimen geometries to accommodate tension testing of intact and heat-treated samples (Figure 3.1). Intact bone samples were prepared by machining one slab from each bone into a reduced-section geometry (6 mm gage length, 2 mm wide in the gage length, 1.5 mm uniform thickness). Twenty heat-treated tension specimens were prepared in the same manner as the compression samples. Overall, six specimens were damaged during machining, handling, or while being attached into the load frame and were therefore discarded from further analysis. A total of 46 specimens remained: 10 intact compression;

[1] Ecomet I, Buehler Ltd., Lake Bluff, IL

10 heat-treated compression; 8 intact tension; and 18 heat-treated tension.

An additional 11 cylindrical specimens were machined and assigned to an ashed group (700° C treated) to be tested in compression. These were prepared from a different set of four bovine humeri and included to confirm our preliminary observations that ashed bone had an exceptionally low strength and was unsuitable for use as a bone substitute in load bearing applications.

For analysis of the ultrastructure, one ten millimeter thick cross-section was cut from the proximal diaphysis of each of seven fixed human left femora (three females aged 76, 82, and 91 years and four males aged 61, 67, 85, and 89 years). One cylindrical core (5 mm diameter, 10 mm long) was machined from each section (Figure 3.1). Each core was then sectioned into three, four, or five 2 mm thick discs, for a total of 30 discs. Eighteen of the discs were then randomly selected and assigned into one of three groups (n = 6/group) for treatment: intact, heat-treated, and ashed. The remaining 12 discs were saved for use in a separate experiment. The ashed group served as a positive control group for the ultrastructural analysis since crystallographic changes are known to occur in bone mineral when heating above 600° C (67, 79, 144). The intact samples were lyophilized overnight to remove the water and provide more accurate comparisons of dry weight and structural parameters between groups. Dry weight was measured in the heat-treated and ashed groups after dehydrating at 50° C until the change in weight was less than 1% per day.

Heat Treatment

The time-temperature characteristics for removing the organic component of bone were quantified in a preliminary study. Thirty discs (5 mm diameter, 1.5 mm thick) of bovine cortical bone were assigned to each of five treatment groups (n = 6 per group): 50° C (control), 300° C, 350° C, 400° C and 700° C and heated at the assigned

temperature in a muffle furnace[2]. Weights were recorded every 24 hours until the daily change in weight was less than 1% for three consecutive days. All heat-treatments were performed at atmospheric pressure and ambient humidity. To adjust for weight changes due to the variation in the water content of each sample and changes in humidity, the average daily weight change of the control group was subtracted from the measured weight change in each sample. All groups were then normalized to the 700° C group, since 700° C removes all of the organic material in 18 hours (72, 147, 148). This protocol was determined to be the lowest temperature-time combination that removed at least 80% of the organic material from bone in less than one week (see Results section). Based on these results, heating to 350° C for two days was selected as the protocol for further study.

Specimens assigned to the heat-treated groups for mechanical and ultrastructural characterization were then heated at 350° C for 48 hours. Specimens assigned to the control groups were wrapped in saline-soaked gauze and stored at -4° C until mechanical testing was performed. Specimens assigned to the ashed groups were heated to 700° C for 18 hours in order to completely remove the organic component.

Mechanical Characterization

A series of compression and tension tests were conducted to measure the elastic and failure properties of intact and 350° C heat-treated bovine bone. Compression tests were performed on a servo-hydraulic load frame[3] with a one inch extensometer[4] attached to the platens to eliminate the effects of load frame compliance. Before heat treatment, all compression samples were non-destructively tested to a 1200 N compressive load in displacement control at approximately 0.01% strain per second. This provided a measure of the elastic modulus for all specimens before any treatment and a method to justifying the statistical analysis used. After heat treatment, all specimens were tested to failure (3%

[2] FB1300, Thermolyne Corp., Dubuque, IA
[3] Mini-bionix 858 MTS Corp., Eden Prarie, MN.
[4] Model 632.11F-20 MTS Corp., Eden Prairie, MN.

strain) in compression at the same strain rate. The non-destructive nature of the first tests was confirmed by comparing elastic modulus in the non-destructive vs. destructive tests; any damage introduced in the non-destructive test would have reduced the modulus measured in the second test, and this was never observed.

For the tension tests, two different protocols were used to accommodate the different specimen geometries and the brittle nature of the heat-treated bone. The reduced-section tensile intact bone samples were held in aligned wedge grips on a tensile micro stage[5] and loaded to failure at approximately 0.03% strain per second. Load was measured using a 2200 N load cell; strain was measured with a miniature extensometer[6] attached directly to the specimen. The heat-treated specimens were tested similarly to those tested in compression (*i.e.* between parallel stainless steel platens) since reduced-section specimens of heat-treated bone could not be fastened into the wedge grips without fracturing. For these tests, a cyanoacrylate adhesive was used to attach each specimen to the platens. Intact tensile specimens could not be tested in this way because the cyanoacrylate adhesive failed at lower loads than the intact specimens.

Elastic modulus was measured as the maximum slope, measured with a least-squares linear regression over a 0.1% strain range, in the initial linear region of the stress-strain curve. The yield point was defined using the 95% secant method, which is the intersection of the stress-strain curve with the line through the origin having a slope equal to 95% of the elastic modulus. This method is a more sensitive measure of initial non-linearity than the traditional 0.2% strain offset method and is particularly well suited for analysis of brittle materials. The ultimate point was defined at the point of maximum stress.

Ultrastructural Characterization

Carbonate content was analyzed using infrared spectroscopy (149). Small chips

[5] Model 18211 Ernest F Fullam Inc., Latham NY.
[6] Model 632-29C-30 MTS Corp., Eden Prairie, MN, 5 mm gage length.

from each sample were ground in an agate mortar and 1 mg was blended with 300 mg of ground spectroscopic grade potassium bromide. A pellet of pure potassium bromide was also prepared and used as a background reference. Transparent 1/2 inch diameter pellets were pressed in a die under a load of 100 kN. Infrared spectra from 400 cm^{-1} to 4000 cm^{-1} were recorded on a ratio recording infrared spectrophotometer[7]. Carbonate content was determined by comparing the extinction coefficient, E, of the 1415 cm^{-1} (carbonate) and 575 cm^{-1} (phosphate) peaks in the infrared spectra using the formula

$$\%CO_3 = 13.5\left(\frac{E_{1415}}{E_{575}}\right) - 0.2 \qquad (1)$$

where

$$E_i = \log\left(\frac{T_{2,i}}{T_{1,i}}\right), \qquad (2)$$

i is 1415 or 575, and $T_{2,i}$ and $T_{1,i}$ are the transmissions at the peak maximum and local baseline, respectively. These formulae were previously derived by calibration with carbonated apatites of known carbonate content as measured by Conway diffusion (149).

Crystallinity was quantified using x-ray diffraction peak widths and locations at $2\theta = 25.9°$ and $2\theta = 31.8°$, corresponding to the (002) and (211) planes of the hydroxyapatite crystal lattice, respectively. Approximately one milligram of each sample was ground in a mortar and mixed with approximately one milliliter of ethanol. The resulting slurry was then placed on a low background holder. After ethanol evaporation, the sample was scanned from 23°-37° 2θ with a 0.024° 2θ step size and a two second count in an x-ray diffractometer[8]. One sample was selected in each group and scanned from 3°-65° 2θ to check for presence of non-hydroxyapatite mineral phases. Peak width at half maximum and peak centerline location were calculated by fitting Lorentzian curves to each

[7] Model 1430. Perkin-Elmer Corp. Norwalk, CT.
[8] Geigerflex x-ray diffractometer system, Rigaku Corp., Tokyo, Japan.

spectra over the ranges 24°-28° 2θ and 31° -32.5° 2θ using wave analysis software[9].

Statistical Analysis

Elastic modulus was compared before and after treatment for both intact and heat-treated bone in compression using a two-factor repeated measure analysis of variance[10]. In addition to testing of the effects of heat treatment on modulus using a paired design, this analysis enabled us to justify pairing of adjacent samples for subsequent statistical analysis of the compressive failure properties. The repeated measure factors in this analysis were treatment status (before vs. after treatment) and the treatment itself (intact vs. heat-treated). Paired Student's t-tests were then used to compare the compressive failure properties between the intact vs. heat-treated groups. Unpaired t-tests were used to compare elastic modulus and failure properties in tension (intact vs. heat-treated), since these specimens were not collected in a paired manner. Since the ashed samples were taken from a different set of bones and were not part of the main study, they were not included in the statistical analysis.

Carbonate content, x-ray diffraction peak width at half maximum, and peak centerline location were compared using a one-factor analysis of variance[11]. Output variables significant at the 0.05 level were tested for mean differences using the Tukey *post-hoc* test.

Results

The average amount of organic material lost was 84% in both the 350° C and 400° C groups after two days and less than 80% in the 300° C group, even after one week (Figure 3.2). We chose a 350° C-two day protocol for the current experiment since it removed as much of the organic material as heating at a slightly higher temperature and was less likely to alter the mineral phase due to the use of a lower temperature.

---

[9] Igor Pro, WaveMetrics Lake Oswego, OR.
[10] Systat version 5.2, Systat, Inc., Evanston, IL.
[11] Systat version 5.2, Systat, Inc., Evanston, IL.

The elastic modulus (mean ± SD) of the intact and heat-treated bone was the same for both compression (16.3 ± 2.2 GPa, $p = 0.68$) and tension (16.3 ± 3.7 GPa, $p = 0.95$). In compression, the 350° C heat-treated bone was 37% less strong as compared to the intact bone (Table 3.1), behaved in an elastic-brittle manner (Figure 3.3), and had an ultimate strain 38% lower than the intact bone. By contrast, in tension, the 350° C heat-treated bone was much weaker than intact bone, failing at 91% lower stress and 96% lower strain on average than the intact bone (Table 3.2). Both intact and heat-treated samples had oblique fracture patterns in compression and transverse fractures in tension. As expected, some tensile post-yield deformation was observed for the intact bone but not for the heat-treated bone (Figure 3.3). The strong positive linear correlation between the strength of the intact bone vs. heat-treated bone in compression (Figure 3.4; $r^2 = 0.75$, $p = 0.001$) indicated that the compressive strength of the intact bone was a good predictor of the strength of the 350° C heat-treated bone. Ashed (700° C) bone had substantially lower stiffness and strength compared to the intact bone (Table 3.1).

Infrared spectra were qualitatively similar in the intact and heat-treated groups (Figure 3.5) indicating that heat-treatment had little effect on the carbonate content of the mineral. There was a small but not statistically significant reduction in the amount of carbonate present after heat-treatment at 350° C (6.3 ± 0.6% vs. 5.4 ± 0.3% for intact vs. 350° C heat-treated bone, respectively, $p = 0.12$). As expected, ashing at 700° C reduced the carbonate content (6.3 ± 0.6% vs. 2.8 ± 1.0% for intact vs. ashed, respectively; $p < 0.001$), confirming the validity of our ultrastructural analysis techniques.

The similarity between the diffraction patterns of the intact vs. 350° C heat-treated bone indicated that there was little qualitative change in crystallinity caused by the heat-treatment (Figure 3.6). Quantitative analysis of the 25.9° and 31.8° peaks confirmed this observation. Peak width at half maximum height, $\beta_{\frac{1}{2}}$ — an inverse measure of crystal size and crystallinity — was not significantly different for intact vs. heat-treated bone at either 25.9° or 31.8° ($p = 0.12$, $p = 0.23$, respectively; Table 3.3). This indicates that no major

change occurred in the c-axis dimensions of the mineral after heating at 350° C. Peak centerline location, a measure of the average lattice spacing in the c-axis direction, was not significantly different among intact, 350° C heat-treated, and ashed bone at either 25.9° or 31.8° ($p = 0.08$, $p = 0.09$, respectively). The measurement of peak centerline location was confounded at 31.8° in the intact and 350° C heat-treated groups due to the overlap of the 31.8° peak with a second peak at 32.3°. The difference in the centerline locations measured from 30-32.5° was negligible ($32.10 \pm 0.08°$ vs. $32.00 \pm 0.03°$ for intact vs. heat-treated). No mineral phases besides hydroxyapatite were observed in the longer (3°-65° 2θ) scans. As expected, ashing at 700° C caused substantial changes in the mineral diffraction pattern compared to both the intact and 350° C heat-treated bone; the background signal was reduced and peaks were more distinct and sharper (Figure 3.6). Ashing reduced $\beta_{\frac{1}{2}}$ by 51% and 72% for the 25.9° and 31.8° peaks, respectively, compared to the intact group (Table 3.3; $p < 0.001$).

Discussion

Previous studies have shown that bone heated to 400–500° C is a good candidate for a bone substitute material from a biological perspective since it maintains the microstructural (67) and ultrastructural (45, 67) features of intact bone and is also biocompatible (66). Our findings extend some of these results to bone heated to 350° C, demonstrating substantial similarities in both ultrastructure and elastic modulus compared to intact bone. Maintaining ultrastructure should help promote biological integration of the implant. Matching the modulus of the implant with that of the surrounding bone should avoid the stress overload and stress shielding of surrounding bone that is associated with use of implants that differ in stiffness from the adjacent bone (138). In these respects, the 350° C heat-treated bone appears well suited as a bone substitute, but this does not address whether or not the implant is suitable for load bearing situations. Habitual *in vivo* strains on human cortical bone rarely exceed 2,000 microstrain (0.2% strain) (141, 142). Using a modulus of 16 GPa for human cortical bone, this strain corresponds to a maximum habitual

stress of 32 MPa. The high value of compressive strength (108 MPa) found here for the 350° C heat-treated bone indicates that this material possesses a factor of safety of over three for these habitual loads. It follows then that this material may be well suited for use in compressive load bearing applications.

A number of aspects of this study support the validity of our results. First, careful mechanical testing techniques ensured axial yield rather than buckling failure modes in the compression tests, thereby providing accurate compressive mechanical properties. For example, ends of the cylindrical samples were ground and polished in a custom fixture to ensure parallel ends and complete contact with the loading platens; extensometers were used to eliminate the effects of compliance in the test system from the strain measurements. Second, the use of paired samples for mechanical testing in compression increased the power (1-beta > 0.99 for paired strength comparison) of the modulus and strength comparisons relative to an unpaired test, justifying the use of relatively small sample sizes. Third, the quantitative analysis of ultrastructure enabled a statistical comparison rather than a qualitative one where subtle changes may not be detectable. Lastly, the use of specimens taken from 22 bovine humeri for mechanical testing and 7 human femora for ultrastructural analysis provides confidence that similar results can be expected for any type of cortical bone heated to 350° C as described here.

While the results from this study suggest that 350° C heat-treated bone is well suited for compressive load-bearing applications, some limitations must be recognized. First, the composition of the organic material that remained in our heat-treated samples is not known. The presence of this material is unlikely to be problematic *in vivo* since the biocompatibility of bone heated to 400° C has been demonstrated previously (66) and we found a negligible difference in the amount of organic material in 350 vs. 400° C heat-treated bone. In addition, the absence of most of the organic components should not hinder biocompatability, since the biocompatability of (completely deorganified) bone heated to 1200° C (79) and pure hydroxyapatite (150, 151) have also been demonstrated. From a

biomechanical perspective, the presence of this remaining organic material is crucial since it helps maintain the desirable elastic and compressive strength properties measured for 350° C heat-treated bone as compared to 700° C ashed bone (see Table 3.1). Thus, our results demonstrate that a small amount of organic material can substantially alter the mechanical properties of heat-isolated bone mineral. However, while only a small amount of organic material is required to maintain most of the compressive strength, tensile strength is much more sensitive to the presence of this material.

A second limitation is that the ultrastructural analysis was performed on fixed human bone, which may respond differently to heat treatment than non-fixed bone. This limitation may not be important since structural differences between fixed and non-fixed bone after heating are likely to be small since fixatives alter only the organic components, which were mostly removed by heating. A third limitation is that the ultrastructural properties of bovine bone were not measured. In defense of this, a study of four samples of heat-treated bovine bone indicated that bovine and human bone ultrastructure were affected similarly by heat-treatment. A fourth limitation was that the specimen geometry was different in the intact tensile samples compared to all other groups. This difference was unavoidable due to the brittle nature of the heat-treated bone in tension and the high tensile strength of intact bone compared to the cyanoacrylate adhesive. However, no significant differences were found between the tensile and compressive elastic moduli of either intact or heat-treated bone, suggesting that the two test methods produce similar results.

There is close agreement between the results presented here and those in the literature for mechanical properties in tension but not for compression (Table 3.4). Mechanical properties have not been reported previously for heated bone, but have been reported for bone deorganified using ethylene diamine (74, 75). While it has been suggested that this technique damages the mineral phase (46, 152), it does remove more than 99% of the organic material (60) and yields a contiguous, mechanically intact material (60, 74, 75). The agreement in tensile properties — both modulus and strength — of

ethylene diamine and 350° C heat-treated bone (Table 3.4) suggests that these materials are similar mechanically. The discrepancy in compressive properties is therefore most probably due to limitations in the previous testing techniques. One possible source of error is the large aspect ratio used in previous tests, 4:1 (75) and 10:1 (74), which can promote buckling and therefore lower strengths compared to the 2:1 aspect ratio used here. Since elastic deformations are due to atomic bonds stretching and rotating, tensile elastic modulus should be equal to the compressive modulus, unless there is damage in which case compressive modulus should be higher. The only previous study that measured both tensile and compressive moduli reported a lower compressive modulus (75), whereas we found equal moduli. This discrepancy may be due to the inclusion of load frame compliance in strain measurements combined with deformations due to buckling in the previous study (74, 75). The consistency in tensile properties, both modulus and strength, across all previous studies provides evidence that the trends reported in this study do not depend on anatomic site.

The ultrastructural analyses confirm that heating at 350° C does not significantly affect the mineral phase of bone. Overall, our ultrastructural analyses agree with previously published reports on the structure of both heat-treated and intact bone (45, 67, 79, 143, 144). The results from our infrared spectroscopy agree with those found previously for synthetic apatites (144): carbonate content was slightly reduced by heating at temperatures of about 350° C and substantially reduced at higher temperatures such as 700° C. The same trends were seen in x-ray diffraction patterns and they also agree with published results which showed broad peaks for intact bone (79) and bone heated at 400° C (45) and sharp peaks for bone heated at temperatures above 600° C (45, 79). The sharp and distinct peaks observed for 700° C ashed bone indicates that heating at high temperatures (600-700° C) causes substantial improvements in crystallinity and increases in crystal size. The similarities in the ultrastructure of intact and 350° C heat-treated bone suggest that 350° C heat-treated bone should be biocompatible since it closely mimics a material already present

in the body, but this remains to be confirmed. However, one discrepancy remains. We found that the 350° C heat treatment removed 84% of the organic material from 1–2 mm thick specimens, whereas complete removal was reported elsewhere using a hydroxyproline analysis on 10 mm thick specimens heated to just 300° C (67). This discrepancy is not easily explained but may be due to inaccuracies in determining the amount of organic material. Weight analysis, used in this study, can be biased towards higher values since we have found that water vapor can contaminate the samples. We used a control group to minimize this effect. Hydroxyproline analysis may be biased towards lower values if heating damages or preferentially removes the hydroxyproline.

Assuming that 350° C heat-treated cortical bone is biocompatible and osteoconductive, successful clinical usage will depend largely on its biomechanical performance. From this perspective, an ideal load-bearing implant should possess two characteristics, which depend in part on whether the implant shares load with, *i.e.* is loaded in parallel to, the surrounding bone, or, simply transmits load in series with the surrounding bone. The first characteristic relates to the elastic modulus. For load sharing, the stresses on the implant and adjacent bone depend on their relative moduli (Figure 3.7). The modulus of the implant should be matched to that of the bone to avoid both overloading and stress shielding of the bone, which increase the risk of bone damage and resorption, respectively. By contrast, for load transmission, the modulus of the implant needs to be large enough to minimize deformation and maintain stable function (Figure 3.7). The second characteristic relates to strength. Regardless of whether the implant is in a load sharing or transmission mode, the strength of the implant must be sufficient to withstand the functional demands. The matched elastic moduli of intact vs. 350° C heat-treated bone indicates that the latter has the ideal characteristics in terms of its elastic modulus when used adjacent to cortical bone. Its high modulus compared to trabecular bone suggests that it may promote resorption if loaded in parallel with trabecular bone, but would be highly stable if loaded in series (*e.g.* between host trabecular bone and a

prosthesis). The high compressive strength of the 350° C heat-treated bone indicates that it should maintain structural integrity when loaded *in vivo* in compression. However, it should be realized that this implant has poor tensile strength, and we have not investigated its fatigue or shear strengths. While it is possible that these strengths may increase with biological integration, we recommend that this type of bone substitute be used only for compressive loading bearing applications and only after sufficient compressive fatigue strength has been verified.

Table 3.1. Compressive mechanical properties of intact vs. 350° C heat-treated (paired samples), and 700° C ashed bovine cortical bone.

Mechanical Property	Intact (n = 10)	Heat-treated (n = 10)	Ashed (n = 11)	Average % Reduction †	p-value
Elastic modulus *before* treatment (GPa)	16.3 ± 1.9	16.9 ± 1.3	—	—	0.68*
Elastic modulus *after* treatment (GPa)	16.1 ± 1.8	15.7 ± 3.2	1.7 ± 1.1	—	0.68*
Yield stress (MPa) ††	170 ± 20	108 ± 32	7.0 ± 5.9	37	0.00002
Yield strain (%) ††	1.24 ± 0.27	0.77 ± 0.22	0.51 ± 0.44	38	0.0001

All values are mean ± SD.

† Average % reduction is for the 350° C heat-treated bone compared to the intact value and is reported for significant ($p < 0.05$) differences only.

†† Yield and ultimate points were coincident.

* All four measures of elastic modulus were compared using a two-factor repeated measure analysis of variance. The repeated measure factors were treatment status (before vs. after treatment) and the treatment itself (intact vs. heat-treated). No significant effects were observed (16.3 ± 2.2 mean ± SD for all 40 measurements; $p = 0.68$).

Table 3.2. Tensile mechanical properties of intact vs. 350° C heat-treated bovine cortical bone (unpaired samples).

Mechanical Property	Intact Bone (n = 8)	Heat-treated Bone (n = 18)	Average % Reduction †	p-value
Elastic modulus (GPa)	16.2 ± 3.4	16.3 ± 4.0	—	0.95
Yield Stress (MPa)	46.8 ± 14.9	7.50 ± 2.70 ††	84	0.0001
Ultimate Stress (MPa)	79.1 ± 19.2	7.50 ± 2.70 ††	91	0.0004
Yield strain (%)	0.26 ± 0.10	0.05 ± 0.01 ††	81	0.00001
Ultimate Strain (%)	1.20 ± 0.38	0.05 ± 0.01 ††	96	0.00006

All values are mean ± SD.

† Average % reduction is for the 350° C heat-treated bone compared to the intact value and is reported for significant ($p < 0.05$) differences only. All properties were compared using an unpaired t-test.

†† Yield and ultimate properties were the same for the heat-treated bone due to its brittle nature.

Table 3.3. Structural and compositional data for intact, 350° C heat-treated, and 700° C ashed human (fixed) cortical bone.

Property		Intact	Heat-treated	Ashed	p-value
organic removed	(%)	NA	85.6 ± 3.6	100†	NA
carbonate content	(%)	6.3 ± 0.63	5.4 ± 0.33	2.8 ± 1.0	< 0.0001
$\beta_{\frac{1}{2}}$ (25.9°)	(° 2θ)	0.530 ± 0.098	0.444 ± 0.038	0.255 ± 0.026	< 0.0001
$\beta_{\frac{1}{2}}$ (31.8°)	(° 2θ)	1.300 ± 0.108	1.219 ± 0.058	0.368 ± 0.045	< 0.0001
peak location (25.9°)	(° 2θ)	25.96 ± 0.13	25.82 ± 0.06	25.90 ± 0.04	0.08
peak location (31.8°)	(° 2θ)	32.10 ± 0.08	32.00 ± 0.03	31.83 ± 0.05	0.09

All values are mean ± SD.

† Ashed bone was assumed to be completely deorganified (72, 147, 148).

P-values are for one-factor analyses of variance. For all significant differences found with the analysis of variance, the ashed group was significantly different than both intact and heat-treated bone ($p < 0.001$, all cases) using a Tukey *post-hoc* test. Differences between intact and heat-treated bone were not significant: carbonate content, $p = 0.12$; $\beta_{\frac{1}{2}}$ (25.9°), $p = 0.12$; $\beta_{\frac{1}{2}}$ (31.8°), $p = 0.23$.

Table 3.4. Review of average mechanical properties of deorganified bovine cortical bone. Neither range nor standard deviation values were reported in previous studies.

Author	Deorganification Technique	Anatomical Site	Elastic Modulus (GPa)	Ultimate Strength (MPa)
Compression:				
Mack, 1964 (75)	ethylene diamine	tibia	6.7	47
Sweeney *et al.*, 1965 (74)	ethylene diamine	femur	7.7	36.9
Current study	heat treatment	humerus	15.7	108
Tension:				
Mack, 1964 (75)	ethylene diamine	tibia	17.2	5.8
Sweeney *et al.*, 1965 (74)	ethylene diamine	femur	NR	6.8
Current study	heat treatment	humerus	16.3	7.5

NR = not reported.

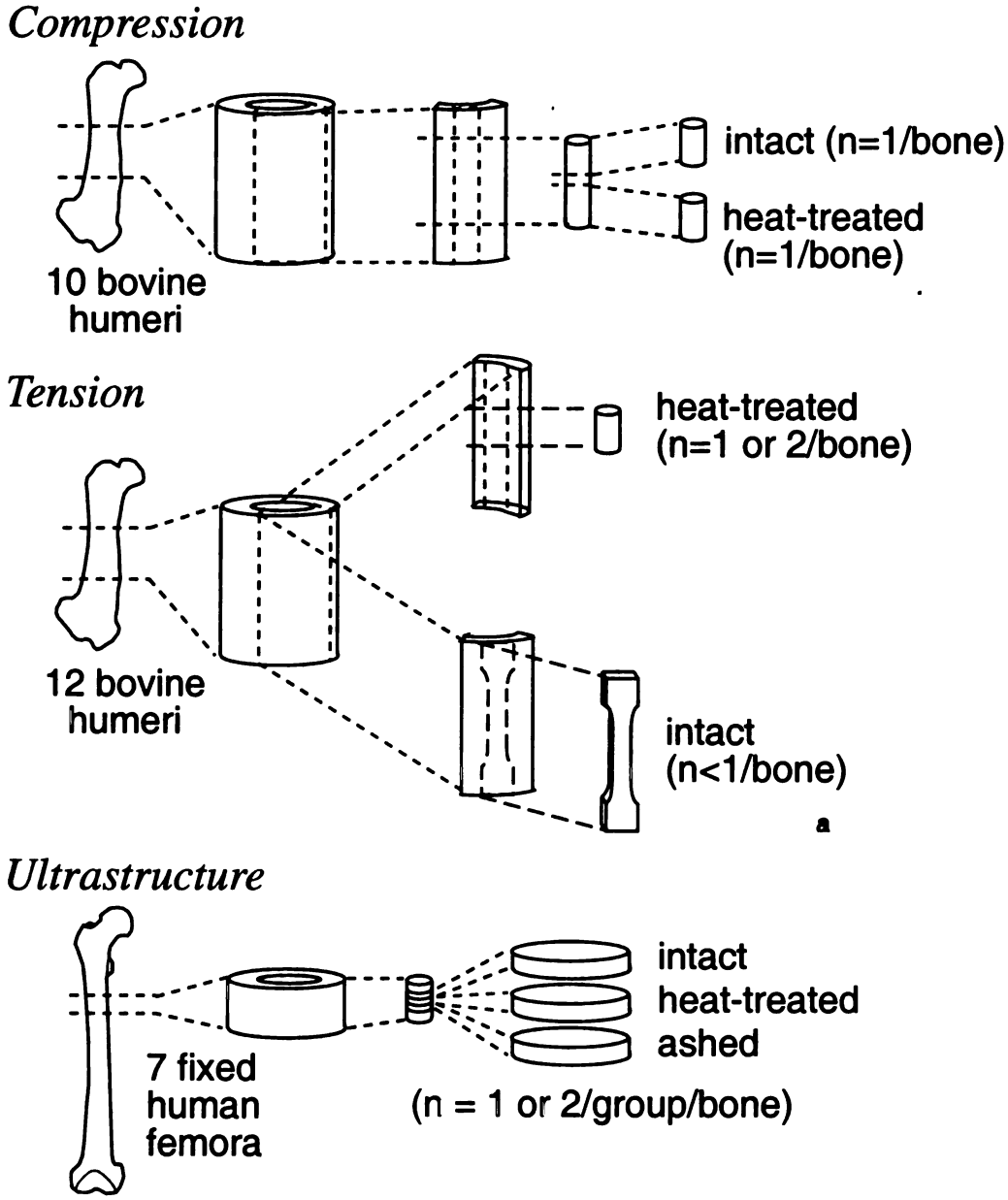

Figure 3.1. Schematic of specimen preparation (not to scale) for mechanical testing in compression (top) and tension (middle) and ultrastructural analysis (bottom), showing the number of specimens harvested from each bone. Due to the brittle nature of the heat-treated bone, it was necessary to use different geometries for mechanical testing in tension to ensure accurate data.

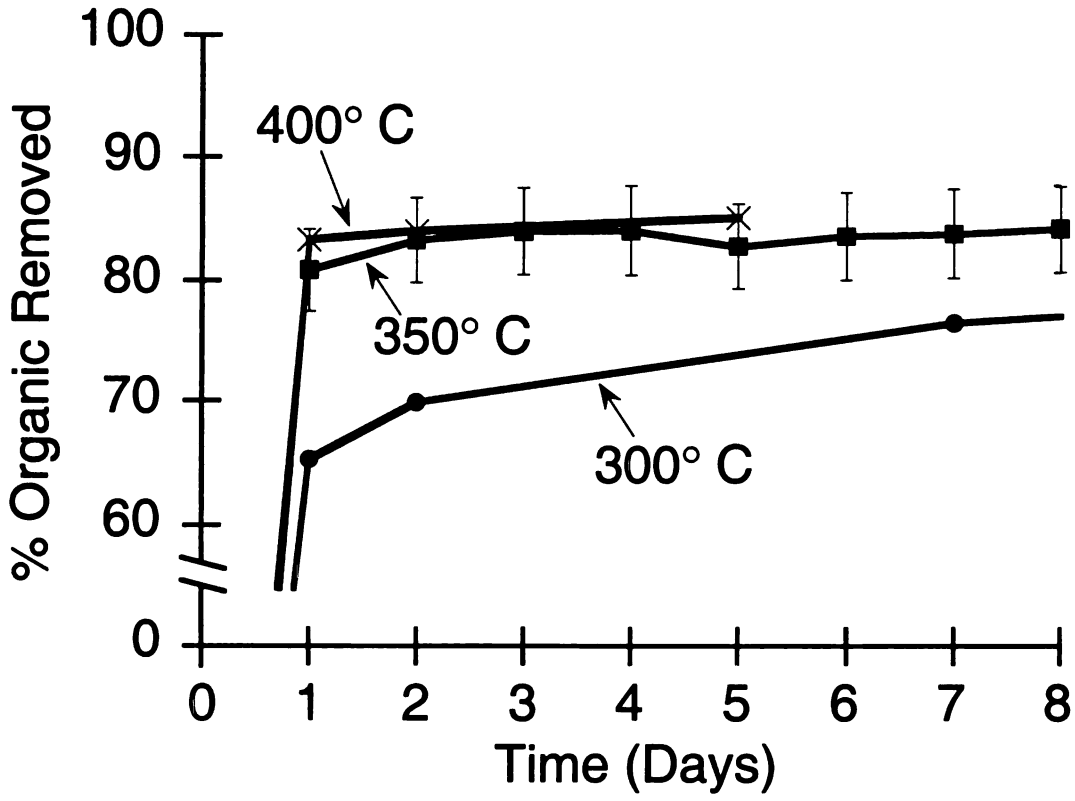

Figure 3.2. Average percentage of organic material removed from bovine cortical bone by heating, vs. time. Responses are shown for groups of specimens heated to either 300° C, 350° C or 400° C. Each datum is the average response of six samples. Data were adjusted for water content using control (50° C) group. For clarity, standard deviation error bars are shown only for the 350° C group; similar standard deviations were seen in each group. Based on these data, we chose a protocol for heating at 350° C for two days as the main treatment for this study.

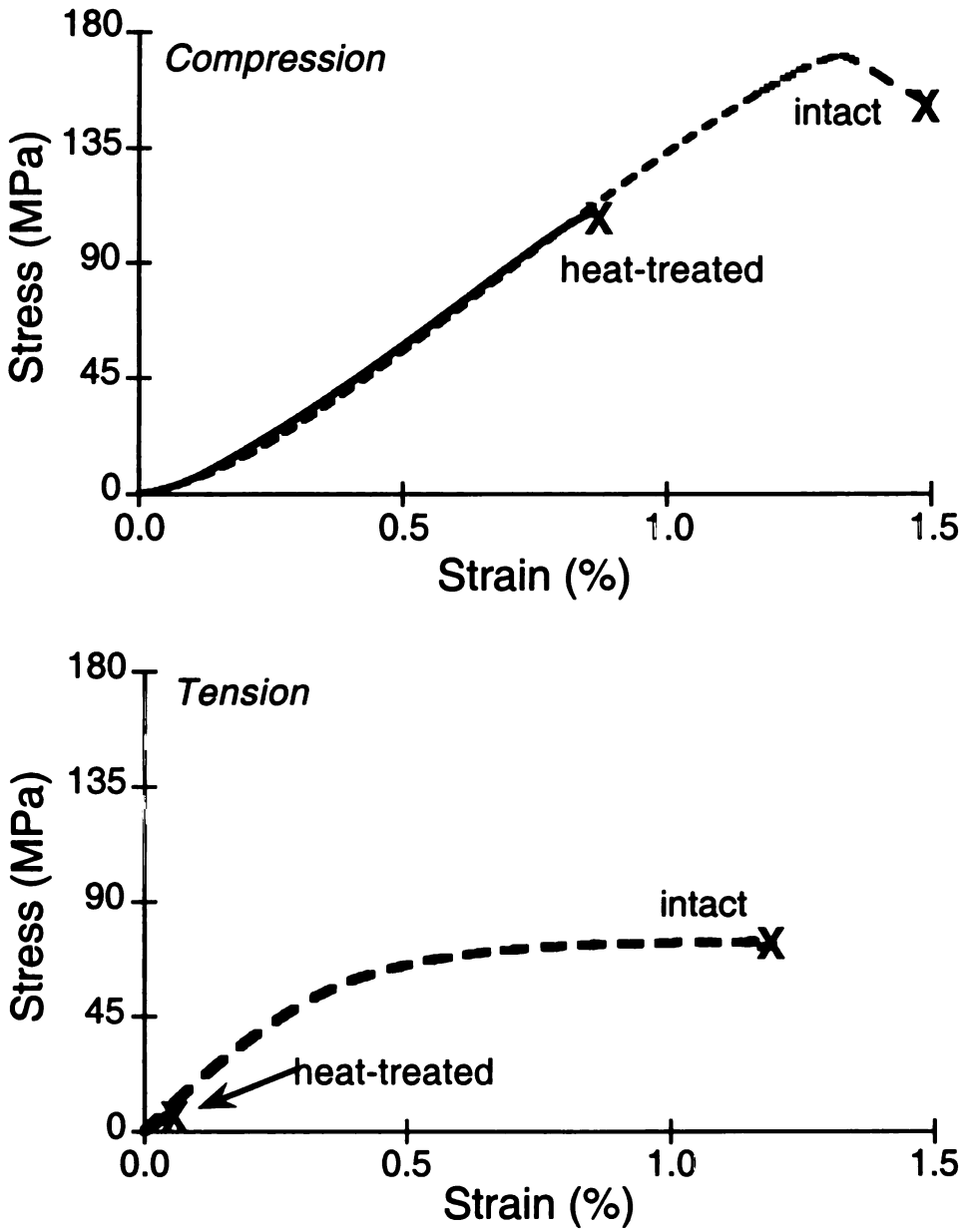

Figure 3.3. Typical compressive (top) and tensile (bottom) stress-strain curves of intact (dashed lines) and 350° C heat-treated (solid lines) bone. The fracture point for each specimen is shown with an "X". Compression samples shown are for two paired specimens taken from the same bone; tension samples are for unpaired samples taken from different bones. In general, elastic moduli were the same for both groups in tension and compression; the strength of the heat-treated bone was only 37% lower than the strength of the intact bone in compression, but was 91% lower in tension.

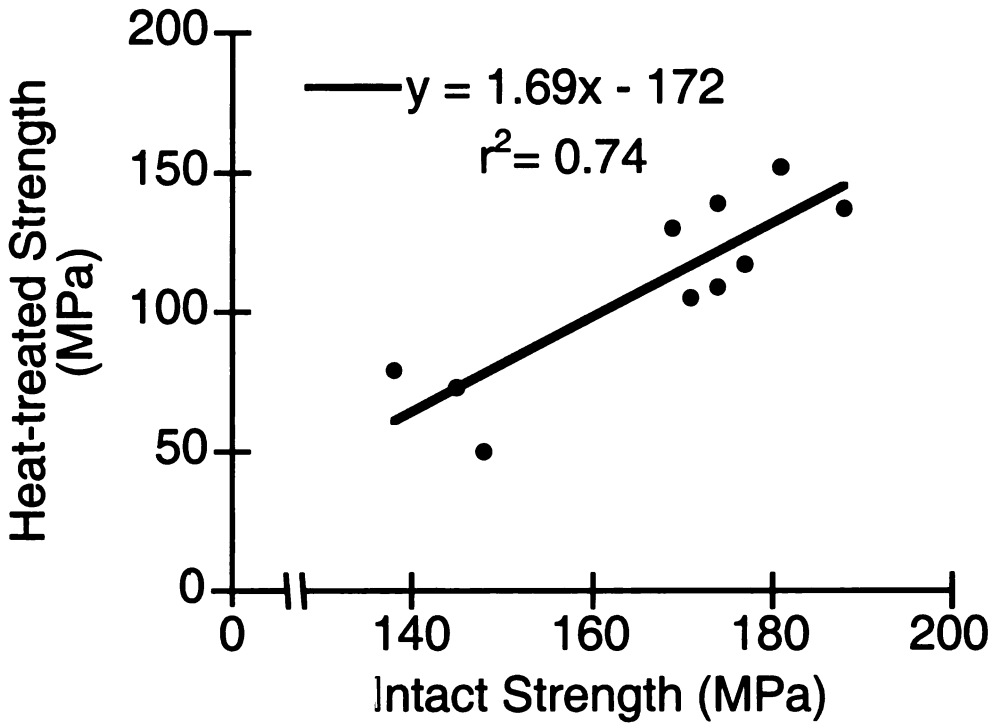

Figure 3.4. Relationship between the compressive yield strength of 350° C heat-treated vs. intact bone. The yield point was defined using the 95% secant method (see text). A strong correlation ($p = 0.001$) between the two variables indicates that the intact compressive strength was a good predictor of the heat-treated strength. Due to the brittle nature of the heat-treated bone and the different geometries used for mechanical testing in tension, regression analysis between intact and heat-treated tensile strength was not possible.

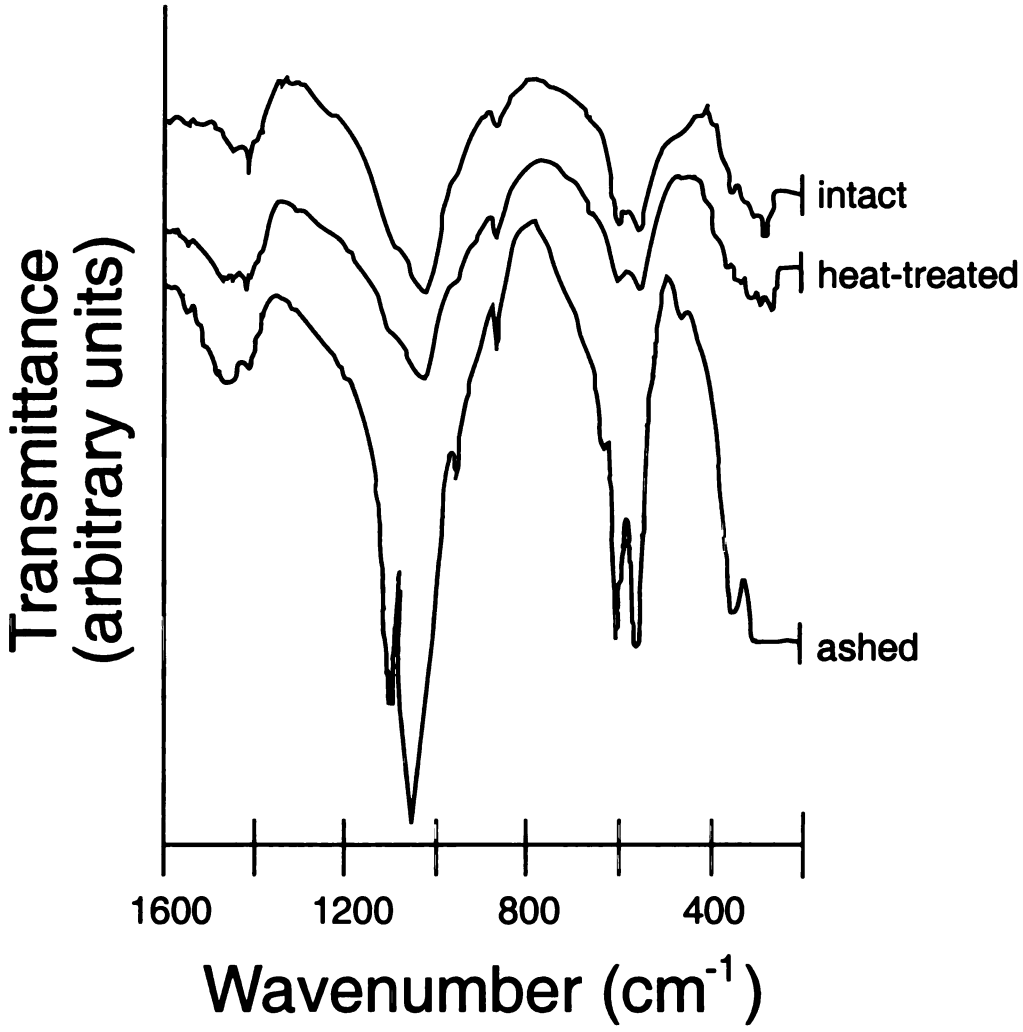

Figure 3.5. Typical infrared spectra of intact, 350° C heat-treated, and 700° C ashed bone. There was no difference between the spectra of the intact vs. heat-treated bone. However the carbonate bands (1415 cm^{-1}) were diminished relative to the phosphate bands (575 cm^{-1}) in the ashed group, indicating that a reduction in the amount of carbonate only occurred after ashing.

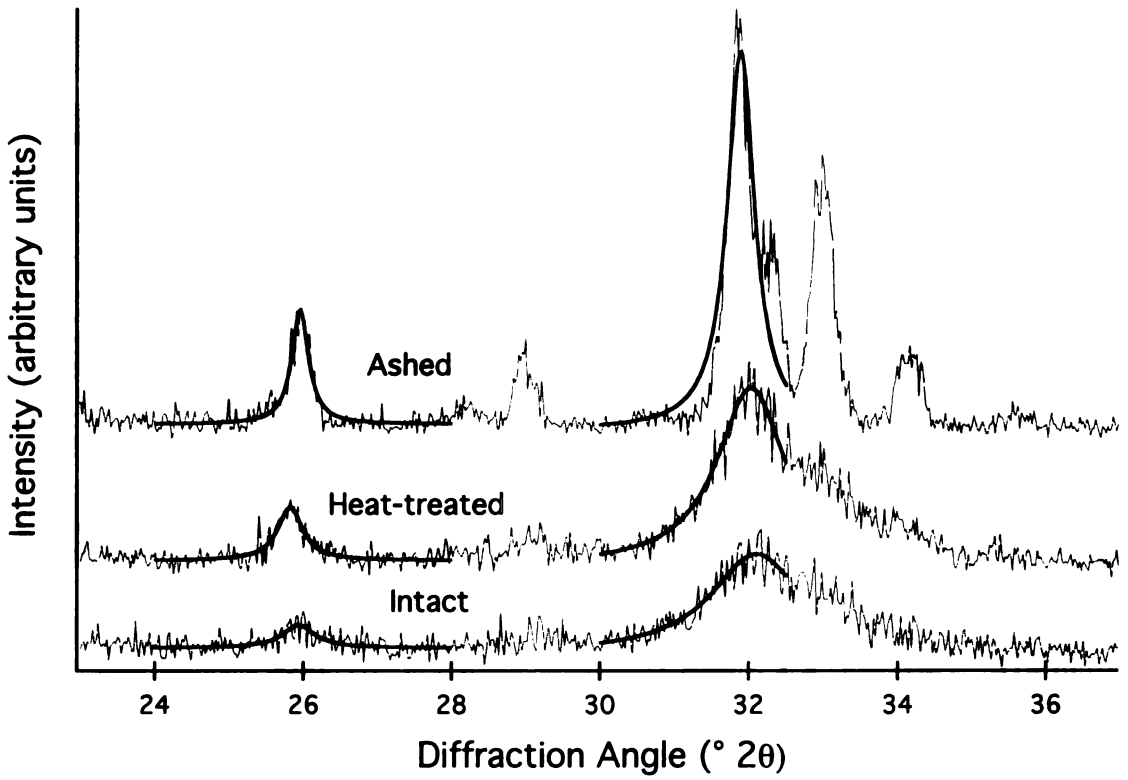

Figure 3.6. Typical X-ray diffraction spectra of intact, 350° C heat-treated, and 700° C ashed bone with Lorentzian curve fits superimposed. Compared to the intact group, peak widths at half-maximum were significantly different in the ashed group only ($p < 0.001$). No significant differences in peak centerline locations were found between any groups (25.9°: $p = 0.08$, 31.8°: $p = 0.09$). These results indicate that heat-treatment at 350° C had no effect on the size, crystallinity, or lattice spacing of the crystals.

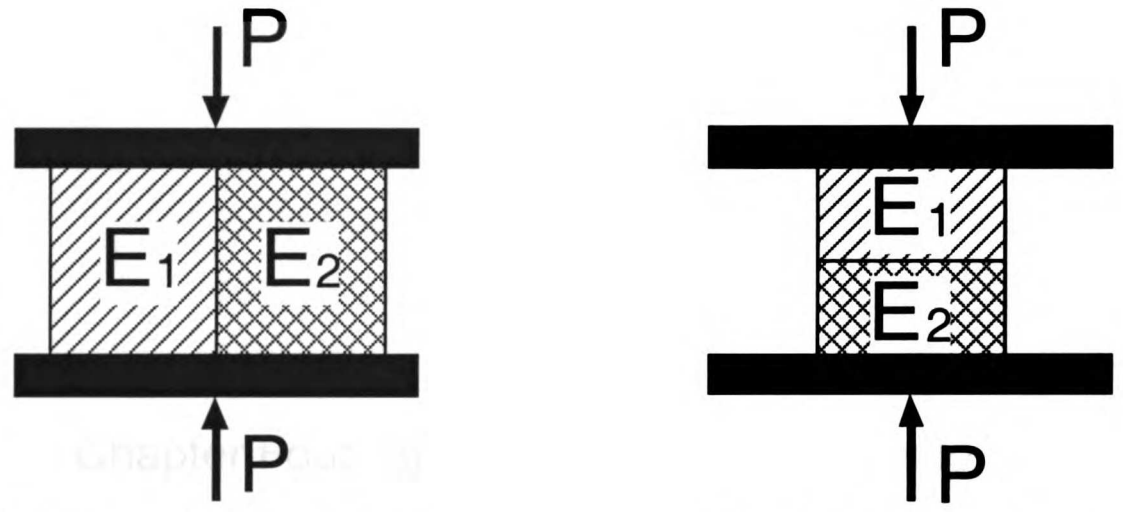

$$\sigma_1 = \frac{E_1}{E_2}\sigma_2$$

$$\sigma_1 = \sigma_2$$

Figure 3.7. Axial load sharing (left) and transmission (right) configurations illustrated with parallel and series models where P is the applied axial force, E_1 and E_2 are the elastic moduli of materials 1 and 2, respectively, and σ_1 and σ_2 are the corresponding stresses. In load sharing configurations, more axial force is carried by the stiffer material in proportion to the ratio of elastic moduli of the two materials. Thus, if an implant is much stiffer than the adjacent bone, "stress-shielding" the bone will occur, increasing the chances of bone resorption. Conversely, if the bone is much stiffer than the implant, overloading of the bone will occur, increasing the chances of bone failure. In a series configuration, the total applied axial force is carried by each material. Similar concepts apply for bending loads.

Chapter Four. Species and anatomical site heterogeneity of bone collagen

Introduction

Successful treatment of bone diseases that are manifested as a reduction in the mechanical properties requires understanding the relationship between the mechanical properties of bone, and how age- and disease-related changes of its constituents affect these properties. For example, osteogenesis imperfecta, Paget's disease, osteoporosis, and aging all adversely affect the mechanical properties of bone (153). Specifically, reductions in ductility and strength are seen with normal aging (10, 19, 23) and large reductions in ductility are seen in a murine model of osteogenesis imperfecta (154). It has been suggested that some of these changes are due to changes in the structure of the underlying collagen (155, 156) but this has never been investigated.

The mechanical properties of both intact bone and isolated bone collagen have been well documented (122, 139). Nonetheless, it is difficult to investigate the role of collagen in the mechanical properties of bone due to the large discrepancies reported for isolated bone collagen (74, 75, 156-159). The only explanation for these discrepancies so far has been differences in mechanical testing technique, but since each previous study examined bone from only one species and anatomical site, it is possible that these differences are due to species and site-related variations in the weight fraction or microstructure of the collagen. Additionally, the mechanical properties of bovine and human bone collagen have never been compared, so the use of a bovine model to investigate age- and disease-related effects in intact bone and bone collagen has not been substantiated. Thus, an important step in relating the mechanical properties of isolated bone collagen and intact bone is to explain these discrepancies in the mechanical properties of bone collagen.

The overall goal of the current experiment was to investigate the heterogeneity of isolated collagen mechanical properties. If differences in properties are due to the species and anatomical site of the testing material rather than the testing techniques, this would suggest that significant differences in either weight fraction or microstructure exist in bone collagen from different species and anatomical sites, and motivate further study into the

structure-function relations for bone collagen. The specific objectives were to: 1) compare the mechanical properties of isolated bone collagen from difference species and anatomical sites; and 2) assess the adequacy of a bovine model in investigating age- and disease-related changes in human bone. This experiment constitutes the first part in a series of experiments aimed at improving the understanding of the role of collagen in the mechanical properties of bone.

Methods

Uniaxial tension tests were conducted to measure the elastic and failure properties of demineralized human and bovine cortical bone. Right human femora (n = 17) and tibiae (n = 15; from the same set of 13 males and four females ranging in age from 49 to 101; mean ± SD of 70.4 ± 15.4 years) were obtained from national tissue banks[1]. Two more femora compared to tibiae were used in the experiment since tibiae were not available from two of the 17 cadavers. Bones were excluded if there was any record of liver, kidney, or bone diseases, malignancy or cancer, vitamin D deficiency, drug use, Cushing's disease, or hypo- or hyper-thyroidism in the donor. Bovine (approximately 2 years old) humeri (n = 8) and tibiae (n = 10) were obtained from local meat suppliers. One longitudinal slab was cut from the diaphysis of each bone on a band saw (Figure 4.1). The slabs were mounted in a custom jig, submerged in isotonic saline and machined to final shape (1.8 x 3.0 x 18 mm gage section) on a computer-controlled mill[2] such that the specimen was aligned with the long axis of the bone. One sample was obtained from each bone. Human humeri and tibiae were harvested from the same individuals but, since only right legs were used, there was only one sample from each donor in each group. Bovine bones were received without the epiphyses, therefore identification of the left and right sides was not possible; thus the bovine specimens were harvested from between four and eight animals

[1] National Disease Research Interchange, Philadelphia, PA; University of California, Davis School of medicine, Davis, CA; Anatomical Gift Foundation, Phoeniz, AZ
[2] LM2000, Light Machines Corp, Manchester, NH.

for the humeri and a different five to ten animals for the tibia.

After machining, specimens were demineralized by soaking in 0.5 M ethylenediamine tetraacetic acid for 4 days with fresh solution every day. The ends of each specimen were coated with paraffin wax to prevent demineralization in the ends in order to enhance attachment into the load frame. After mechanical testing, portions of the gage length of each specimen were ashed at 700° C for 24 hours to verify that the samples had been completely demineralized.

All specimens were tested in uniaxial tension on a servo-hydraulic load frame[3] in displacement control, corresponding to an approximate strain rate of 0.30%/second. The load history was similar to that used by Bowman *et al.* (158), consisting of nine pre-conditioning cycles between zero and approximately 3% strain followed by a large strain (>25%) to failure. Specimens were attached to the load frame using two-jaw self-centering chucks with a recess machined into the grip faces to ensure axial alignment of the specimen. Load was measured with a 1,112 N load cell set to a 556 N range. Strain was measured with a soft-tissue extensometer[4] designed to minimize the lateral force that the extensometer exerted on the specimen. Because the soft-tissue extensometer separated from the specimens during some of the tests, the displacement measured from the load frame LVDT was also used to calculate strain (Appendix A). The effective gage length for each specimen was calculated by dividing the total displacement (measured with the LVDT) by the strain (measured with the soft-tissue extensometer) in the region that the extensometer was attached to the specimen. The displacement measured from the LVDT was then divided by the effective gage length in order to calculate the strain over the entire loading history. In this method, the strain measured from the LVDT and the soft-tissue extensometer were, by definition, equal in the initial portion of the stress-strain curve.

[3] Mini-bionix 858 MTS Corp., Eden Prarie, MN.
[4] Model 632.29c-30, MTS Corp., Eden Prarie, MN.

Elastic modulus was measured as the maximum slope, using a least-squares linear regression over a 1% strain range, of the initial linear region of the stress-strain curve. The ultimate point was defined at the point of maximum stress. In most cases, the specimens failed at the ultimate strain and thus the ultimate strain and strain-to-failure were usually coincident. Accordingly, only ultimate strain was reported (Table 4.2). The strain-to-failure was defined as the strain at the point where the specimen could no longer bear any load. Complete demineralization was verified by ashing a small portion of the gage length of each specimen at 700° C for 24 hours after mechanical testing. Demineralization was determined to be complete if there was no visible mineral in crucibles after ashing and the weight lost in each crucible was greater than 99% of the demineralized specimen weight. Eleven of the original 50 specimens were excluded due to incomplete demineralization (n=3), pulling out of the grips (n=5), or the presence of vascular channels in the gage length of the specimen (n=3). A total of 39 specimens were therefore included in the analysis: 10 from human femora, 13 from human tibiae, 8 from bovine humeri, and 8 from bovine tibia. All mechanical properties were compared between groups using a one-factor analysis of variance with a Fisher LSD post-hoc test[5].

Results

All specimens exhibited a non-linear toe region followed by a linear region extending to 8.3% strain, on average (Figure 4.2). All specimens appeared to fail in a slightly oblique manner either in the gage length or in the fillet region. Closer inspection of the oblique failure surface revealed a stair-step pattern where layers of fibers created individual steps with transverse failure surfaces perpendicular to the stair-step (oblique) direction.

The elastic modulus and ultimate stress of isolated bone collagen varied with both species and anatomical site ($p = 0.02$ and $p = 0.03$, respectively; Table 4.2). In particular,

[5] Systat version 5.2, Systat, Inc., Evanston, IL.

ultimate stress was different for the different species (25.5 ± 4.7 MPa vs. 18.2 ± 4.8 MPa for the bovine and human tibiae, respectively; $p = 0.04$), and elastic modulus was different for different bovine anatomical sites (313 ± 182 MPa vs. 450 ± 50 MPa for the humerus and tibia, respectively; $p = 0.02$). No significant differences were observed between the two anatomical sites investigated in the human bone, although both elastic modulus and ultimate stress were approximately 25% higher, on average, in the tibia compared to the femur ($p = 0.13$ and $p = 0.27$, respectively). Significant differences were found in elastic modulus between bovine tibia compared to human femur (450 ± 50 MPa vs. 275 ± 94 MPa; $p = 0.003$), and ultimate stress between bovine tibia compared to human femur (25.5 ± 4.7 MPa vs. 14.7 ± 4.2 MPa; $p = 0.005$). No significant differences were observed between any groups for either ultimate strain or strain-to-failure or between human femur and human tibia for any mechanical property. Additionally, ultimate strain and strain-to-failure differed by less than 2% in all cases, so only strain-to-failure is reported.

Discussion

The findings of this study confirm that the mechanical properties of bone collagen are heterogeneous among different species and anatomical sites. Furthermore, this variation is not due to differences in the testing techniques since all the groups in this experiment were tested using identical methods. The elastic modulus and ultimate stress of bovine tibial bone collagen were 64% and 73% higher, respectively, than collagen from the human femur. Among the species and anatomical sites tested, the trends were that bovine bone collagen was stronger and generally more stiff than human bone collagen and that tibial bone collagen was stiffer and stronger than collagen from other bones from the same species, suggesting that a bovine model may not be appropriate for studying human bone collagen. The structure of engineering polymers including chain length and cross-link density are known to affect the mechanical properties of these materials (160). It is therefore reasonable to assume that similar parameters are the source of the heterogeneity of

the mechanical properties of bone collagen. Moreover, relating these structural differences to differences in the mechanical properties may enhance our understanding of the mechanical behavior of both healthy and diseased bone tissue.

A number of strengths support the validity of this study. The soft tissue extensometer used to calibrate the strain measurements was designed to minimize the transverse force and the deformation of the specimen compared to a clip-on style extensometer. While this method was different than that used by Bowman *et al*, both methods should provide accurate and precise results. Additionally the use of a computer controlled milling machine provided specimens of consistent geometry and uniform cross-section along the gage length. This, combined with the large aspect ratio of our specimens, ensured that there was a uniform stress state in the gage length. Finally, the use of bone collagen specimens from three anatomical sites and two species and from at least 31 human cadavers provides generality to our conclusions.

While this study indicates that elastic modulus and ultimate strength of isolated bone collagen do vary with species and anatomic site, a few limitations must be addressed. Most importantly, the load frame LVDT was used for strain measurements, so measured strains may have been lower than local strains around the site of failure. To assess this limitation, the load frame LVDT was calibrated with a soft-tissue extensometer. Stress-strain curves generated from LVDT strain data and soft-tissue extensometer data were coincident for all samples that remained in contact with the extensometer throughout the loading period. This indicated that our method of calibrating the LVDT using the soft-tissue extensometer was as accurate as the extensometer itself, but more reliable at large strains where the extensometer was prone to falling off the specimen. A second limitation was that not all specimens failed in the gage length. Comparison of the stress-strain curves from samples which failed in the gage length and in the fillet region showed no qualitative differences. Since this problem was random rather than specific to one or two of the test groups, its affect, if any, would be the same across all test groups and therefore would not alter the results that were

statistically significant. This limitation may have reduced the power of our statistical tests however, and therefore masked some differences which would have otherwise been significant such as the 25% difference in the average elastic modulus and ultimate stress of human tibia vs. human femur. Finally, the use of different anatomical sites in the human (tibia and femur) and bovine (tibia and humerus) bone prevented the use of a two-factor ANOVA for statistical analysis. Although this method would have been preferable in order to separate the effects of species and anatomical site, the one-factor ANOVA did indicate significant differences among species (bovine tibia vs. human femur) and anatomical site (bovine tibia vs. bovine humerus).

Our results indicate that there is variation in the mechanical properties of bone collagen among species and anatomical site. The mechanical properties measured here fall in the range of those reported previously (Table 4.1). Specifically, The average strain-to-failure in all groups in this experiment was higher than values reported previously for human femur (74) and bovine tibia (156) and lower than values reported previously for bovine femur (159) and bovine humerus (158). Ultimate stress values are similar to those reported previously for human bone (15 MPa and 18 MPa for human femur and tibia in this study compared to 17 MPa reported previously for human femur (74)) but range from 25% to 75% lower than those reported previously for bovine bone. The average elastic modulus of bovine tibia and humerus were 18% higher and lower, respectively, than the elastic modulus that Wright *et al.* measured for the bovine femur. The elastic modulus of human femur and tibia were about one-third and two-thirds higher than the same tissues tested previously, although harsh demineralizing agents were used, particularly with the human tibia, and this may have compromised the tissue. We were unable to reproduce the large average values of modulus, strength and ultimate strain seen by Bowman *et al.* (158) and Burstein *et al.* (156) for bovine humeral collagen, although some bovine humerus specimens in this study had modulus and strength values as high as 625 MPa and 45 MPa, respectively. While the high modulus and strength values reported in the latter study (156)

may have been caused by the high strain rate (~12%/second) used, Bowman *et al.* used a much lower rate (~0.5%/second) and obtained similar results. Thus, discrepancies between this and previous experiments are most likely due to heterogeneity of bone collagen and not testing technique. Relating these differences in mechanical properties to structural differences of bone collagen may enhance our understanding of the mechanical behavior of both healthy and diseased bone tissue.

The results of this experiment have implications for future research in bone mechanics. Specifically, the differences observed in bovine and human bone collagen in this and previous experiments indicate that using a bovine model may not be appropriate for studying human bone mechanics. Since collagen is thought to play an important role in the post-yield behavior of bone, the large differences in strain-to-failure reported here and by Bowman *et al.* suggest that we must be especially cautious of using a bovine model for investigating properties like strain-to-failure or toughness. Additionally, if age or disease related affects are being investigated, the bovine model must be verified since collagen is thought to play an important role in these processes. Site-specific differences in strain-to-failure have also been reported for intact human bone (10), thus it seems likely that differences in the mechanical properties of bone collagen are reflected in the intact bone. If this is the case, then there is a clear need for understanding the role of age and disease on the mechanical properties of bone collagen, as it may improve our ability to treat these conditions.

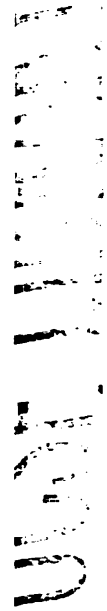

Table 4.1. Review of the monotonic tensile mechanical properties of demineralized bone collagen.

Source	Treat-ment	Species, site	# specimens/ # bones	Strain rate (%/sec)	Elastic modulus (MPa)	Ultimate stress (MPa)	Strain-to-failure (%)
Mack (1964)	HNO	Human tibia	5/5	~ 0.3†	212 ± 19†	7.0 ± 2.0†	—
Sweeney *et al.* (1965)	dilute HCl	Human femur	10/1?	—	209 ± 75†	17 ± 4.1†	6.7† ± 1.0†
Burstein *et al.* (1975)	0.5 M HCl	Bovine tibia	4/1	~ 12	750 ± 212	40 ± 3.0	6.1 ± 1.7
Wright *et al.* (1981)	0.2 M HCl	Bovine femur	11/1	~ 2.5	370 ± 50	34 ± 7.5	9.2 ± 1.5
Bowman *et al.* (1996)	0.5 M EDTA	Bovine humerus	18/6	~ 0.5	613 ± 113	62 ± 13.1	12.3 ± 0.5
Present study	0.5 M EDTA	Bovine humerus	8/8	0.3	313 ± 182	21 ± 14.4	8.9 ± 1.2
		Bovine tibia	8/8	0.3	450 ± 50	26 ± 4.7	8.4 ± 1.2
		Human femur	10/10	0.3	275 ± 94	15 ± 4.2	8.7 ± 2.7
		Human tibia	13/13	0.3	351 ± 102	18 ± 4.8	7.8 ± 0.9

All values are mean ± SD.

— indicates that the property was not reported.

† Estimates from analysis of Bowman *et al.* (158) of published data and stress-strain curves.

Table 4.2. Mechanical properties of isolated bone collagen from different species and anatomical sites.

	Bovine humerus (n = 8†)	Bovine tibia (n = 8 †)	Human femur (n = 10 †)	Human tibia (n = 13 †)	p value‡
Elastic modulus (MPa)	313 ± 182 (151-625)	450 ± 50 (378-518)	275 ± 94 (171-475)	351 ± 102 (178-489)	0.02
Ultimate stress (MPa)	21.3 ± 14.4 (7.1-45.2)	25.5 ± 4.7 (12.2-33.5)	14.7 ± 4.2 (9.3-22.4)	18.2 ± 4.8 (8.0-25.2)	0.03
Strain-to-failure (%)	8.9 ± 1.2 (7.0-10.4)	8.4 ± 1.2 (6.1-9.6)	8.7 ± 2.7 (6.3-13.7)	7.8 ± 0.9 (6.4-8.9)	0.42

All values are mean ± SD (Range).

† In each group, only one sample was produced from each human donor, a maximum of two samples were produced from each cow.

‡ P value was calculated using a one-factor ANOVA among all four groups. Fisher's LSD post-hoc tests indicated that for elastic modulus: bovine tibia ≠ human femur ($p = 0.003$) and bovine tibia ≠ bovine humerus ($p = 0.02$) and for ultimate stress: bovine tibia ≠ human femur ($p = 0.005$) and bovine tibia ≠ human tibia ($p = 0.04$).

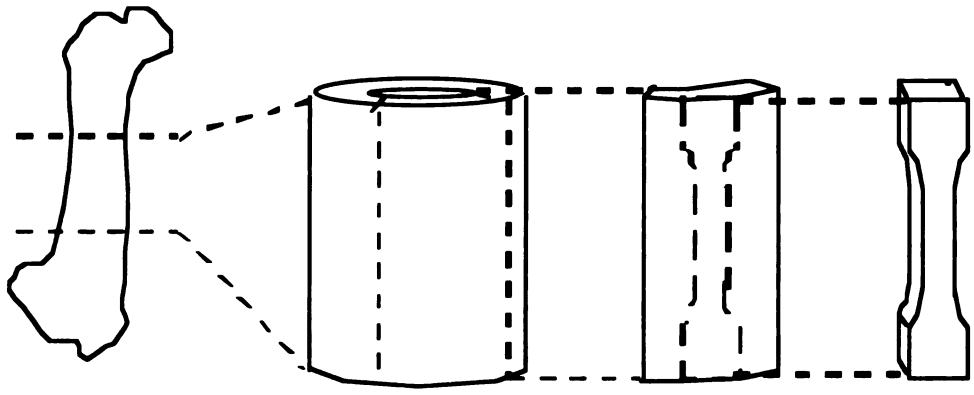

Figure 4.1. Schematic diagram of specimen harvesting protocol. One slab was cut from the diaphysis of each bone and then machined into a reduced-section geometry with a gage section of 1.8 x 3.0 x 18 mm.

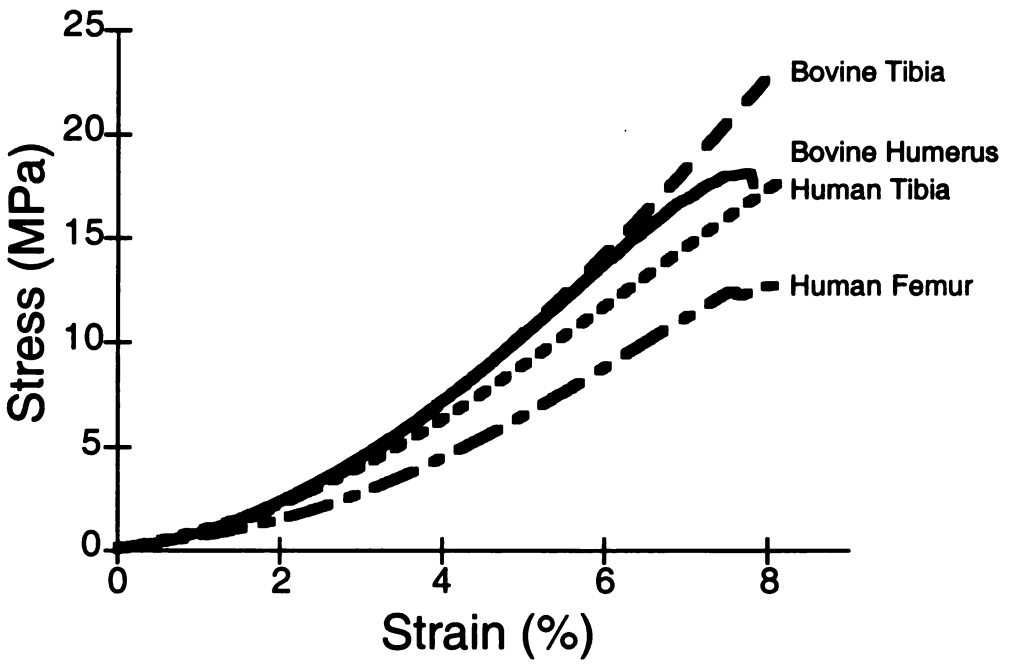

Figure 4.2. Typical tensile stress-strain curves of isolated human and bovine bone collagen.

Chapter Five. Cross-linking reduces the ductility of bone collagen

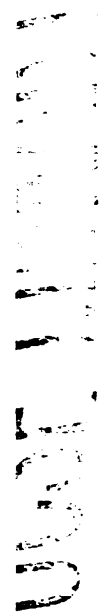

Introduction

Since bone is a composite material, variations in its mechanical properties should be reflected by variations in the amount and structure of its constituents. Understanding the mechanical properties of bone in relation to its constituents may aid in the design of drug therapies for osteoporosis and other bone diseases that can target the deficient constituent directly. Such treatments may be more effective than current treatments which aim to increase the amount of bone. Additionally, new, non-invasive assays of fracture risk and bone health that are based on biochemical assays of its constituents may be possible if we better understand how the mechanical properties of bone relate to the amount, structure, and biochemistry of its constituents.

Numerous studies of the variation in mechanical properties of bone have explained some of the variation, especially age-related, in terms of various aspects of the microstructure of the tissue (10, 17, 19, 161, 162). Changes in porosity, from about 5% at age 20 to 12% at age 80 in humans, explains most of the variation in strength, but only part of the variation in fracture energy (17, 19, 162). From a clinical perspective, fracture energy is important since it determines whether a bone breaks or deforms without fracturing under falling conditions and other severe loads. The non-elastic part of fracture energy depends on the strength and the strain-to-failure of the material, both of which depend on age (10, 19, 23). In a previous experiment, it was demonstrated that there are site and species differences in the mechanical properties of isolated bone collagen (Chapter 4). Based on these findings, it was suggested, as it has been previously (19, 156), that the variation in the amount of cross-linking in bone collagen is responsible for differences in the mechanical properties of bone collagen and, in turn, intact bone. This relationship, between the amount of collagen cross-linking and mechanical properties, has been demonstrated for articular cartilage (163). In bone collagen, the strain-to-failure and post-yield or plastic modulus are thought to be related to the strain-to-failure and elastic modulus of the underlying collagen, respectively (156). Indeed, the mechanical properties of many

engineering and some biological polymers are affected by the amount of cross-linking (160, 163), but this has never been investigated in bone.

Cross-links in bone collagen can be divided into two types: enzymatic and nonenzymatic. The amount of enzymatic cross-links (hydroxlysine, lysylpyridinoline and hydroxylysylpyridinoline) does not change in bone collagen after skeletal maturity has been reached (20). Therefore, any age-related changes in the amount of cross-linking in bone collagen must be due to changes in the amount of nonenzymatic cross-links. Age-related changes in the level of pentosidine, the most abundant nonenzymatic cross-link, have not yet been examined in bone. From approximately age 20 to age 80 however, pentosidine levels increase by a factor of between four and six in both human articular cartilage (163, 164) and human dura mater (165). Furthermore, *in vitro* changes in pentosidine levels significantly altered the mechanical properties of human articular cartilage (163). Thus, if they exist, age-related changes in the pentosidine levels of bone collagen may also affect the mechanical properties of isolated bone collagen and intact bone.

The overall goal of the current experiment was to determine the effects of pentosidine cross-linking on the mechanical properties of isolated bone collagen. This is the second in a series of three experiments designed to relate the mechanical properties of bone to the microstructure of the constituents. The specific hypotheses for this experiment were that: a) the pentosidine level (*i.e.* cross-link density) in human bone collagen increases with age; b) the ultimate strain of isolated bone collagen decreases with increasing cross-link density; and c) the elastic modulus of isolated bone collagen increases with increasing cross-link density. To test these hypotheses we measured the pentosidine levels in isolated human cortical bone collagen from 14 cadavers aged 49 to 101 and compared the mechanical properties of untreated and cross-link enhanced collagen from the same individuals.

Methods

The level of pentosidine cross-linking in isolated bone collagen was measured using reversed-phase high performance liquid chromatography (RP-HPLC). Uniaxial tension tests were conducted to measure the elastic and failure properties of demineralized human femoral cortical bone with and without a cross-link enhancing ribose treatment. Right human femora (from eleven males and three females ranging in age from 49 to 101; mean ± SD of 69 ± 16 years) were obtained from national tissue banks.[1] Bones were excluded if there was any record of liver, kidney, or bone diseases, malignancy or cancer, vitamin D deficiency, drug use, Cushing's disease, or hypo- or hyper-thyroidism in the donor.

Specimen preparation was identical to that described previously (Chapter 4). Briefly, between six and twelve slabs were cut from the diaphysis of each bone on a band saw and machined on a computer controlled mill (1.8 x 3.0 x 18 mm gage section). Two specimens were randomly selected from each bone to allow paired statistical analysis between untreated vs. cross-link enhanced specimens. Specimens were demineralized by soaking in 0.5 M ethylenediamine tetraacetic acid for 4 days with fresh solution every day. Demineralization was verified by ashing small portions of the gage length of each sample after mechanical testing.

A ribose treatment was used to increase the amount of pentosidine cross-links and model age-related increases in pentosidine levels. This was necessary due to the old average age (69 years) of the cadavers used in this study. Ribose treatment has been successfully used to increase the collagen cross-link density in cartilage (163). One sample from each pair was randomly selected and assigned to the treatment group. Ribose treated samples were incubated at 30° C for 48 hours in 0.4 M ribose in phosphate buffered saline

[1] National Disease Research Interchange, Philadelphia, PA; University of California, Davis School of medicine, Davis, CA; Anatomical Gift Foundation, Phoeniz, AZ

(pH 7.4) containing 0.01% sodium azide in order to increase the number of pentosidine cross-links. The control group was treated in a similar solution without ribose. Following treatment, all samples were rinsed with phosphate buffered saline and reduced with sodiumborohydride (90 minutes at room temperature) to terminate the non-enzymatic glycation reaction. Reduction was then terminated by addition of acetic acid to pH 4.0. Finally, the samples were rinsed with phosphate buffered saline again.

All specimens were mechanically tested in uniaxial tension as described in Chapter 4. Specimens were loaded for nine pre-conditioning cycles from zero to approximately 3% strain and then loaded to failure, all at approximately 0.3%/second. Strain was measured with a soft-tissue extensometer[2] and the load frame LVDT using the effective gage length technique described previously (Chapter 4). Elastic modulus, ultimate stress and strain, and strain-to-failure were measured as described previously (Chapter 4). Since strain-to-failure was always coincident with or differed from the ultimate strain by less than 2%, only ultimate strain was reported. Mechanical properties were compared between cross-link enhanced treated vs. control groups using two-tailed paired Student's t-tests[3]. Paired analysis was selected since each pair of samples was machined from the same bone and only one pair was machined from each cadaver.

After mechanical testing, a small section was removed from the gage length of each sample for reversed-phase high performance liquid chromatography as described elsewhere (163, 166) in order to measure the level of pentosidine cross-links in both control and ribose treated samples. The analysis was performed in a 150 mm x 4.6 mm column;[4] the elution conditions were: time 17-30 min 0.05% (v/v) heptafluorobutyric acid in 40% (v/v) methanol. Fluorescence was monitored at 328/378 nm using a programmable fluorimeter.[5]

---

[2] Model 632.29c-30, MTS Corp., Eden Prarie, MN.
[3] Systat version 5.2, Systat, Inc., Evanston, IL.
[4] Micropak ODS-80TM, Varian, Inc., Palo Alto, CA.
[5] Model 821-FP, JASCO, Inc., Easton, MD.

The age-related variation in the number of pentosidine cross-links per mole of collagen molecules was determined using least-squares linear regression analysis.

Complete demineralization was confirmed by ashing a small portion of the gage length of each specimen at 700° C for 24 hours after mechanical testing. Demineralization was determined to be complete if there was no visible mineral in crucibles after ashing and the weight lost in each crucible was greater than 99% of the demineralized specimen weight. Seven specimens were excluded from the analyses because of incomplete demineralization (n=2) or because the demineralized specimen tore in the grip region (n=5). Since the statistical design for the comparison of mechanical properties required paired samples, a total of 14 specimens were excluded from this analysis, leaving seven specimens in each group. Four of the seven excluded specimens were in the control group, thus ten specimens (ranging in age from 49 to 84 years) were included in the linear regression of pentosidine level vs. age.

Results

Pentosidine cross-link density increased from 3.5 mmol/mol collagen near age 50 to 8.6 mmol/mol collagen for individuals over age 80 (Figure 5.1). The age-related increase was 1.3 mmol/mol collagen per decade of life ($r^2 = 0.55$; $p = 0.015$). Ribose treatment increased pentosidine density, on average, by a factor of two, from 6.2 mmol/mol collagen in untreated samples to 12.2 mmol/mol collagen ($p = 0.003$), thus mimicking approximately 45 years of aging.

All untreated specimens exhibited an initial non-linear toe region followed by a linear region extending to failure (Figure 5.2); cross-link enhanced specimens had qualitatively similar stress-strain curves (Figure 5.2). As expected, demineralized human bone became less ductile after the cross-link enhancing treatment (Table 5.1). The ultimate strain of the demineralized bone decreased 13% on average from $8.4 \pm 1.3\%$ strain to $7.3 \pm 1.5\%$ ($p = 0.038$) in ribose treated samples compared to untreated controls. There was no significant change in the elastic modulus of ribose treated samples compared to the

control samples but there was a suggestive trend; the average elastic modulus of demineralized bone decreased 17%, from 294 ± 103 MPa to 245 ± 82 MPa ($p = 0.149$) in ribose treated samples compared to untreated controls. Ultimate stress was affected similarly to ultimate strain, being reduced by an average of 19%, from 15.1 ± 5.1 MPa to 12.2 ± 3.0 MPa ($p = 0.103$).

Ultimate strain did not vary with either age or pentosidine level in the control group ($p = 0.33$, Appendix B; and $p = 0.55$, Appendix C, respectively), despite the highly significant difference found between controls and paired ribose treated samples. Regressions between modulus vs. age and pentosidine level and between ultimate stress vs. age and pentosidine level were significant at the $p = 0.05$ level (Appendices B and C).

Discussion

The results of this study indicate that pentosidine cross-link density increases with increasing age and that the mechanical properties of human bone collagen are significantly altered by changes in the pentosidine cross-link density. Furthermore, ribose treatment provided a good model of aging of bone collagen, as the treatment mimicked 45 years of aging. Since the ductility of bone is thought to be due to the collagen component (156, 167), these findings provide strong evidence that an increase in the pentosidine cross-link density of collagen will decrease the ductility of mineralized bone. This suggests that the bones of older individuals, which have a higher cross-link density compared to bones of younger individuals, are more likely to fracture under falling conditions compared to bones from younger individual with similar bone mass and structure.

In this experiment, specimens were harvested in a paired fashion, *i.e.* only two specimens were used from each bone. The use of paired samples increased the power of the comparisons relative to an unpaired test, enabling use of a small sample size to show significant differences between the ribose enhanced and untreated groups. Larger sample sizes may have indicated a significant difference in the elastic modulus, but significant differences were observed in other properties indicating that ribose treatment did have a

statistically significant effect on some of the mechanical properties of demineralized bone. Additionally, specimens were harvested from seven cadavers, indicating that the effects were not due to abnormalities in bone tissue from one or two donors.

Another limitation of the small samples sizes used in this experiment is that an *in vitro* cross-link enhancement was required in order to relate ductility to pentosidine level. Although linear regressions of the mechanical properties vs. pentosidine level of the untreated samples was used to correlate natural pentosidine levels and mechanical properties (Appendix C), a significant relationship was not observed between strain-to-failure and pentosidine level. However, linear regressions for elastic modulus and ultimate strength vs. pentosidine and age were significant. Power analysis revealed that 81 samples would be required to show a significant relationship between strain-to-failure and pentosidine level over the range tested here. This sample size could be reduced by increasing the age range (and thus pentosidine level range) of the cadavers used. Another disadvantage to using naturally occurring variations in pentosidine level is that other age-related factors may confound the results. The method used in this study employed paired samples and a treatment which mimicked aging in order to isolate the role of pentosidine on the ductility of bone from other confounding factors.

Another limitation of this study is that pentosidine cross-link density in young (below age 49) individuals was not measured. While this information is essential in mapping the pentosidine cross-link density though adult life, a significant age-related affect was observed. The 2.5-fold increase seen in approximately 30 years (from age 50 to age 80) is comparable to the four-to-five-fold increase seen in articular cartilage (163, 164) and dura mater (165) over 60 years (from age 20 to age 80) on a per decade basis. The similarities of the age-related changes in the pentosidine level among different tissues suggests that aging affects many collagenous tissues similarly via increased pentosidine cross-link density.

The results of this experiment have implications in both the research and clinical arenas. The role of pentosidine in the ductility of isolated bone collagen has been demonstrated, but this remains to be shown for intact bone. Furthermore, additional work is required to determine the levels of pentosidine in bone collagen in individuals younger than 49 years, and how these (presumably) lower levels of pentosidine affect ductility. Clinically, these results suggest that the ductility of bone may be increased, or at least maintained, by controlling the level of pentosidine cross-links in collagen.

Table 5.1. Tensile mechanical properties and pentosidine cross-link density of untreated and cross-link enhanced demineralized human femoral cortical bone specimens (paired samples; n = 7 per group).

	Control (Untreated)	Cross-link Enhanced	Average % Change †	p value ‡
Pentosidine cross-links (mmol/mol collagen)	6.2 ± 2.7 (3.0-9.5)	12.2 ± 4.1 (7.0-17.3)	+97	0.003
Elastic Modulus (MPa)	294 ± 104 (184-475)	245 ± 82 (169-396)	-17	0.149
Ultimate Stress (MPa)	15.1 ± 5.1 (8.7-22.4)	12.2 ± 3.0 (7.6-16.9)	-19	0.103
Strain-to-failure (%)	8.4 ± 1.3 (6.4-10.1)	7.3 ± 1.5 (5.1-9.2)	-13	0.020

All values are mean ± SD (range).

† Average % change is for cross-link enhanced compared to the untreated controls.

‡ p values were calculated using a paired sample Student's t-test.

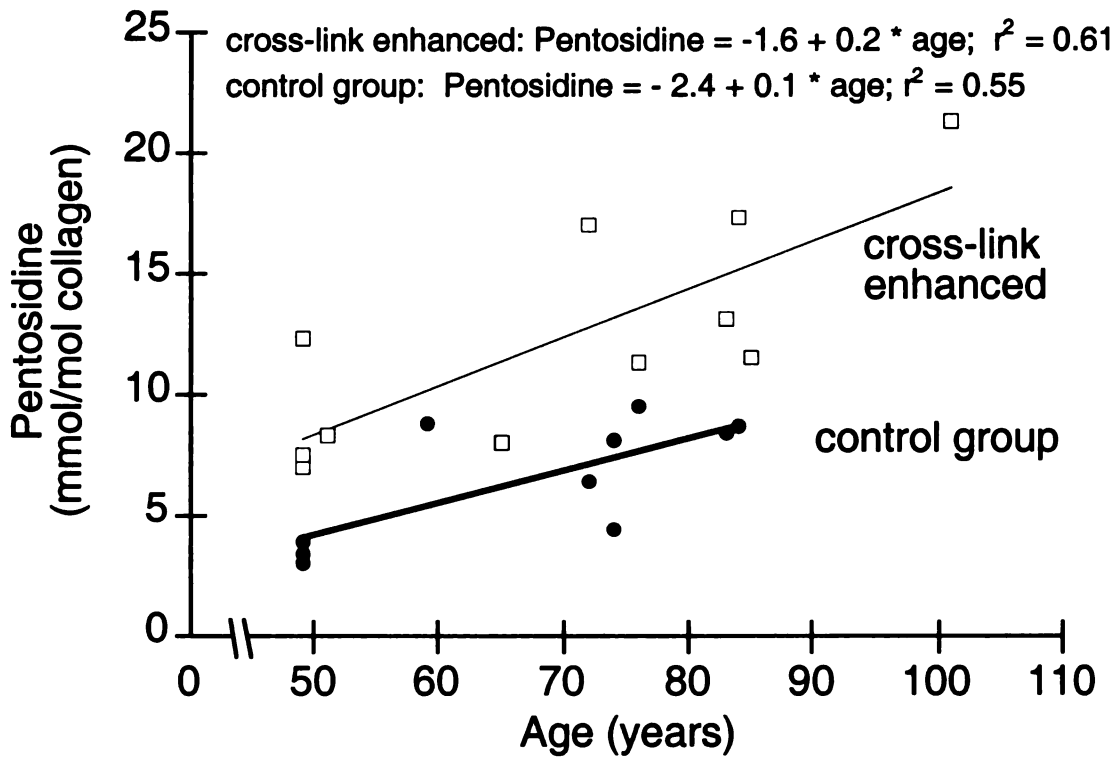

Figure 5.1. Pentosidine cross-link density of untreated and cross-link enhanced demineralized human femoral cortical bone. Ribose treatment increased cross-link density by a factor of two, on average. This increase is similar to that seen in untreated bone between age 50 to age 85. The best-fit lines were determined using least squares linear regressions; both regressions were statistically significant ($p = 0.015$ for control group and $p = 0.005$ for cross-link enhanced).

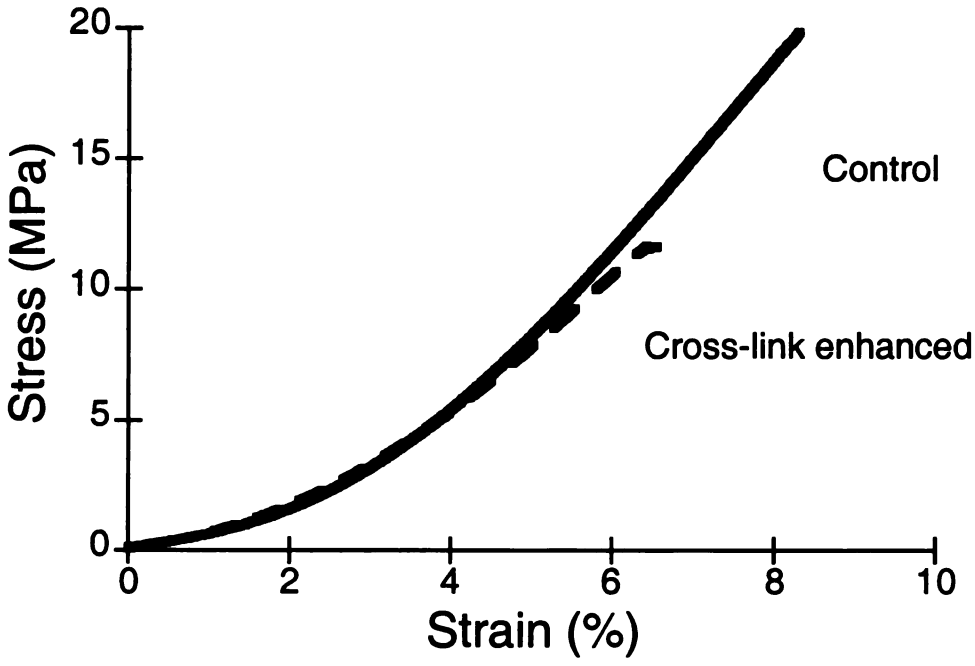

Figure 5.2. Typical tensile stress-strain curves of untreated and cross-link enhanced demineralized human femoral cortical bone. Only strain-to-failure was significantly different between the two groups (paired t-test: $p = 0.020$).

Chapter Six. Collagen cross-linking reduces the ductility of bone

Introduction

A reduction in the ductility of bone is an important consequence of aging and disease. Bone tissue with low ductility is less capable of absorbing energy from falls and other severe loads and thus is more prone to fracture compared to younger, more ductile bone. For example, the prevalence of vertebral fractures is more than 55% in women over 90 years old, but only 6% in women aged 50-54 years (168). Since bone is a composite material, variations in its mechanical properties should be reflected by variations in the amount and structure of its constituents. Understanding this relationship may improve our ability to design drugs that can target deficient constituents directly and have a complementary effect to current treatments which aim to increase bone mass. Additionally, new, non-invasive diagnostic assays of fracture risk and bone health may be possible if we better understand how the mechanical properties of bone relate to the structure of the constituents.

From a biomechanical perspective, the ductility of bone is important since it determines whether a bone breaks or deforms without fracturing under severe loads. In previous experiments, it has been shown that the amount of pentosidine cross-linking increases with age in isolated human bone collagen and that this increase reduces the ductility of the collagen (Chapter 5). Based on these findings, we suggested, as have others (19), that age-related increases in the amount of cross-linking in bone collagen is responsible for differences in the ductility of bone. This relationship, between cross-link density and mechanical properties, has been demonstrated in other collagenous tissues (163, 169) but not in intact bone. For example, ultimate strain decreased while the relative amount of insoluble (or highly cross-linked) collagen increased with age in the skin, tendon and aorta, of 2-year-old rats compared to 4-month and 1-year-old controls (169), and instantaneous deformation, which is inversely related to material stiffness, was reduced in human articular cartilage by increasing the level of pentosidine cross-linking (163). Since

bone is more than 25% collagen (by volume) it is likely that this relationship, between cross-link density and ductility also exists for bone tissue.

The overall goal of the current experiment was to describe the age-related changes in pentosidine cross-link levels in human cortical bone and determine the effect of these cross-links on its ductility. This was the final experiment in a series of three designed to relate the mechanical properties of bone to the microstructure of its constituents. The specific hypotheses for this experiment were that: a) pentosidine levels in human bone increase with age, and b) ductility of bone decreases with increasing pentosidine cross-link density. To test these hypotheses we measured pentosidine levels in femoral cortical bone from 16 cadavers aged 49 to 101 years and compared the mechanical properties of untreated and cross-link enhanced bone from the same individuals.

Methods

The level of pentosidine cross-linking in human femoral bone was measured using reversed-phase high performance liquid chromatography. Tension tests were conducted to measure the elastic and failure properties of human femoral cortical bone with and without a cross-link enhancing ribose treatment. Right human femora (from 13 males and three females ranging in age from 49 to 101 years; mean $\pm$ SD of 72 ± 15 years) were obtained from national tissue banks[1]. Bones were excluded if there was any record of liver, kidney, or bone diseases, malignancy or cancer, vitamin D deficiency, drug use, Cushing's disease, or hypo- or hyper-thyroidism in the donor. Specimen preparation was identical to that described previously (Chapters 4 and 5). Two samples were obtained from each bone to allow paired statistical analysis.

[1] National Disease Research Interchange, Philadelphia, PA; University of California, Davis School of medicine, Davis, CA; Anatomical Gift Foundation, Phoeniz, AZ

A ribose treatment was used to increase the amount of pentosidine cross-links in cortical bone. This treatment has been successfully used to increase the collagen cross-link density in human articular cartilage (163) and in isolated bone collagen (Chapter 5). One sample from each pair was randomly selected and assigned to the treatment group. Ribose treated samples were incubated at 30°C for ten days in 0.4 M ribose in phosphate buffered saline (pH 7.4) containing 0.01% sodium azide. The control group was treated in a similar solution without ribose. Following treatment, all samples were rinsed with phosphate buffered saline and reduced with sodiumborohydride to terminate the non-enzymatic glycation reaction. Reduction was then terminated by addition of acetic acid to pH 4.0. Finally, samples were rinsed with phosphate buffered saline again.

All specimens were tested in uniaxial tension on a servo-hydraulic load frame[2] in displacement control, corresponding to an approximate strain rate of 0.1%/second. Specimens were attached to the load frame actuator using a two-jaw self-centering chuck with a recess machined into the grip faces to ensure axial alignment of the specimen. The specimen was attached to the fixed part of the load frame with a custom grip fixture designed to eliminate bending in the sample. The grip consisted of a small aluminum cylinder with a dovetail shaped channel cut at the top. To attach the specimens into the custom grip the open ends of the channel were covered with adhesive tape and then the channel was filled with uncured polymethylmethacrylate cement. The specimen was then lowered into the cement and left in place for approximately 15 minutes in order for the cement to cure before mechanical testing. The gage length of each specimen was wrapped in saline soaked gauze during the entire mounting and curing process, which lasted approximately 20 minutes. Load was measured with a 1,112 N load cell. Strain was measured with a 5 mm gage length miniature extensometer[3] attached to the middle of the specimen gage length using spring clips.

---

[2] Mini-bionix 858 MTS Corp., Eden Prarie, MN.
[3] Model 632.29f-30, MTS Corp., Eden Prarie, MN.

Elastic modulus was measured as the maximum slope, measured with a least-squares linear regression over a 0.15% strain range, in the linear region of the stress-strain curve. The yield point was defined as the intersection of the 95% secant line and the stress-strain curve. The 95% secant line is created by plotting a line through the origin with a slope equal to 95% of the elastic modulus of the specimen. The post-yield modulus was defined as the average slope of the stress-strain curve after the knee in the stress strain curve. The ultimate point was defined at the point of maximum stress. The strain-to-failure was defined as the strain at the point where the specimen could no longer bear any load. In all cases the ultimate strain and strain-to-failure were either coincident or differed by less than 2% and thus only strain-to-failure is reported. The post-yield strain was defined as the strain-to-failure minus the yield strain. All mechanical properties were compared between groups using paired Student's t-tests[4].

After mechanical testing, a small section was removed from the gage length of each sample for reversed-phase high performance liquid chromatography as described elsewhere (163, 166) in order to measure the level of pentosidine cross-links in both control and ribose treated samples. The analysis was performed in a 150 mm x 4.6 mm column;[5] the elution conditions were: time 17-30 min 0.05% (v/v) heptafluorobutyric acid in 40% (v/v) methanol. Fluorescence was monitored at 328/378 nm using a programmable fluorimeter.[6] The age-related variation in the number of pentosidine cross-links per mole of collagen molecules was determined using least-squares linear regression analysis.

Complete demineralization was confirmed by ashing a small portion of the gage length of each specimen at 700° C for 24 hours after mechanical testing. Demineralization was determined to be complete if there was no visible mineral in the crucibles after ashing and the weight lost in each crucible was greater than 99% of the demineralized specimen weight. Two specimens were not completely demineralized and thus excluded from the

[4] Systat version 5.2, Systat, Inc., Evanston, IL.
[5] Micropak ODS-80TM, Varian, Inc., Palo Alto, CA.

analysis. An additional three specimens were excluded from the analyses because of the polymethylmethacrylate grip failed during the test. Since the statistical design for the comparison of mechanical properties between treated and untreated samples required paired samples, a total of eight[7] specimens were excluded from this analysis, leaving nine specimens in each group. Four of the five excluded specimens were in the control group, thus 12 specimens (ranging in age from 49 to 85 years) were included in the linear regression of pentosidine level vs. age.

Results

The amount of pentosidine cross-linking in human cortical bone increased by approximately 65%, from an average of 4.3 mmol/mol collagen in the three youngest cadavers investigated (aged 49, 49 and 51 years) to an average of 7.1 mmol/mol collagen in the three oldest individuals (aged 83, 84 and 85 years). Linear regression analysis revealed that pentosidine levels increased nearly 1 mmol/mol collagen per decade of life in the untreated samples ($r^2 = 0.53$; $p = 0.008$; Figure 6.1). The ribose treatment increased pentosidine cross-linking five-fold, on average (31 ± 7 mmol/mol collagen for ribose treated vs. 6 ± 2 mmol/mol collagen for untreated controls; $p < 0.0001$; Table 6.1). The linear regression between pentosidine level and age predicts a similar five-fold increase in pentosidine level from age 20 to age 80, when extrapolated back to the younger age. Thus the ribose treatment mimicked approximately 60 years of aging. Pentosidine cross-linking was not related to age in the cross-link enhanced group (Figure 6.1), and thus the relative increase between untreated controls and treated samples was greater in specimens from younger individuals compared to older ones.

The five-fold increase in pentosidine cross-link density was reflected by reduced ductility of bone. Strain-to-failure, a measure of the total deformation of a specimen,

---

[6] Model 821-FP, JASCO, Inc., Easton, MD.

[7] Eight, rather than ten specimens were excluded in total since two of the excluded specimens were from a matched pair, *i.e.* the same donor.

decreased 28%, on average, in the cross-link enhanced group compared to untreated controls ($1.63 \pm 0.54\%$ vs. $1.18 \pm 0.63\%$; $p = 0.026$; Table 6.1). Ultimate strain is not reported since strain-to-failure and ultimate strain differed by less than 2% for all specimens. Post-yield strain, a more refined measure of ductility, decreased 38%, on average, in cross-link enhanced specimens compared to untreated controls ($1.23 \pm 0.54\%$ vs. $0.76 \pm 0.60\%$; $p = 0.015$; Table 6.1).

All intact specimens exhibited an initial linear region followed by yield region and then a second linear region with a much lower slope than the first (Figure 6.2). All cross-link enhanced had similar linear and yield regions but only five out of nine displayed a second linear region (Figure 6.2). The other four samples failed after the initial linear region. Qualitative differences in the behavior of cross-link enhanced specimens could not be explained by age or gender differences. All specimens failed in the gage length.

Mechanical properties besides ductility were not significantly altered by increases in the collagen cross-link density (Table 6.1). Elastic modulus, yields stress and strain, and post-yield modulus were not different in cross-link enhanced samples compared to untreated controls ($p > 0.65$ for these properties; Table 6.1). Ultimate stress tended to reduce by 6% on average; this result was not significant ($p = 0.082$) and was due to the loss of post-yield strength since yield strengths in both groups were equal (66.8 ± 7.7 vs. 67.0 ± 11.0; $p = 0.97$; Table 6.1).

Discussion

The results of this study demonstrate that pentosidine levels in human cortical bone increase with age and furthermore, that the ductility of human cortical bone is substantially reduced by increases in the amount of pentosidine cross-links. The reduction in ductility with increased pentosidine level parallels that seen in isolated bone collagen (Chapter 5). No other mechanical properties of cortical bone were significantly affected by our cross-link enhancing treatment. In a previous study, it was demonstrated that the elastic modulus was not altered by removing 85% of the organic material but the strength was reduced by

35% in compression and 95% in tension (Chapter 3). Combined, these results, suggest that the role of collagen in the mechanical properties of bone is twofold: First, collagen is responsible for the ductility of bone, if the ductility of the collagen is reduced, by increasing the cross-link density, for example, bone ductility will also be compromised. Second, collagen toughens the hydroxyapatite, allowing it to attain higher strengths than it is capable of alone. Thus, the role of collagen is more important in tensile loading since: 1) intact bone is not ductile in compression (Chapter 3) so increasing collagen cross-links will probably have no further affect on ductility; and 2) isolated hydroxyapatite maintains 63% of the strength of intact bone in compression but only 9% in tension (Chapter 3).

The statistical design and testing technique support the validity of this study. The custom designed grip fixture eliminated bending in the samples. This is important since bending can lead to errors in the strain measurements as large as 20% when using traditional gripping techniques. The use of paired samples increased the power of the comparisons relative to an unpaired test, justifying the use of relatively small sample sizes. Additionally the use of a computer controlled milling machine provided specimens of consistent geometry and uniform cross-section along the specimen's gage length. This, combined with the large aspect ratio of the specimens, ensured that there was a uniform stress state in the gage length. Finally, the use of bone specimens from nine different donors provides a degree of generality to the conclusions.

While this study indicates that the ductility of cortical bone is reduced by increases in the pentosidine cross-link density, a few limitations must be addressed. First, the cross-link density in the samples used in this experiment was artificially increased by a factor of five and thus is higher than physiological levels. Although the *in vitro* increase in pentosidine level was higher than that observed physiologically in an absolute sense, the relative increase is similar to what might be expected *in vivo*. Using the linear regression between pentosidine level and age to estimate the average level in a 20 year old population predicts approximately 1.5 mmol/mol collagen. This is nearly five times less than the levels

observed in the three oldest individuals in this experiment (7.1 mmol/mol collagen; average age 84 years), thus the five-fold increase is appropriate in order to demonstrate the effect of increasing pentosidine levels over a larger age range. Now that this relationship has been demonstrated, more extensive studies on age-related changed are justified. Specifically, the level of pentosidine cross-linking in young individuals must be investigated.

A second limitation is that the number of specimens included in the statistical analysis was small, but significant differences in ductility were observed nonetheless. Even though larger samples sizes may have indicated significant differences in the ultimate stress, this difference is small (6%) and probably not important compared to the 28% reduction in strain-to-failure and the 38% reduction in post-yield strain. Third, although all specimens failed within the gage length not all specimens failed between the extensometer knife edges. However, comparison of the stress-strain curves from samples which did and did not fail between the knife edges showed no qualitative differences. Since this problem was random rather than specific to one of the test groups, its affect, if any, would be the same for both test groups and therefore not affect the statistical comparisons.

Linear regression analysis of pentosidine level vs. age suggests that there is a five-fold increase in pentosidine level between the ages of 20 and 85 years. This agrees well with the increases observed in isolated bone collagen (Chapter 5), human articular cartilage (163, 164), and human dura mater (165) on a per decade basis. Pentosidine levels were also increased by a factor of five in the treatment group of this study, which suggests that the change in ductility that we observed, is similar to what can be expected through adult life.

These results demonstrate that increasing the collagen cross-link density reduces the ductility of bone. Changes in collagen cross-linking may therefore explain age-related changes in the mechanical properties of bone. For example, other authors have measured a 5.1% (23) and 9% (19) drop in ultimate strain per decade of life in fresh human femora and a 6.8% per decade drop for fresh human tibia (23), so our cross-link enhancing treatment

corresponds to between 30 and 55 years of aging. The mechanical properties measured in this experiment agree very well with data from the 60-80 year-old population in the latter study (19) although the age-related changes observed previously (19, 23) were not seen here in the untreated control group, due to the relatively low sample size (Appendix B). Additionally, ultimate strain was 26% lower in embalmed cortical bone from older (average age 71 years) compared to younger (average age 42 years) men (10). This is very close to the 28% reduction we observed with a fivefold increased in pentosidine cross-link density for nine individuals (average age 72 years).While the bone used in that experiment was fixed, a recent study has demonstrated that strain-to-failure is not affected by fixation (170) thus similar age-related differences can be expected in fresh (*i.e.* not fixed) bone.

The results of this study have substantial clinical implications. Most importantly, the reduction in bone ductility that occurred with an increase in collagen cross-link density suggests that decreasing bone collagen cross-link density may reduce the risk of fracture. It is reasonable to assume that the reduction in ductility observed for human cortical bone will also occur in human trabecular bone if the pentosidine cross-link density is increased. If this is true, then the ductility of whole bones will be compromised. That is, increased cross-linking will make bones less tough (without necessarily losing any strength) and therefore less able to absorb energy during falls or other severe loading configurations. Thus drugs which can reduce or prevent age-related increases in the amount of pentosidine cross-linking in bone are potential complements or alternatives for current therapies which target osteoporosis and other bone diseases. Collagen is present in many tissues including skin, cartilage, tendon and ligament however, and it is unclear what other effects reducing collagen cross-link density might have on these tissues. Thus, further investigation into the role of cross-linking in other collagenous tissues is required before any specific drug treatments can be suggested. In addition to new drug therapies, the current results suggest possible methods to assay fracture risk. Specifically, biochemical assays of the pentosidine

Table 6.1. Mechanical properties of untreated and cross-link enhanced human femoral cortical bone (paired samples; n = 9 per group).

	Control (Untreated)	Cross-link Enhanced	Average % Change ††	p value ‡
Pentosidine cross-links (mmol/mol collagen)	6 ± 2 (4-9)	31 ± 7 (23-42)	509	< 0.001
Elastic Modulus (GPa)	17.7 ± 1.5 (14.6-19.4)	17.4 ± 2.0 (13.3-20.6)	-2	0.65
Yield Stress (MPa)	66.8 ± 7.7 (49.8-75.8)	67.0 ± 11.0 (44.3-77.4)	0	0.97
Yield Strain (%)	0.41 ± 0.03 (0.35-0.44)	0.42 ± 0.06 (0.28-0.47)	+2	0.69
Post-yield Modulus † (MPa)	714 ± 207 (429-993)	735 ± 320 (429-1183)	+3	0.82
Ultimate Stress (MPa)	95.0 ± 5.6 (86.0-102.9)	89.3 ± 12.4 (67.2-109.4)	-6	0.082
Strain-to-failure (%)	1.63 ± 0.54 (0.96-2.5)	1.18 ± 0.63 (0.52-2.4)	-28	0.026
Post-Yield Strain (%)	1.23 ± 0.54 (0.56-2.2)	0.76 ± 0.60 (0.17-2.0)	-38	0.015

All values are mean ± SD (range).

† For post-yield modulus comparison n = 5 per group since four cross-link enhanced specimens did not display any post-yield region in their stress-strain curves.

†† Average % change is for cross-link enhanced compared to untreated.

‡ p values were calculates using a paired Student's t-test.

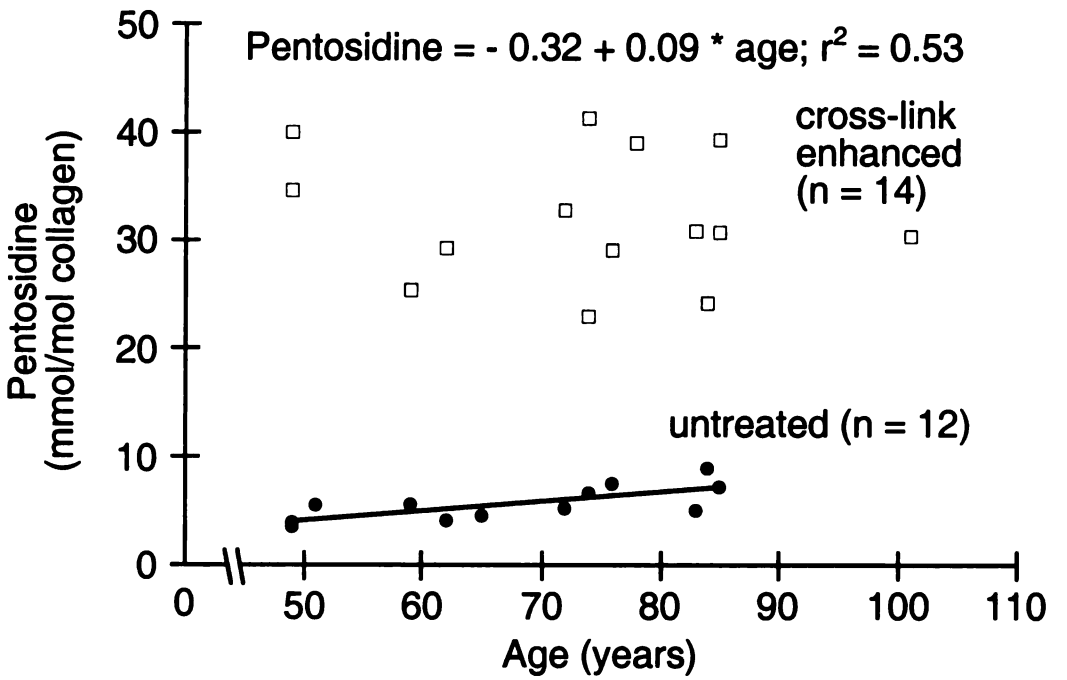

Figure 6.1. Pentosidine cross-link density of untreated and cross-link enhanced human femoral cortical bone. Ribose treatment increased cross-link density by a factor of five, on average. The regression equation was statistically significant ($p = 0.008$) for the control group but not for the cross-link enhanced group ($p = 0.59$).

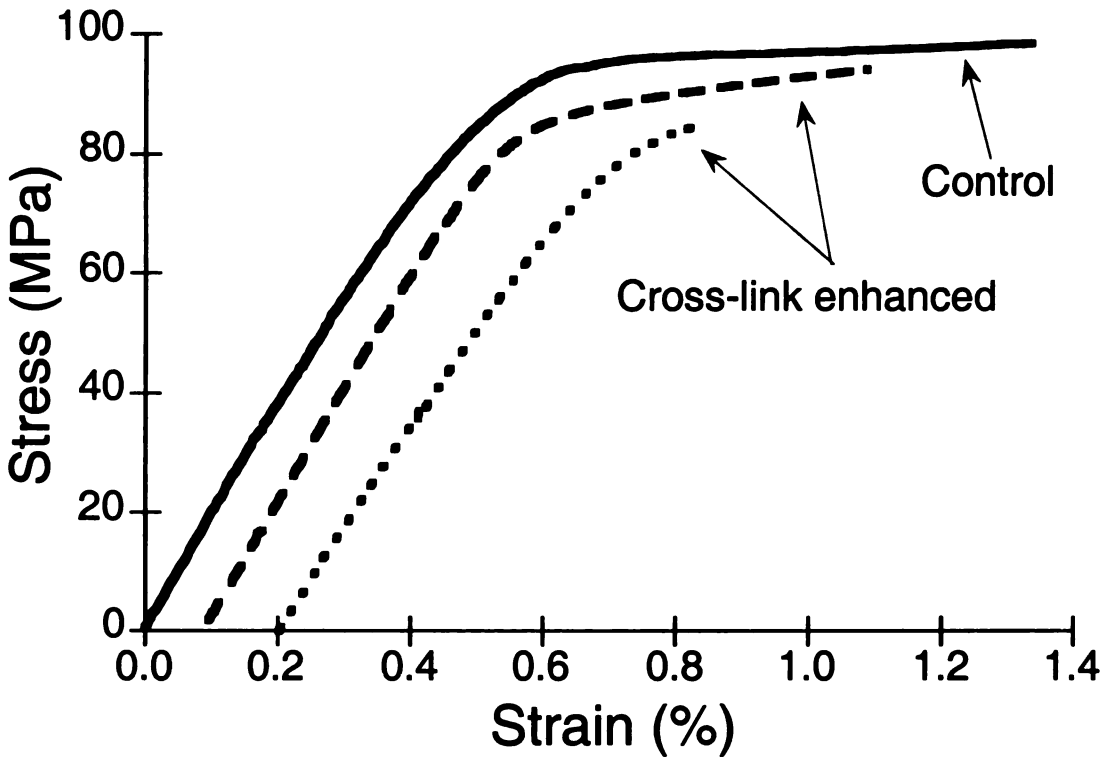

Figure 6.2. Typical tensile stress-strain curves of untreated and cross-link enhanced human cortical bone. Two typical stress-strain curves are shown for cross-link enhanced bone. Four out of nine cross-link enhanced samples failed without any post-yield region, the other five were qualitatively similar to the untreated controls but failed at lower strains. Differences in qualitative behavior of cross-link enhanced specimens could not be explained by age or gender differences. Ultimate strain was significantly lower in the cross-link enhanced group compared to the untreated control group (paired t-test: $p = 0.026$). Curves are offset from the origin along the strain axis for clarity.

Chapter Seven. A microstructure-based continuum damage model for cortical bone

Introduction

There are two specific motivations for creating models of bone: first, models can be used to predict the mechanical properties of bone in situations which are difficult or impossible to create or control experimentally. For example, microstructural parameters such as porosity and osteon size can be more thoroughly investigated with a model compared to an experimental approach since they can be varied independently in a model. A second motivation for creating models of bone is to solve inverse problems. In this case, the objective is to determine the mechanical properties of microstructural components, like osteons, using a model which incorporates the microstructure and accurately predicts the mechanical response of bone at a higher hierarchical level. More specifically, an estimate of the mechanical properties of osteons, which are input parameters in the model, can be made by adjusting the input parameters until the output—the mechanical properties of bone—match experimentally observed values.

A better understanding of the relationship between the microstructure and the mechanical properties of bone may lead to drugs which are targeted directly at the deficient constituent. This approach—improving the quality of the existing bone—would complement current drug treatments which attempt to increase whole bone strength by increasing or maintaining bone mass. Additionally, this information may help to develop drugs which can prevent degenerative changes before they occur. Fracture risk prediction may also be improved with such a model by the possible discovery of important biochemical markers of the microstructure and thus the mechanical properties of bone.

Previous models of cortical bone can be divided into two broad groups: elastic models and post-yield models. Models in the first group were based on theories proposed by Voight, Reuss, and Hashin and Shtrikman (171) and provided broad limits for elastic modulus when applied to bone (167, 172-175). Unfortunately, the wide bounds did not offer much physical insight into the micromechanics of bone. More recent models of the

elastic behavior have employed homogenization theory and finite element models to predict the elastic properties of cortical bone with more accuracy but have not addressed the post-yield response (176-178). The second group of models aims to describe either the complete stress-strain response of cortical bone or use the experimentally determined stress-strain response in order to model and predict damage in the tissue. Within this group, some authors have included the time-dependent response in their models. The simplest time-dependent model, a visco-plastic rheological model (179), displayed the elastic-strain hardening response seen for cortical bone in tension, but there was no microstructural basis for the individual elements of the model. Later models described the mechanical response of the tissue accurately, but did not incorporate bone anatomy explicitly (158) (156, 180). Fondrk (180) presented a strong argument that both the observed mechanical behavior and his theoretical model could be explained by an array of parallel penny shaped cracks in the tissue, but there has been no experimental work to confirm this. Although the cracks do provide a physical basis for Fondrk's continuum damage model, the origin and size scale of the cracks was not specified.

Two authors have developed continuum damage models which are rooted in a physical phenomenon: osteons debonding from the interstitial matrix (181, 182). Courtney, like Fondrk, developed a model to predict the amount of mechanical damage (quantified by modulus reduction upon reloading) induced by loading to various strain levels. The monotonic stress-strain response of bone was not modeled in either case. This leaves only one model which is rooted in a physical damage phenomenon and attempts to model the stress-strain response of cortical bone (182). Unfortunately, the Krajcinovic model is not accurate; it predicts damage from the onset of loading and thus lacks the initial linear region observed experimentally. Another discrepancy between the constitutive response predicted by the model and that observed experimentally is lack of a linear strain-hardening post-yield region. This is due to the limiting nature of the elastic constitutive response assigned to the

osteons in the model, whereas it is known that osteons exhibit inelastic behavior before failure (121).

One use of mechanical models of bone is the explanation of experimental results in terms of microstructure. The relationship between cortical bone mechanical properties and microstructural parameters such as porosity, mineral fraction and osteonal bone fraction, has been investigated empirically (13, 16-19), but little work has been done in comparing the relative effects of these microstructural parameters on the mechanical properties of bone. Stepwise multiple regression was used to rank microstructural properties in terms of their effect on bending properties (13), but the amount of osteonal vs. interstitial bone was not included in the analysis. Furthermore, these data, relating microstructure and mechanical properties have never been incorporated into a mathematical model of the elastic and post-yield properties of cortical bone. Such a model would be useful in that it could be used to predict the mechanical properties of bone after controlled variation of microstructural parameters that are difficult to control or measure experimentally. These predictions would then provide an understanding of the underlying failure mechanisms.

The overall goal of the current study was to expand the continuum damage model first proposed by Krajcinovic (182) in order to better understand the role of microstructure in the mechanical properties of bone. This approach could then be extended to the ultrastructural level to model collagen, hydroxyapatite , and their interface, in order to gain a more complete understanding of the structure-function relationship of bone tissue. The specific objectives of this study were to: 1) extend the Krajcinovic model to include in initial linear-elastic region and post-yield deformation; 2) further extend the model to include interstitial bone and incorporate variations in microstructure and mechanical properties; 3) perform a sensitivity analysis to determine the effect of input parameters on the predicted stress-strain response; 4) calibrate the model by comparing select model predictions to experimental results; 5) perform a parametric analysis to determine the role of porosity, osteonal bone fraction, and osteon and Haversian canal size on the mechanical

properties of bone; and 6) compare results from the parametric analysis to experimental results in order to provide an overall validation of the model. To meet these objectives, models of osteons embedded in a matrix of interstitial bone were created where both the osteons and the sections of interstitial bone were assigned mechanical properties from a statistical distribution. The models were numerically loaded in tension to failure and mechanical properties including elastic modulus and yield and ultimate stress and strain were calculated and compared with experimental results.

Theoretical Background

Three different models will be described in this section. First, the model proposed by Krajcinovic (182) will be reformulated in terms of the displacement which causes failure in each osteon, rather than force which Krajcinovic used. Second, the model will expanded to address one limitation of the original model, the lack of an initial linear region (Figure 7.1 and 7.2). Third, the model will be further expanded to address a second limitation of the original model, the lack of a linear, strain-hardening post-yield region (Figure 7.1 and 7.2).

The original model consisted of osteons only, that is, interstitial bone was not accounted for even though the failure mechanism was osteons pulling out of interstitial bone. The interstitial bone will be neglected here also. The model described in the next section will address this limitation.

The input parameters for these models are elastic modulus, initial and final yield strains and failure strain of the osteons.[1] These values, set to 17.7 GPa, 0.3%, 0.8% and 1.5%, respectively in each model were obtained from experimental results of larger,

[1]The following terminology will be used in this chapter for clarity: "Apparent" mechanical properties will be used to describe the mechanical properties of a continuum level specimen, *i.e.* a specimen that contains many osteons and many fragments of interstitial bone. The apparent properties may refer to either experimental results or the output of one of the theoretical models; it will be clear in the text which one is being refered to in each case. "Osteon" and "interstitial" properties refer to the mechanical or microstructural properties of the osteons or interstitial bone fragments, respectively.

continuum level specimens (Chapter 6). Thus the predicted behavior could only be compared qualitatively to experimental results since the quantitative results (elastic modulus, yield point, etc.) were input parameters for the model. Since the purpose of these models is to motivate the more detailed model described in the next section, the methods as well as the results for these models will be described in this section.

Krajcinovic assumed that osteons failed by pulling out of the matrix of interstitial bone. The strength of each osteon was then dependent on a random variable, the embedded length of the osteon, which was selected from a statistical distribution. No assumption about the failure mechanism will be made here, and furthermore, the model will be reformulated with displacement, rather than load as the failure criteria. In this case, the displacement required to break each osteon will be selected from a statistical distribution. Assuming that the displacement required to break each osteon is random and uniformly distributed over a range of possible values (from 0 to δ_{max}; Figure 7.4), the probability density function for the displacement which causes the osteon to break, δ_i^{break} is:

$$p(\delta_i^{break}) = \frac{1}{\delta_{\max}}. \tag{1}$$

Since the osteons are first assumed to behave in a linear-elastic fashion, with no post-yield deformation, the constitutive law for Force in the i^{th} osteon, F_i, is:

$$F_i = \frac{K\delta}{N} \text{ for } 0 \le \delta \le \delta_i^{break} \tag{2}$$

$$F_i = 0 \text{ for } \delta > \delta_i^{break} \tag{3}$$

where δ is the displacement of the model, K is the apparent stiffness, and N is the number of osteons in the model. The forces in all the osteons can then be summed to get the apparent force in the model:

$$F_{app} = \sum_{i=\overline{N}+1}^{N} F_i = K\delta\left(1-\frac{\overline{N}}{N}\right) = K\delta(1-\omega) \tag{4}$$

where $\overline{N}$ is the number of osteons that have reached their failure displacement, and ω is the damage parameter, defined as:

$$\omega = \frac{number\ of\ failed\ osteons}{total\ number\ of\ osteons}. \tag{5}$$

Note that ω=0 indicates that there is no damage—all the osteons are intact, and ω=1 indicates a fully damaged state—where no osteons can bear any load. For a continuous probability distribution, ω is given by the integral of the probability density function from negative infinity to the current displacement (Figure 7.4) Similarly, the fraction of intact osteons, (1-ω), is given by the integral from the current displacement to infinity. The equilibrium equation (4) can then be rewritten in integral form for a large number of osteons as:

$$F_{app} = K\delta\int_{\delta}^{\infty} p(\delta_i^{break})d\delta_i^{break}. \tag{6}$$

where the integral represents the fraction of osteons that have not yet failed, (1-ω). For a constant probability density function with bounds of 0 and δ_{max}, the integral is:

$$\int_{\delta}^{\delta_{max}} p(\delta_i^{break})d\delta_i^{break} = 1-\omega = (\delta_{max}-\delta)\frac{1}{\delta_{max}}, \tag{7}$$

and the damage parameter is:

$$\omega = \frac{\delta}{\delta_{max}}. \tag{8}$$

Combining (8) with (4) the constitutive relation for the model can be written as:

$$F_{total} = K\delta\left(1 - \frac{\delta}{\delta_{\max}}\right), \tag{9}$$

which is quadratic in displacement. The stress-strain response predicted by this model is therefore parabolic (Figure 7.2).

The preceding equations can be rewritten in terms of apparent stress and strain by introducing the following relations:

$$F=A\sigma; \qquad K=AE/L; \qquad \delta=L\varepsilon, \tag{10}$$

where A and L are the original cross-sectional area and length of the material, E is the elastic modulus and σ and ε are the apparent stress and strain, respectively:

$$\sigma = E\varepsilon\left(1 - \frac{\varepsilon}{\varepsilon_{\max}}\right) \tag{11}$$

where ε_{max} is the maximum failure strain in any osteon, determined by a statistical distribution.

The first shortcoming of the Krajcinovic model is the lack of an initial linear regime in the stress-strain response. The response is non-linear from the onset since the uniform distribution of osteon strengths has a lower bound of zero. An initial linear regime is created by simply increasing the lower bound of the statistical distribution of displacements that cause failure in the osteons. In this case, the probability density function (Figure 7.4) is given by:

$$p(\delta_i^{break}) = \frac{1}{\delta_{\max} - \delta_{\min}}. \tag{12}$$

In this model, the failure strains, rather than displacements vary from a non-zero minimum value, ε_{min}, to a maximum value ε_{max} but the equations are similar. The constitutive equation is then:

$$\sigma = [1-\omega]E\varepsilon \text{ for } 0 \le \omega \le 1 \tag{13}$$

where

$$1-\omega = \left[\frac{\varepsilon_{\max} - \varepsilon}{\varepsilon_{\max} - \varepsilon_{\min}}\right] \tag{14}$$

and σ is the apparent stress, E is the apparent Young's modulus and ε is the apparent strain in the model. At strains below the minimum osteon failure strain, ε_{min}, equation (13) is replaced with

$$\sigma = E\varepsilon \text{ for } 0 \le \varepsilon \le \varepsilon_{\min}. \tag{15}$$

This model has two degrees of freedom: ε_{min} and ε_{max}. Increasing these parameters increases the strain at the yield point—where the curve becomes nonlinear—and the failure point respectively. Additionally, the apparent ultimate stress is proportional to both ε_{min} and ε_{max}. The discontinuity in the stress-strain response is due to the abrupt onset of failure caused by the use of a uniform distribution of failure strains. A normal distribution of failure strains provides continuity of slopes between the linear and non-linear regions of the response. The addition of a linear regime brings the model into good agreement with experimental data from a qualitative standpoint in the elastic and knee regions, but does not predict the linear post-yield region (Figure 7.2). Again, no significance should be associated with the good quantitative agreement between the apparent mechanical properties of the model and experimental results, since the osteon mechanical properties were selected from the apparent experimental data.

The second shortcoming of the Krajcinovic model is the lack of a linear post-yield region in the stress-strain response. This type of response, although observed experimentally in cortical bone, is not displayed by the model since the osteons in the model are assigned a linear-elastic constitutive response. This shortcoming can be addressed by assuming an elastic-plastic constitutive behavior for each osteon rather than an elastic-brittle one.

To create a smooth transition between the elastic and post-yield regimes, the yield strain rather than the failure strain of each osteon is varied. Since only one input parameter was assigned from a statistical distribution, the failure strain of each osteon is constant, ε_f. This limits the failure strain of the model to a constant value, ε_f. The yield strains in the osteons vary with a constant probability from ε^y_{min} to ε^y_{max}. The value of ε^y_{min} determines the onset of yielding and ε^y_{max} determines the strain when all osteons have yielded and are deforming plastically. There are three distinct regions in this model. The first region is linearly elastic with a slope equal to the modulus of the osteons. The governing equation in this region is:

$$\sigma = E\varepsilon \text{ for } 0 \le \varepsilon \le \varepsilon^y_{\min}. \tag{16}$$

The second region, $\varepsilon^y_{min} < \varepsilon < \varepsilon^y_{max}$ is parabolic and links the linear elastic region to the (linear) perfectly plastic region. Stress is determined by adding the forces in the plastically deforming osteons (those that have passed their yield point) to the forces in the elastically deforming osteons (which have not reached their yield point). Since forces, and not stresses, must be summed, this part of the constitutive law is first given in units of force and displacement and then converted to units of stress and strain. The total force in the osteons that are deforming elastically is:

$$F_{elastic} = \left[\frac{x^y_{\max} - x}{x^y_{\max} - x^y_{\min}}\right] Kx. \tag{17}$$

where the bracketed quantity is the fraction of osteons that have not yielded *(1-ω)* and *F*, *k*, and *x* are the force, stiffness and elongation in the elastically deforming osteons, respectively.

The force in the plastically deforming osteons must also be summed. Since each osteon has a different yield strain but a common elastic modulus, the force in an osteon after yielding occurs is linearly proportional to the yield strain of that osteon. The average yield strain of the already yielded osteons is halfway between the minimum osteon yield strain and the current strain, since the probability distribution function is constant. The total force in the plastically deforming osteons is then:

$$F_{plastic} = \left[\frac{x - x^{y}_{\min}}{x^{y}_{\max} - x^{y}_{\min}}\right] K\left(\frac{x + x^{y}_{\min}}{2}\right) \tag{18}$$

and the total force is:

$$F = F_{elastic} + F_{plastic} \tag{19}$$

Substituting equations (17) and (18) into (19):

$$F = \left[\frac{x^{y}_{\max} - x}{x^{y}_{\max} - x^{y}_{\min}}\right] Kx + \left[\frac{x - x^{y}_{\min}}{x^{y}_{\max} - x^{y}_{\min}}\right] K\left(\frac{x + x^{y}_{\min}}{2}\right) \tag{20}$$

Converting into apparent stress and strain using (10):

$$\sigma = \left[\frac{\varepsilon^{y}_{\max} - \varepsilon}{\varepsilon^{y}_{\max} - \varepsilon^{y}_{\min}}\right] E\varepsilon + \left[\frac{\varepsilon - \varepsilon^{y}_{\min}}{\varepsilon^{y}_{\max} - \varepsilon^{y}_{\min}}\right] E\left(\frac{\varepsilon + \varepsilon^{y}_{\min}}{2}\right) \text{for } \varepsilon^{y}{}_{\min} < \varepsilon < \varepsilon^{y}{}_{\max}. \tag{21}$$

In the third region all rods in the model are deforming plastically. Again the mean value of the yield strain distribution is used for the strain:

$$\sigma = E\left(\frac{\varepsilon^{y}_{\min} + \varepsilon^{y}_{\max}}{2}\right) \text{ for } \varepsilon^{y}{}_{\max} < \varepsilon < \varepsilon_{f}.. \tag{22}$$

This model has two degrees of freedom: ε^{y}_{min} and ε^{y}_{max}. Increasing these parameters increases the apparent strain at the onset of yielding—where the curve becomes nonlinear—and the completion of yielding—where all the osteons deform plastically. Again, the ultimate strength is proportional to both ε^{y}_{min} and ε^{y}_{max}. The addition of the elastic-plastic constitutive behavior improves the qualitative agreement between the model and experimental data (Figure 7.3). Again, no significance should be associated with the good quantitative agreement between the curves, since the input parameters were selected from the experimental data.

While these models can predict the qualitative stress-strain behavior of cortical bone they are limited in that only a single input parameter is allowed to vary in a given model and thus the full intra-specimen heterogeneity of cortical bone is not adequately represented. Additionally, the model employs an integral rather than summation in the solution, thereby assuming an infinite number of osteons while at the same time neglecting interstitial bone. In real bone, of course, there are a finite number of osteons and the interstitial bone does contribute to the stress-strain response. A final limitation is that these models do not account for porosity, which will decrease the stiffness and strength of the material. All of these limitations will be addressed in the model described in the next section.

Theory

A more complex model of cortical bone was developed based on the original model developed by Krajcinovic and expanded in the previous section. Each shortcoming of the previous models was addressed specifically, and the result was a more general model of cortical bone. This section will present the governing equations and derivation of the model. Specific values of input parameters will be described in the next two sections: the baseline case and the sensitivity analysis.

Since elastic behavior alone was not capable of completely matching the stress-strain response of bone (Figure 7.2), an elastic-hardening constitutive response was used.

The elastic-perfectly plastic response used in the previous model (Figure 7.3) is a special case of this model, where the slope of the hardening (post-yield) modulus is set equal to zero. The interstitial bone was modeled explicitly, and separately from the osteons, so that each material had mechanical properties which were assigned independently. The size of the specimen in the model was fixed, so that the model would include a finite number of osteons and interstitial bone fragments thus allowing the use of a summation rather than integration techniques. In order to incorporate more intra-specimen heterogeneity, all mechanical properties—elastic modulus, yield strain, hardening modulus, and failure strain—were assigned to each osteon and each fragment of interstitial bone according to independent statistical distributions. Osteon and Haversian canal diameters were set according to a statistical distribution also, and porosity was modeled explicitly via the Haversian canals, which were considered to have stiffness and strength equal to zero. Finally, since so many parameters were assigned simultaneously from statistical distributions, a Monte Carlo simulation was used to run each model multiple times, thus simulating an experiment with a mean value and a standard deviation for each output parameter representing the inter-specimen heterogeneity.

Small blocks of cortical bone were modeled as a set of parallel circular osteons with concentric circular Haversian canals embedded in a matrix of interstitial bone. The apparent specimen size was 2 mm x 3 mm x 10 mm in all models, selected to mimic specimens used in mechanical testing (Chapter 6). The cross-section of the specimen was constant. The first step in building each model was to select the number of osteons and interstitial fragments. Each osteon was then assigned an inner and outer diameter according to a beta distribution. A beta distribution was used to eliminate numerical instabilities due to extrema occasionally found in normal distributions. Each beta distribution required a mean value, coefficient of variation, and a minimum and maximum value. The porosity, osteonal bone

fraction, and corrected osteonal bone fraction[2] were calculated based on the osteon diameter distributions and the specimen size as:

$$porosity = \frac{\frac{\pi}{4}\sum_i HCD_i^2}{w * t}, \tag{23}$$

$$Ost\_Frac = \frac{\frac{\pi}{4}\sum_i OD_i^2}{w * t}, \tag{24}$$

and

$$Cor\_Ost\_Frac = \frac{\frac{\pi}{4}\left(\sum_i OD_i^2 - \sum_i HCD_i^2\right)}{w * t - \frac{\pi}{4}\sum_i HCD_i^2}, \tag{25}$$

respectively, where HCD_i and OD_i are the diameters of the i^{th} Haversian canal and osteon, *Ost_Frac* and *Cor_Ost_Frac* are the uncorrected and corrected osteonal bone fraction, and w and t are the width and thickness of the specimen. The fraction of interstitial bone was then calculated as:

$$Int\_Frac = 1 - Ost\_Frac \tag{26}$$

and the cross-sectional area of each interstitial fragment was given by:

$$Int\_Area = \frac{Int\_Frac * w * t}{n_{int}} \tag{27}$$

[2] The osteonal bone fraction and corrected osteonal bone fraction refer to the relative area occupied by osteons in the whole specimen including and excluding porosity, respectively and has been used previously by other authors (10, 19).

where n_{int} is the number of interstitial fragments. After completing the assignment of microstructural properties, mechanical properties were assigned to each osteon and interstitial bone fragment.

Elastic stiffness, displacement at yield, post-yield stiffness, and displacement at failure were assigned to each osteon and each interstitial bone fragment according to beta distributions. In general, different distributions were used for the interstitial bone and the osteons (see next section). Forces, displacements and stiffnesses were used in the model rather than stress, strain and moduli, since the osteons varied in size and thus forces, rather than stresses, were summed in order to obtain the total force on the model. After force-displacement data were obtained from each model, they were converted into stress and strain data.

Since experimental results are generally reported as material properties and not structural properties, input parameters were converted back into structural properties before being input to the model. The mean stiffness in the osteons, $\bar{k}^o$, was calculated using the following formula:

$$\bar{k}^o = \tfrac{\pi}{4}(\overline{OD}^2 - \overline{HCD}^2)\frac{\overline{E^{ost}}}{l} \tag{28}$$

where $\overline{E^{ost}}$ is the average elastic modulus of the osteons, l is the length of the specimen (10 mm), and $\overline{OD}$ and $\overline{HCD}$ are the mean diameters of the osteons and Haversian canals, respectively. Since elastic stiffness was linearly proportional to elastic modulus, the coefficient of variation, and minimum, and maximum values for the stiffness distribution were scaled from the desired elastic modulus values. The post-yield stiffness of the osteons was set similarly to the elastic stiffness, except that the experimental post-yield modulus was used to determine the mean, coefficient of variation, maximum and minimum values in the post-yield stiffness distribution. Since the length of the model was constant (10 mm),

the deformation at both yield and failure were calculated by multiplying the desired yield and failure strains by this length.

Mechanical properties were assigned to the interstitial bone in a similar manner. All the interstitial bone fragments were assumed to be solid and of the same size, so the average stiffness in the interstitial bone was given by:

$$\bar{k}^{int} = Int\_Area\frac{\overline{E^{int}}}{l} \tag{29}$$

where $\overline{E^{int}}$ is the average elastic modulus in the interstitial bone and *Int_Area* is given by equation (27). Again, the coefficient of variation, and minimum and maximum values for the stiffness distribution were scaled from the desired elastic modulus values. The post-yield stiffness of the interstitial bone was set in the same manner as for the osteons, except that different input parameters were used. For convenience, units of modulus and strain rather than stiffness and deformation are used in all tables of input parameters.

Stress-strain curves were generated from each model by calculating the apparent force on the model at strain levels from zero to 2.5% and dividing the force by the apparent cross-sectional area to obtain the stress. Total force was calculated as the sum of the force in each osteon plus the force in each interstitial bone fragment. The force at a displacement x_j for the i^{th} osteon or interstitial bone fragment was given by:

$$f_i = \begin{cases} k_i x_j \text{ if } x_j < x_i^{yield} \\ k_i x_i^{yield} + h_i(x_j - x_i^{yield}) \text{ if } x_i^{yield} \le x_j \le x_i^{fail} \\ 0 \text{ if } x_j \ge x_i^{fail} \end{cases} \tag{30}$$

where k_i and h_i are the elastic and post-yield stiffnesses of the i^{th} component (osteon or interstitial bone fragment) respectively, and superscripts denote the yield and failure displacements. Apparent stress and strain were calculated by dividing force by the apparent cross-sectional area and dividing the displacements by the length of the specimen,

respectively. Elastic modulus was calculated as the slope in the initial region of the stress-strain curve; the yield point was calculated using the 95% secant method; the ultimate point was calculated as the point of maximum stress; and the post-yield modulus was calculated as the slope immediately prior to the ultimate point (Figure 7.1).

To obtain a statistical distribution of mechanical properties, the process described above (assigning microstructural and mechanical properties, summing the forces in the osteons and interstitial bone and calculating mechanical properties) was run multiple times, each with a different distribution of microstructural and mechanical properties (*i.e.* a Monte Carlo simulation). Summary statistics (mean, standard deviation, maximum and minimum) were calculated for each set of simulations.

Methods

Baseline case

In order to perform a sensitivity analysis on the input parameters in the model, a baseline case was first created. Some input parameters for the baseline case were taken directly from published studies of the apparent mechanical properties of bone tissue while others were estimated directly for osteons and interstitial bone based on results from other studies. For the baseline case and the sensitivity analysis of mechanical properties, there were 25 runs in each simulation and the number of osteons was fixed at 55. A convergence study indicated that 25 runs was sufficient to produce average microstructural and mechanical properties within 3% of the average value of 100 simulations (Appendix D). Models with 55 osteons had porosity values of 13.5% and osteonal bone fractions of approximately 54%, on average (Table 7.3).

The osteon diameter was assigned from a beta distribution with a mean ± SD of 252 ± 107 μm. The minimum and maximum for the beta distribution used to assign osteon diameter were 100 μm and 572 μm, respectively. For each osteon, the Haversian canal diameter was set equal to one half of the osteon diameter. These values were selected

based on the measurements of osteons and Haversian canals in tibial cortical bone from seven cadavers ranging in age from 21 to 83 years (183). The minimum and maximum for all other beta distributions (used to assign mechanical properties) were two standard deviations less than and greater than the average value, respectively.

Rho *et al.* (184) measured the elastic moduli of dehydrated osteons and interstitial bone using nanoindentation tests. Values of 25.8 ± 0.7 GPa (mean $\pm$ SD) and 22.5 ± 1.3 GPa were reported for the interstitial and osteonal bone tissue, respectively. These mean values were reduced by 25% to account for the 20-30% increase in stiffness that occurs with dehydration (139, 185). The elastic moduli used for the baseline case were therefore: 19.4 ± 0.7 GPa and 16.9 ± 1.3 GPa for the interstitial and osteonal bone, respectively (Table 7.1). The maximum and minimum values were set to two standard deviations above and below the mean value for each group, respectively.

No measurements of the yield strain in either osteons or interstitial bone have been reported. Ascenzi and Bonucci measured the elastic modulus and ultimate stress for various types of isolated osteons (121). They employed a microwave extensometer to measure strain, and measured values of failure strain in single osteons 3-4 times higher than observed in machined specimens of cortical bone. Additionally, demineralized osteons also failed at strains 3-4 times higher than demineralized cortical bone. Thus while the strength values seem reliable, modulus values, which rely on the strain measure, may not be. Ascenzi and Bonucci also reported that the "proportional limit is only about half the breaking stress" for each osteon (121). This has been confirmed more recently (186). The average yield strain in the osteons can therefore be estimated by dividing the ultimate tensile strength by two (to get the yield strength) and then dividing by the average elastic modulus of the osteons (given above). Using Ascenzi and Bonucci's strength values and a constant elastic modulus of 16.9 GPa, gives yield strains ranging from an average of 0.26% for lowly calcified osteons to an average of 0.36% for highly calcified osteons, with an average of 0.31%. Thus the yield strain for the osteons was selected from a beta

distribution with a mean ± SD of 0.31 ± 0.05%. Since interstitial bone is thought to be more highly mineralized than osteons (121) and since the yield strain of osteons increased with calcification (0.36% vs. 0.26% in highly vs. lowly calcified osteons (121)) a yield strain of 0.39 ± 0.05% was assumed for the interstitial bone. This mean value was selected to be greater than the yield strain of highly calcified osteons but with less of a difference between the yield strains of interstitial bone and highly calcified osteons compared to the difference between the yield strains of highly and lowly calcified osteons. The standard deviation was assumed to be the same in the interstitial bone and in the osteons.

Like yield strain, no data are available for the post-yield modulus of either osteons or interstitial bone. The elastic modulus of interstitial bone is approximately 15% higher than the elastic modulus of osteons (184). Accordingly, post-yield modulus will be assumed to be different by 15% also. Since the higher level of mineralization in interstitial bone may be the cause of the increased elastic modulus relative to osteonal bone, the opposite will be assumed about the post-yield modulus. That is, since the interstitial bone has a lower organic fraction (*i.e.* a higher mineral fraction) the post-yield modulus of interstitial bone is assumed to be lower than the post-yield modulus of osteons. That difference will be set to 15%. Furthermore, since the elastic modulus of osteons and machined specimens of cortical bone are similar (16.9 ± 1.3 GPa vs. 17.7 ± 1.5 GPa, respectively) the post-yield modulus of osteons was selected from a distribution with a mean ± SD equal to that measured from machined specimens of cortical bone (714 ± 207 MPa; Chapter 6). The post-yield modulus of the interstitial bone was selected from a distribution with a mean ± SD of 607 ± 178 MPa (mean was reduced 15%, coefficient of variation was the same as for the osteons).

The final mechanical property that had to be assigned to the osteons and the interstitial bone fragments was failure strain. Ascenzi reported failure strains, but as discussed above, they are much higher than would be expected based on test results from

machined specimens (121). However, even if Ascenzi and Bonucci's failure strain values are high, they were probably systematically high, and so the variation they observed is likely representative of the true variation. Furthermore, there is no evidence to suggest that the failure strain of osteons and interstitial bone should be different. As an initial approximation of the mean failure strain in osteons and interstitial bone fragments, the mean failure strain of machined cortical bone samples (1.63%) was selected. The coefficient of variation was set to 30%, approximately in the middle of the values obtained by Ascenzi and Bonucci (121). This resulted in a failure strain distribution of 1.63 ± 0.50 %. Coincidentally, the standard deviation (0.50%) is very similar to that measured for machined samples of cortical bone (0.54%).

Sensitivity study of mechanical properties

In order to determine the sensitivity of the output parameters to the input mechanical properties, the mean value of each mechanical property (elastic modulus, yield strain, post-yield modulus, failure strain) was increased and decreased by two standard deviations while keeping the coefficient of variation constant. All other parameters were assigned from distributions with the same mean and standard deviation that were used in the baseline case (Table 7.2). The number of osteons in each model was kept constant at 55 to reduce the variation in the output parameters and simplify comparisons between different models. One parameter, failure strain, could not be reduced by two standard deviations since negative values would have been assigned to some elements and since failure strain would have been lower than yield strain in some elements therefore, it was increased by two standard deviations and decreased by only one standard deviation (Table 7.2).

Two additional models were created with all parameters simultaneously increased or decreased by two standard deviations (failure strain was only decreased by one SD) in order to investigate the interaction effects of different properties. The sensitivity of the model-predicted apparent mechanical properties to the mean values of input parameters was

quantified by calculating the percent change in the predicted value of each mechanical property for each change in input parameter.

Calibration

Stress-strain curves and apparent mechanical properties measured experimentally (Chapter 6) were compared to the baseline model and models with different input parameters. Input parameters used in the sensitivity analysis which provided the closest match between the model and the experimental results described in Chapter 6 were then selected for the microstructural parameter study. This calibration allowed for direct comparisons between the results of the subsequent microstructural parameter study and experimental results.

Microstructural parameter study

After calibrating the model, the role of porosity, osteonal bone fraction (uncorrected and corrected), and osteon size were investigated. Since the model was programmed into a Monte Carlo simulation, porosity and osteonal bone fraction could be varied within one simulation (*i.e.* multiple runs of the model) by allowing the number of osteons to be set randomly for each run within the simulation. For these studies, the number of runs in each simulation was set to 100 and the number of osteons was assigned a number randomly selected from a uniform distribution from 40 to 70. This range of osteon numbers spanned the physiological range of both porosity and osteonal bone fraction. The role of porosity and osteonal bone fraction in the mechanical properties of bone was then investigated using linear regression analysis of mechanical properties vs. porosity, osteonal bone fraction and corrected osteonal bone fraction.

The role of porosity was further investigated by changing the Haversian canal diameters. The Haversian canal diameters were set equal to 60% and 40% of the osteon diameters, compared to 50% for the baseline case. The number of osteons in these simulations was changed simultaneously in order to maintain a porosity values within the

physiological range. The bounds on the number of osteons were 30 and 60 for the model with larger Haversian canals and 50 and 80 for the model with smaller Haversian canals. Finally, the role of osteon size was investigated by increasing and decreasing the mean osteon diameter, to 200 μm and 300 μm, respectively, while keeping the Haversian canal diameters equal to half of the osteon diameters. Again, the number of osteons was changed simultaneously, to 40-130 and 20-50, respectively, in order to maintain a physiological range of porosity values.

Results

Sensitivity study and calibrated model

The baseline model did not predict the shape of the stress-strain curve of cortical bone (Figure 7.3). Instead, the model predicted a linear region followed by a yield point and subsequent softening, due to osteons and interstitial bone fragments failing at strains as low as 0.63% (the minimum value of the beta distribution used to assign failure strain). Additionally, The model did not predict the sudden failure observed experimentally, but rather that the stress reduced gradually until all osteons and interstitial bone fragments had failed. These differences were reflected in the predicted apparent mechanical properties which were lower than experimental values by 6 to 59% although the variation in the predicted apparent propertied was much less than that observed experimentally for most mechanical properties (Table 7.3).

The sensitivity analysis demonstrated that the former discrepancy was eliminated when the mean failure strain was increased by two standard deviations (Figure 7.3d). In this case, the model accurately predicted the stress-strain response of cortical bone up to the ultimate point. After the ultimate point, the model still predicted a slow decline in stress, rather than the catastrophic failure observed experimentally (Figure 7.3d). Interestingly, the apparent ultimate stress was reached immediately prior to failure of the first osteon or

interstitial bone fragment. This result is not obvious since the remaining intact material is still in a hardening regime, that is, the post-yield stiffness is positive.

All but one mechanical property of the osteons and the interstitial bone had to be increased in order to match experimentally observed apparent properties. Increasing elastic modulus and yield strain brought the model predictions closer to bone behavior (Figure 7.3a and b); while changing post-yield modulus had little effect (Figure 7.3c). Increasing all input values simultaneously brought the model into good agreement with experimentally observed behavior (Figure 7.3e). Two input parameters—elastic modulus and yield strain—had substantial affects on multiple mechanical properties (Table 7.4). For example, increasing elastic modulus of the osteons and interstitial bone by an average of 12% (16% in the osteons and 8% in the interstitial bone) caused 6-9% increases in elastic modulus, yield stress, post-yield modulus and ultimate stress and a 16% reduction in ultimate strain. In contrast, changing the other two input parameters—post-yield modulus and failure strain—had little affect on other mechanical properties. Neither the elastic modulus nor the yield stress or strain were changed by increasing or decreasing the mean value of post-yield modulus or failure strain.

There were large differences in the post-yield modulus predicted from all the models (Table 7.4), but these differences were due to the absence of a linear post-yield region in most of the predicted stress-strain responses. The failure strain was increased in the calibrated model to ensure a linear post-yield region, thereby eliminating this problem from subsequent analyses. Decreasing each input parameter caused changes of similar magnitude but opposite direction to those caused by increasing the same parameter.

Taken collectively, the results of the sensitivity analysis indicated that all input values except post-yield modulus had to be increased in order to mimic the stress-strain response and the apparent mechanical properties of cortical bone. The calibrated model therefore had input parameters two standard deviations above baseline values except post-yield modulus, which was kept at the baseline value (Table 7.4). The calibrated model

predicted the mechanical properties of cortical bone within 15% for all properties except post-yield modulus, which was 26% lower than the measured value (Table 7.5). The average porosity, osteonal bone fraction and corrected osteonal bone fraction in the baseline model were 13.5% and 53.8% and 45.2%, respectively (Table 7.5).

Microstructural parameter study

The microstructural parameter study revealed that all mechanical properties except failure strain decreased with increasing porosity and osteonal bone fraction (Figure 7.4, Figure 7.6). Additionally, both corrected and uncorrected osteonal bone fraction were highly correlated with porosity ($r^2 > 0.98$ for both regressions; Figure 7.8). This result indicated that osteonal bone fraction and porosity were not independent measures of the microstructure of the model. This result is not surprising since the Haversian canals are the only source of porosity in the model. Porosity was therefore selected as the independent variable for the analysis of microstructure and mechanical properties.

The relationships between apparent modulus, and apparent yield and ultimate stress vs. porosity were different for different Haversian canal diameters (Figure 7.6, Figure 7.7). The apparent elastic modulus decreased with Haversian canal diameter at a fixed porosity. Additionally, the negative slope of the apparent modulus vs. porosity regressions decreased with decreasing Haversian canal diameters (Figure 7.5), indicating there was a greater effect at higher values of porosity. Similar trends were observed for apparent yield and ultimate stress (Figure 7.6). In contrast, no differences in any mechanical property were observed in models with different mean osteon size, when plotted against porosity (Figure 7.4, Figure 7.5).

Discussion

Overall, the model was able to accurately predict the stress-strain response, and provide insight into the relationship between microstructure and the apparent mechanical properties of bone. Specifically, the mechanical properties of osteons and interstitial bone

had to be increased in order to accurately predict the apparent mechanical properties of bone. The model predicted that apparent mechanical properties decrease with increasing porosity, and further that the Haversian canal diameter, relative to the osteon diameter, also affects apparent mechanical properties. The model is therefore a useful tool in investigating the relationship between the microstructure and the mechanical properties of cortical bone and could easily be expanded to include additional microstructural elements such as cement lines and lamellae. The relatively simple changes from the model originally proposed by Krajcinovic caused substantial improvements in its predictive power.

The greatest strength of this study is the agreement between the predicted relationships of both elastic modulus and ultimate stress vs. porosity and published regressions based on experimental findings. Furthermore, the use of a Monte Carlo simulation allowed for all input parameters—mechanical and microstructural—to be selected randomly for each element in the model, thus mimicking the heterogeneity of bone tissue. Closed-form analysis prohibits the random assignment of more than one input parameter. The Monte Carlo simulation also enabled the porosity and osteonal bone fraction to be varied within a single simulation, thus simplifying the investigation of microstructure and mechanical properties.

Although the model accurately predicted the stress-strain response of cortical bone, it must be recognized that some of the input parameters were selected based on experimental results from macroscopic specimens (*i.e.* specimens larger than single osteons or interstitial fragments). These input parameters, post-yield modulus and failure strain, were selected based on apparent behavior, since there are no reliable data available on either of these parameters for osteons or interstitial bone. Ascenzi (121) reported failure strains for single osteons, but the values were much higher than expected for highly mineralized osteons. Elastic modulus values reported in the same study were substantially lower than reported values for macroscopic samples and osteons tested with other techniques. These discrepancies can both be explained by artificially high strain measurements, suggesting

that the microwave extensometer used by Ascenzi was not sufficiently accurate. Other input parameters, elastic modulus, yield strain, and osteon and Haversian canal diameters, were selected based on experimental results of apparent properties for the baseline case.

Sensitivity analysis indicated that all mechanical properties except post-yield modulus had to be increased by two standard deviations in order to accurately predict the mechanical properties of cortical bone. This suggests that: 1) the mechanical properties of osteons and interstitial bone may be substantially greater than the apparent properties; and 2) variance in the mechanical properties of the osteons and interstitial bone reduces the apparent properties. The second point is most obvious in the case of yield strain. For example, if the yield strain of all osteons and all interstitial bone fragments were set to a constant value of 0.4%, the apparent yield strain would also be 0.4%. If, instead, the yield strain of the osteons and interstitial bone fragments was assigned separately for each element from a beta distribution with and mean $\pm$ SD of $0.40 \pm 0.05\%$, some components could be assigned yield strains of less than 0.30% which would cause the apparent stress-strain behavior to become non-linear at this strain. Since the apparent yield strain is measured as a deviation from linearity, variance in the yield strains of the osteons and interstitial bone would cause the apparent yield strain to drop below 0.40%. This affect was confirmed by increasing the coefficient of variation of the yield strain distribution for both the osteons and interstitial bone by a factor of five while keeping the mean yield strains and all other input parameters constant relative to the calibrated model. The resulting model predicted apparent yield strains that were substantially lower, on average, and had more variation compared to the calibrated model ($0.16 \pm 0.04\%$ vs. 0.45 ± 0.01, respectively).

The aim in creating the calibrated model was to simplify comparisons between the model predictions and experimental results. The trends that were predicted by the model—a reduction in apparent ultimate stress with increasing porosity, for example—would have been the same without the adjustments, the mean values would have been different, thus

making comparisons with published results more difficult. The role of the variance of input parameters on the model behavior was not investigated in detail, neither was the affect of altering osteon and interstitial bone properties independently. These are also limitations of the model which must be recognized, and possibly addressed in future work. A preliminary analysis did indicate that increasing the coefficient of variation of some input parameters did affect the model predictions. As described above, increasing the coefficient of variation of the yield strains in the osteons and interstitial bone decreased the apparent yield strain substantially. In contrast, increasing the variation in the elastic moduli of osteons and interstitial bone by a factor of five while keeping the mean values constant has little affect; the only difference was an increased coefficient of variation of the apparent modulus (6.4% vs. 5.0% for the calibrated model).

A final limitation was that porosity was only modeled via the Haversian canals. Although there is porosity due to lacunae and canaliculae, they sum to about 10% of the total porosity of cortical bone (187), and are therefore minor compared to Haversian porosity. Additionally, porosity due to lacunae and canaliculae is not usually included in experimental analysis (10, 12, 19), thus the predicted relationships between apparent mechanical properties and porosity should still match those determined experimentally. Porosity due to Volkmann's canals, however, may be similar in magnitude to Haversian porosity. Since all apparent mechanical properties decreased with increasing Haversian porosity, it is likely that the inclusion of Volkmann's porosity into the interstitial bone portion of the model will further reduce the apparent mechanical properties.

The elastic modulus vs. porosity relationship predicted by the calibrated model and models with increased or decreased Haversian canals agreed with the linear regression reported by Currey (188) in the porosity range of 7 to 12% (Figure 7.9). A second regression, an exponential relationship reported by Schaffler and Burr (189), crosses the first at about 5% strain but has a steeper slope than both Currey's regression and the model. The former regression was based on test specimens with porosity ranging from 3%

to 7% and therefore does not overlap the porosity range included in the models. Assuming the highly linear trend of the models continues at lower strains, however, suggests that a good agreement between the model and both published regressions can be expected in this lower porosity range. The relationship between ultimate stress and porosity was also similar to a published regression (Figure 7.10). Ultimate stress in the calibrated model decreased at a rate of 2.2 MPa/% porosity compared to 2.4 MPa/% porosity reported by McCalden *et al.* (19). The intercepts of the equations were also similar (109.5 MPa vs. 123.5 MPa) and would agree even more closely if the post-yield modulus of the osteons or interstitial bone were increased. The strong agreement between the model predictions and experimentally determined relationships between mechanical properties and porosity indicate that the model was capable of accurately predicting the relationship between the mechanical properties and the microstructure of bone

This is the first model to simulate the complete tensile stress-strain behavior of cortical bone. The model presented here is based on the continuum damage model originally proposed Krajcinovic. The main improvements to Krajcinovic's model include 1) explicit inclusion of interstitial bone, 2) an elastic-plastic constitutive response of the osteons and interstitial bone, and 3) a statistical distributions of all input parameters. Other continuum damage models have been used to predict damage behavior—the reduction in modulus upon reloading after loading past the yield point has occurred—but not the initial stress-strain response (180, 181). The model presented here can be used to investigate both the initial and reloading stress-strain response, although only the former has been addressed here. Other methods have been used to model the elastic behavior of cortical bone, specifically homogenization theory (176, 178) and finite element methods (177). While these techniques have been limited to the elastic behavior thus far, both models predict a linear relationship between modulus and porosity similar to that reported here (177, 178).

Two important motivations for developing a model of any biological system include: 1) to predict the response of the system by varying input parameters that are difficult or impossible to control in an experimental situation; and 2) to solve the inverse problem—describe microscopic phenomena of the system using a model which matches the macroscopic behavior of the system. Both objectives have been met with the current model.

Input parameters were altered in a controlled manner in order to predict the dependence of the apparent properties to changes in these parameters. This was done with porosity, osteon size and Haversian canal size, and could be expanded to include combinations of these parameters or others such as specimen size, interstitial bone fragment size, or mechanical properties. The results indicated that all mechanical properties except ultimate strain decreased with increasing porosity and that at a given porosity, elastic modulus and yield and ultimate stress also decreased with average Haversian canal diameter. No relationship between mechanical properties and mean osteon diameter was predicted.

These results can be explained by considering a simpler model, a three-element parallel spring model. The elements in the model represent osteonal bone, interstitial bone and void space. Any mechanical property of the parallel spring model can then be obtained by taking a volume weighted average of the properties of the spring elements. First, recall that porosity was only modeled via Haversian canals, which were 25% of the volume of the osteons in the Monte Carlo simulations, thus

$$P = 0.25 v_{osteons} \tag{31}$$

where P is the porosity and $v_{osteons}$ is the osteonal bone fraction (*i.e.* the volume of osteons including the Haversian canals divided by the total volume). The modulus of the three-element parallel spring model is then given by:

$$E_{spring\_model} = PE_{void} + (v_{osteon} - P)E_{osteon} + v_{interstitial} E_{interstitial} \tag{32}$$

where E_{spring_model}, E_{void}, E_{osteon}, $E_{interstitial}$ are the elastic moduli of the three-element parallel spring model, the void space, the osteonal bone tissue, and the interstitial bone, respectively and $v_{interstitial}$ is the volume fraction of interstitial bone. Since the void space has no stiffness, $E_{void}=0$ and the right hand side reduces to two terms:

$$E_{spring\_model} = (v_{osteon} - P)E_{osteon} + v_{interstitial}E_{interstitial}. \quad (33)$$

Using the fact that the volume fractions must sum to one, and equations (31) and (33) gives:

$$E_{spring\_model} = 3PE_{osteon} + (1-4P)E_{interstitial}. \quad (34)$$

This equation is linear in P and can then be rearranged to:

$$E_{spring\_model} = E_{interstitial} + (3E_{osteon} - 4E_{interstitial})P. \quad (35)$$

A similar relationship can be obtained for post-yield modulus and yield and ultimate stress since these quantities (or more properly their structural analogs: stiffness and force) are summed among the elements of the model to determine the properties of the model. Yield and ultimate strain should not behave similarly however, since yield and failure strain are determined at the point when the first elements of the model yield and fail, respectively. Thus, modulus and stress properties should depend on porosity and strain properties should not, as the model predicted. In the three-element parallel spring model analogy, increasing osteon size has no affect on mechanical properties at a given porosity, since porosity and osteonal bone fraction are explicitly linked (*i.e.* equation 29 remains the same). Haversian canal diameter does affect mechanical properties however, since this changes the amount of void space relative to the osteonal bone fraction (*i.e.* equation 29 changes). Thus this three-element parallel spring model and the continuum damage model predict similar relationships between the microstructure and apparent properties of bone. The three-element parallel spring model lacks the variation obtained by using the continuum

damage model, since each input parameter is assigned a single value rather than a random value from a statistical distribution.

The second objective of models of biological systems, solving the inverse problem, was also addressed through the sensitivity analysis. Adjustments to the input parameters that were required to bring the model into agreement with experimental data may provide insight into the mechanical properties of osteons and interstitial bone. The sensitivity analysis indicated that all input parameters had to be increased in order to accurately predict the stress-strain response of bone. Although post-yield modulus of the osteons and interstitial bone was not increased in the calibrated model, this value had the greatest discrepancy with experimental results, 26%, and increasing it by one standard deviation would have produced more accurate results. This was not done since the sensitivity analysis was restricted to changes of two standard deviations in order to simplify the analysis.

Aside from post-yield modulus though, all input parameters were increased in order to bring the model into agreement with experimental results. This suggests that the elastic modulus and yield and failure strains of isolated osteons and interstitial bone are substantially higher than measured properties of larger samples. This is especially important for failure strain, since the lower mean value (1.63%) of failure strain used in the baseline case did not predict the linear post-yield region in the stress-strain response that has been observed experimentally. Higher failure strains are required to produce this linear post-yield region. This is supported by the high failure strains reported for isolated osteons, which ranged from 6.8-10.3%, the lower failure strains corresponding to osteons with higher elastic modulus, which ranged from 4.3 to 11.7 GPa (121). These strain measurements may be inaccurate, as discussed above, however, a correction factor can be obtained however, by dividing the reported elastic modulus by 16.9 GPa, the baseline value used for this study. The failure strains reported by Ascenzi can then be scaled down

using this correction factor. This yields failure strains from 2.6% to 4.7%, which are consistent with the values used as input parameters in the calibrated model ($2.6 \pm 0.5\%$).

While the high failure strains reported by Ascenzi (121) suggest that some osteons may be capable of very high strains before failure, such high strains are not realized *in situ* since catastrophic failure occurs after the first osteons fail. Bone fails quickly and catastrophically, but the model predicts a slow decline in stress after the ultimate point. The catastrophic failure observed experimentally suggests that complete failure occurs once the first few osteons have failed and that load can not effectively be redistributed at high strains. This phenomenon could be incorporated into the model by assuming that after a fixed number of osteons and interstitial bone fragments have failed, the model can no longer bear any load. This does not minimize the importance of microcracks, which are the basis for other continuum damage models (180, 181), but rather supports the idea that when a microcrack reaches a critical size, perhaps the diameter of an osteon, the amount of damage is too great for continued loading and complete failure ensues. The strain which determines when a critical crack size is reached in an osteon is the failure strain.

The model developed in this study has been validated by demonstrating good agreement between predictions from the model and results from experimental tests. This suggests that the model adequately represents the microstructure of cortical bone—at least within the scope of this study. Obviously, many simplifications were required in order to implement the model, and the roles of many microstructural features including individual lamellae, cement lines, porosity from sources besides Haversian canals, have not been considered. These features, as well as smaller ones like individual collagen and hydroxyapatite elements, should be considered for future refinements of this model. Neither hydroxyapatite nor collagen exhibit post-yield deformation like that observed in bone. Since osteons without such post-yield deformation can not accurately model the stress-strain response of bone, the interface between the hydroxyapatite and collagen must be the source of this post-yield behavior. The inclusion of more microstructural features,

along with individual elements of hydroxyapatite and collagen may provide more accurate results and more insight into the inverse problems of bone mechanics.

Table 7.1. Input parameters for baseline model.

	Osteon	Interstitial Bone
Diameter (μm)	252 ± 107 (100—572)	NA
Haversian Canal Diameter (μm)	111 ± 47 (44—252)	NA
Elastic Modulus (GPa)	16.9 ± 1.3 (14.3—19.5)	19.4 ± 0.7 (18.0—20.8)
Post-yield Modulus (MPa)	714 ± 207 (300—1128)	607 ± 178 (251—963)
Yield Strain (%)	0.31 ± 0.05 (0.31-0.41)	0.39 ± 0.05 (0.29-0.49)
Failure Strain (%)	1.63 ± 0.50 (0.63—2.63)	1.63 ± 0.50 (.63—2.63)

Values are input parameters for the beta distribution function used to assign values to each osteon or the interstitial bone and are given as mean ± SD (lower limit—upper limit).

NA=property not applicable to interstitial bone.

Table 7.2. Mean values of input parameters for the baseline model, sensitivity analysis, and the calibrated model.

	Osteon		Interstitial Bone	
	Baseline	Alternate	Baseline	Alternate
Elastic Modulus (GPa)	16.9	14.3; 19.5	19.4	18.0; 20.8
Post-yield Modulus (MPa)	714	300; 1128	607	215; 963
Yield Strain (%)	0.31	0.31; 0.41	0.39	0.29; 0.49
Failure Strain (%)	1.63	1.13; 2.63	1.63	1.13; 2.63

Values are means of the beta distribution function used to assign values to each osteon or interstitial bone fragment. The coefficient of variation was the same in the baseline and all alternate cases.

The values listed for the alternate cases were used while all other properties remained at the baseline value. The underlined values were used for the input parameters for the calibrated and subsequent models.

Alternate cases for the osteons and the interstitial bone were changed simultaneously (*i.e.* mean post-yield modulus of 1128 MPa in the osteon corresponded to a mean post-yield modulus of 963 in the interstitial bone).

Table 7.3. Apparent mechanical properties of cortical bone from experimental data (n = 9) and the baseline model (n = 100).

	Experiment	Baseline Model	Average % Difference ††
Elastic Modulus (GPa)	17.7 ± 1.5 (14.6-19.4)	14.8 ± 0.6 (13.6-15.6)	-16
Yield Stress (MPa)	66.8 ± 7.7 (49.8-75.8)	46.8 ± 2.5 (40.6-51.2)	-30
Yield Strain (%)	0.41 ± 0.03 (0.35-0.44)	0.33 ± 0.01 (0.31-0.35)	-20
Post-yield Modulus (MPa)	714 ± 207 (429-993)	672 ± 607 (470-3541)	-6
Ultimate Stress (MPa)	95.0 ± 5.6 (86.0-102.9)	54.1 ± 2.6 (48.0-58.9)	-43
Ultimate Strain (%)	1.63 ± 0.54 (0.96-2.5)	0.67 ± 0.13 (0.44-0.98)	-59
Osteonal Bone Fraction (%)	NA	53.8 ± 5.4 (44.1-64.4)	—
Porosity (%)	NA	13.5 ± 1.4 (11.0-16.1)	—

All values are mean ± SD (range).

†† Average % difference is for baseline model compared to experimental data.

Experimental data was derived from the apparent properties reported in Chapter 6 and from previous studies by other authors (121, 183, 184).

Table 7.4. Sensitivity of the apparent mechanical properties of the model to input parameters. The two numbers below each input parameter entry are the coefficient of variation of the input parameters for the osteons and interstitial bone, respectively. Thus an increase of two standard deviations in elastic modulus of the osteons (a 16% increase) and the interstitial bone fragments (an 8% increase) resulted in 10%, 11%, and 10% increases in the apparent elastic modulus, yield stress, and ultimate stress of the model, respectively, but no changes in other apparent properties.

Input parameter	Z (SD)	Elastic modulus	Yield stress	Yield strain	Post-yield modulus†	Ultimate stress	Ultimate strain
Elastic modulus	+2	9	9	0	6	8	-16
(8%; 4%)	-2	-11	-10	0	-22	-10	0
Post-yield modulus	+2	0	0	0	49	0	0
(29%; 29%)	-2	0	0	0	-57	0	-4
Yield strain	+2	0	34	36	37	25	-6
(16%; 13%)	-2	0	-32	-33	-23	-24	0
Failure strain	+2	0	0	0	-24	7	130
(31%; 31%)	-2	0	0	0	457	-4	-36
All	+2	10	49	36	20	53	145
	-1‡	-10	-25	-18	-54	-26	-37

Z is the Z score of the change in input parameter (*i.e.* the number of standard deviations in the change).

Differences of less than 3% were considered to be due to random variation in the input parameters and not due to changes in the mean value of input parameters and, for convenience, were listed as 0 in the table. Other values were rounded to the nearest percent.

† Apparent post-yield modulus values differed widely since in most cases—including the baseline case—osteons and interstitial bone fragments began failing soon after the yield point and therefore there was no linear region to measure the post-yield modulus.

‡ In this case, the mean value of each properties was reduced by 2 SD except for failure strain which was reduced by 1 SD (see text for explanation).

Table 7.5. Apparent mechanical properties of cortical bone from experimental data (n = 9) and the calibrated model (n = 100).

	Experiment	Calibrated Model	Average % Difference ††
Elastic Modulus (GPa)	17.7 ± 1.5 (14.6-19.4)	16.4 ± 0.8 (13.7-18.2)	-7
Yield Stress (MPa)	66.8 ± 7.7 (49.8-75.8)	70.2 ± 5.1 (54.5-81.9)	5
Yield Strain (%)	0.41 ± 0.03 (0.35-0.44)	0.45 ± 0.01 (0.41-0.47)	10
Post-yield Modulus (MPa)	714 ± 207 (429-993)	527 ± 23 (456-572)	-26
Ultimate Stress (MPa)	95.0 ± 5.6 (86.0-102.9)	80.6 ± 5.5 (63.3-92.8)	-15
Ultimate Strain (%)	1.63 ± 0.54 (0.96-2.5)	1.52 ± 0.19 (1.06-1.96)	-7

All values are mean ± SD (range).

†† Average % difference is for calibrated model compared to experimental data.

Table 7.6. Apparent mechanical properties measured in experiments and predicted from the calibrated model and models with altered microstructure.

	Experiment	Calibrated Model	Small Haversian Canals	Large Haversian Canals	Small Osteons	Large Osteons
Elastic Modulus (GPa)	17.7 ± 1.5	16.4 ± 0.8	16.4 ± 0.7	16.2 ± 1.0	16.2 ± 1.4	16.7 ± 1.1
Yield Stress (MPa)	66.8 ± 7.7	70.2 ± 5.1	67.7 ± 4.4	71.1 ± 6.2	68.9 ± 8.2	72.0 ± 6.6
Yield Strain (%)	0.41 ± 0.03	0.45 ± 0.01	0.43 ± 0.01	0.46 ± 0.01	0.44 ± 0.02	0.45 ± 0.02
Post-yield Modulus (MPa)	714 ± 207	527 ± 23	541 ± 18	508 ± 28	520 ± 30	533 ± 27
Ultimate Stress (MPa)	95.0 ± 5.6	80.6 ± 5.5	78.3 ± 4.7	81.2 ± 6.5	78.8 ± 8.7	82.8 ± 6.8
Ultimate Strain (%)	1.63 ± 0.54	1.52 ± 0.19	1.51 ± 0.18	1.54 ± 0.23	1.51 ± 0.19	1.55 ± 0.24

All values are mean ± SD.

Results from mechanical testing experiment were obtained in the study described in Chapter 6.

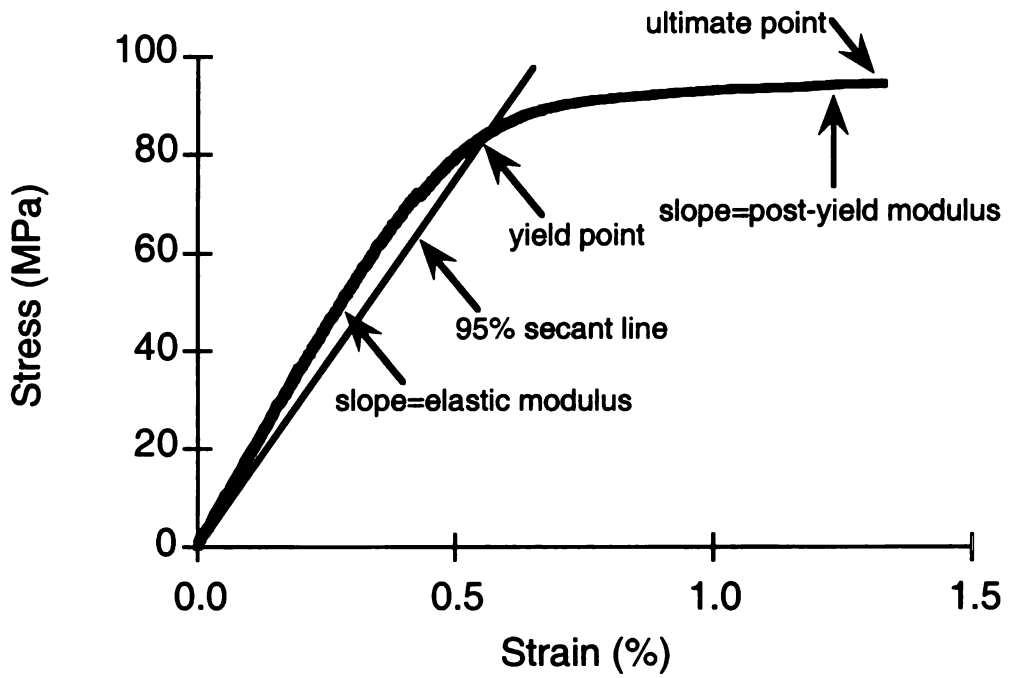

Figure 7.1. Typical stress-strain response of cortical bone with definitions of mechanical properties illustrated. The curve consists of an initial linear (elastic) region, a non-linear knee, and a second linear (post-yield) region.

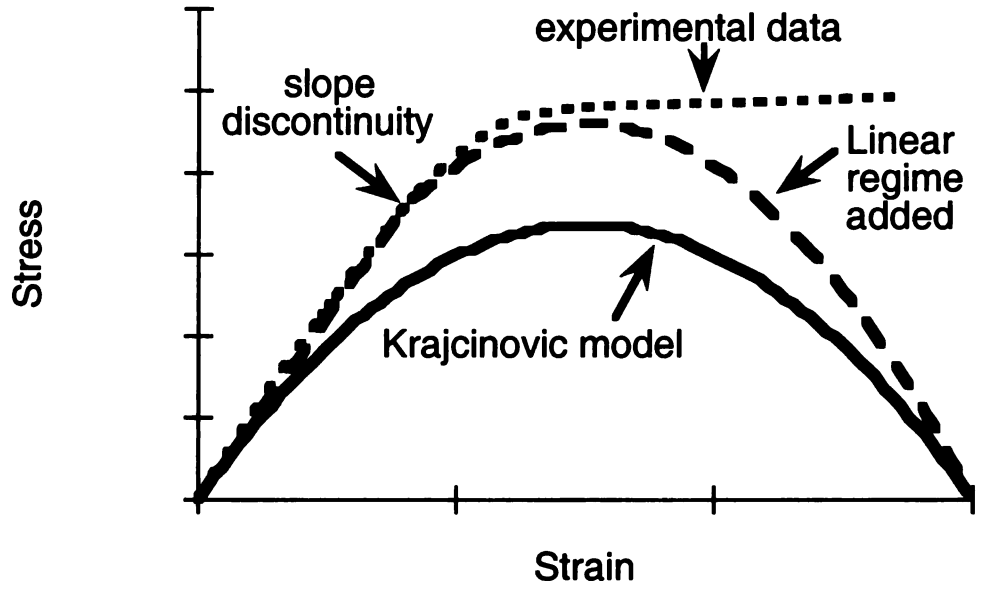

Figure 7.2. Stress-strain response predicted by original model by Krajcinovic, the same model with an initial linear regime added, and experimental data. An initial linear regime was incorporated by changing the lower bound of the osteon failure strain distribution from zero to a positive value. The slope discontinuity is due to the use of a uniform rather than a normal distribution of failure strains. The adjusted model matches the elastic and knee regions of the experimental data well but does not predict the linear post-yield region.

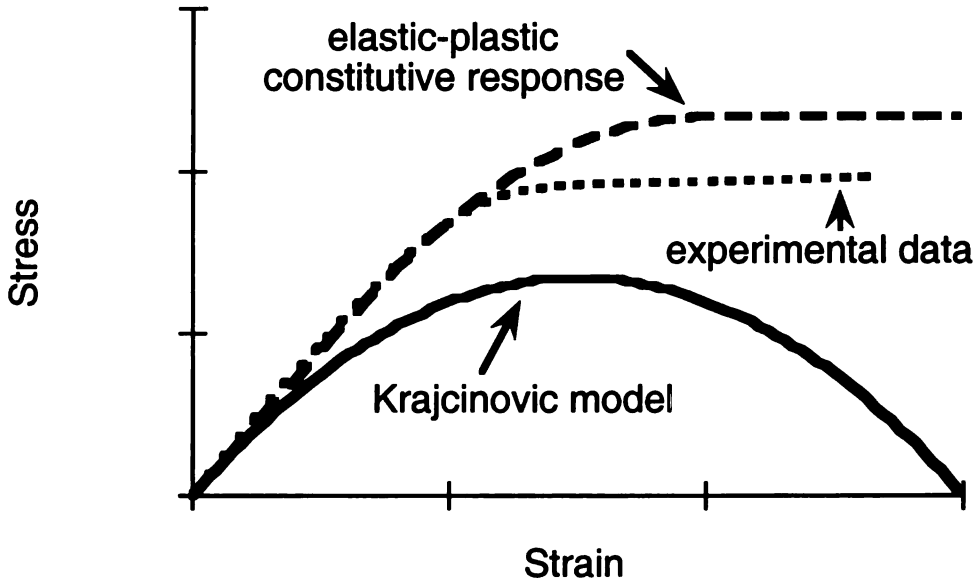

Figure 7.3. Stress-strain response predicted by original model by Krajcinovic and the model with an elastic-plastic constitutive response and a uniform distribution of yield strain assigned to the osteons. The elastic-plastic constitutive response matches the experimental data well.

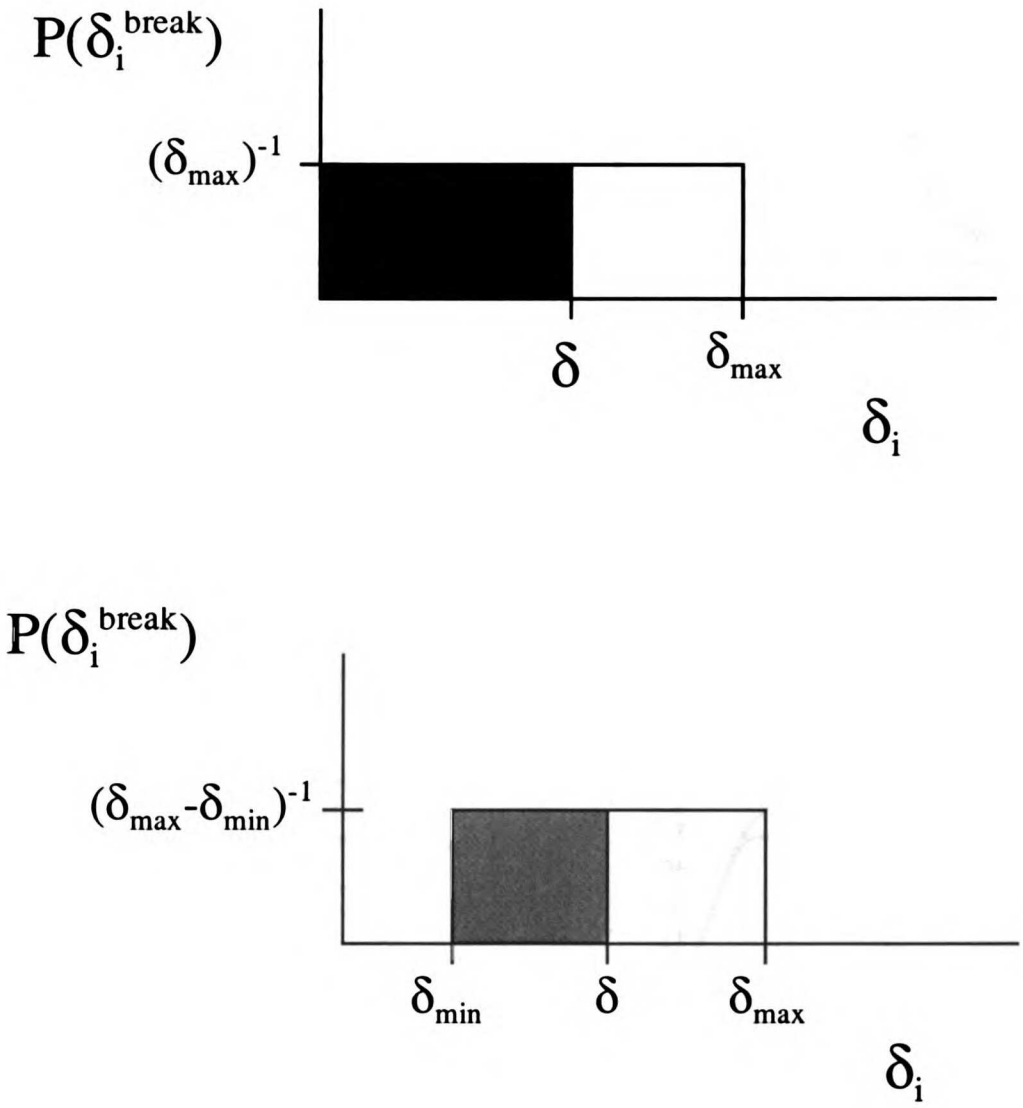

Figure 7.4. Probability density function of the osteon failure displacement for failure displacements from zero to δ_{max} (top) and from δ_{min} to δ_{max} (bottom). The area of each box equals one, by definition. The fraction of damaged osteons, ω, at a given displacement, δ, is given by the shaded area divided by the total area.

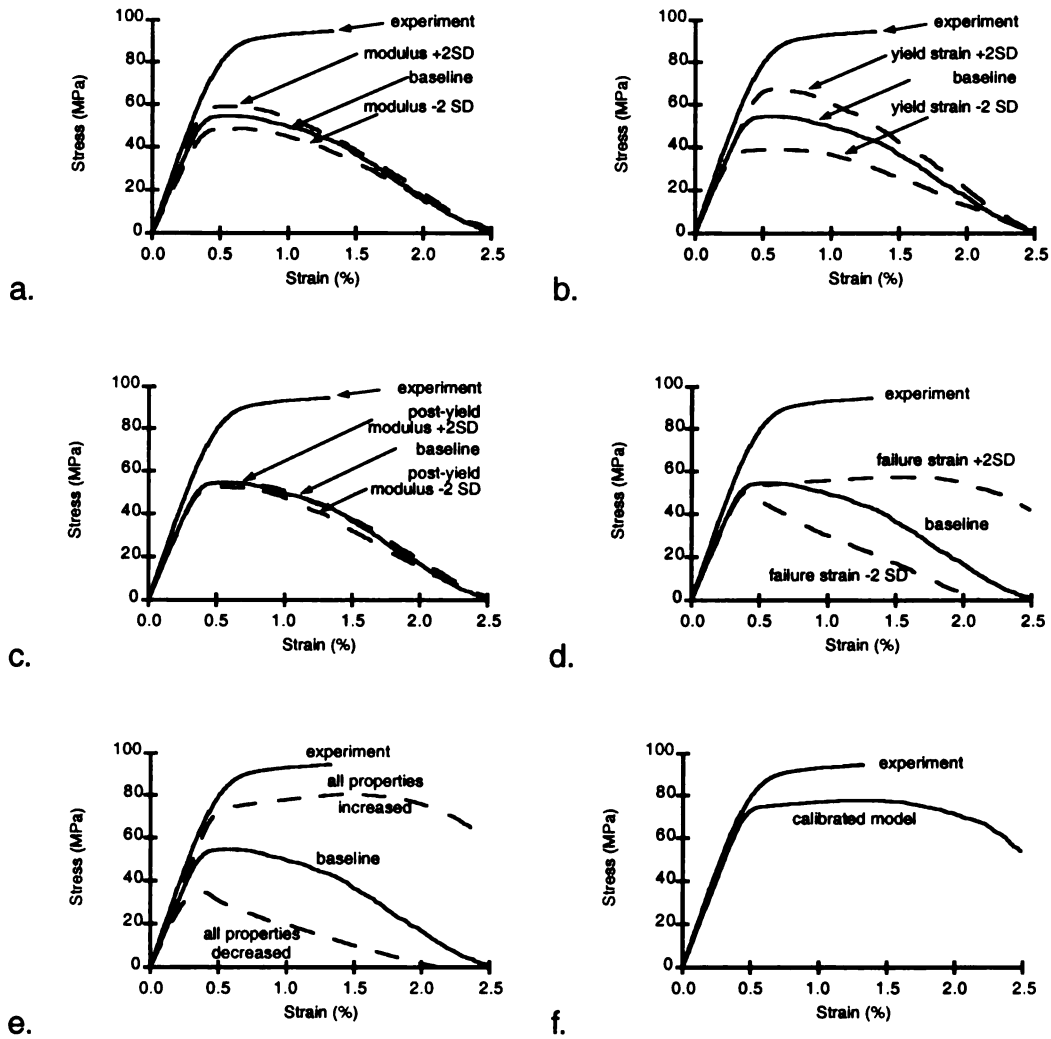

Figure 7.3. Experimentally determined and model predicted stress-strain response from the baseline model and models with increased and decreased mean values of: a) elastic modulus; b) yield strain, c) post-yield modulus, d) failure strain, e) all input parameters, and f) stress-strain response of the calibrated model and experimental results. The calibrated model behaves similarly to cortical bone except that the model predicts a sharper knee in the yield region and does not predict catastrophic failure.

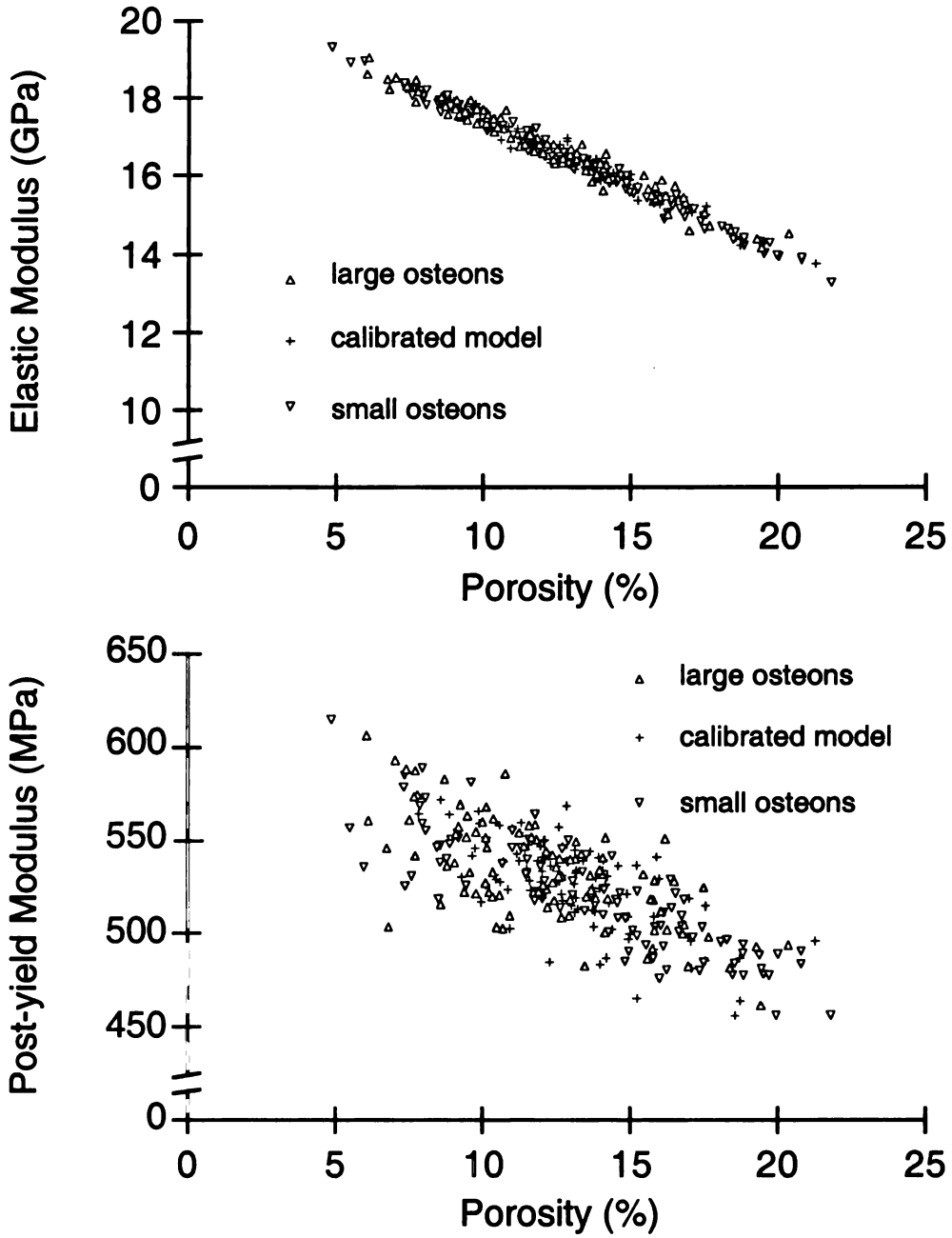

Figure 7.4. Relationship between elastic (top) and post-yield (bottom) modulus and porosity for models with osteon diameters of 200 μm (small osteons), 252 μm (calibrated model), and 300 μm (large osteons). The substantial overlap of the data from the three different models suggests that osteon diameter is not an important parameter in determining the mechanical properties of bone. The Haversian canal diameters are set equal to one-half of the osteon diameters for all cases.

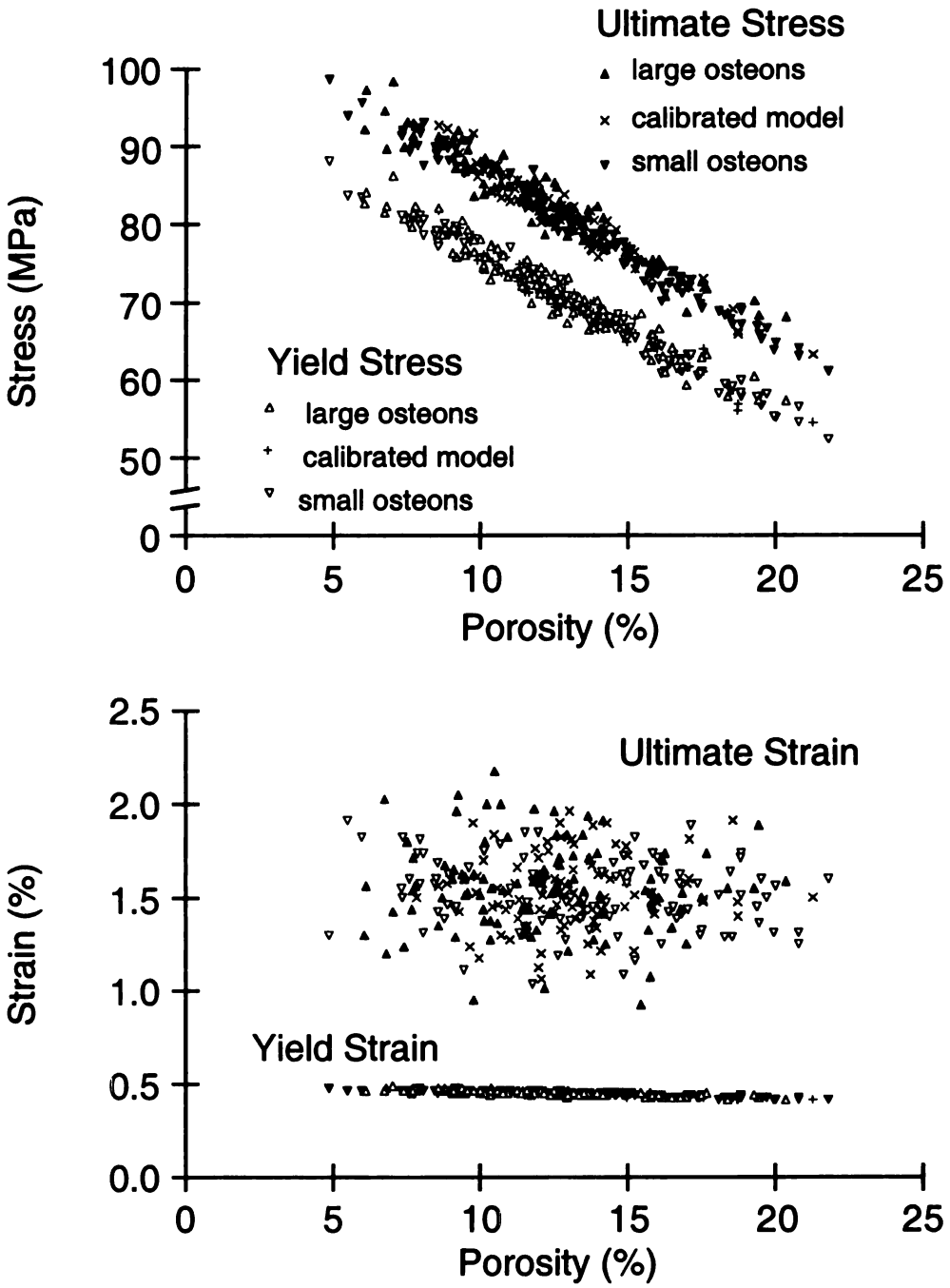

Figure 7.5. Relationship between yield and ultimate stress (top) and strain (bottom) and porosity for models with osteon diameters of 200 μm (small osteons), 252 μm (calibrated model), and 300 μm (large osteons). The substantial overlap of the data from the three different models suggests that osteon diameter is not an important parameter in determining the mechanical properties of bone.

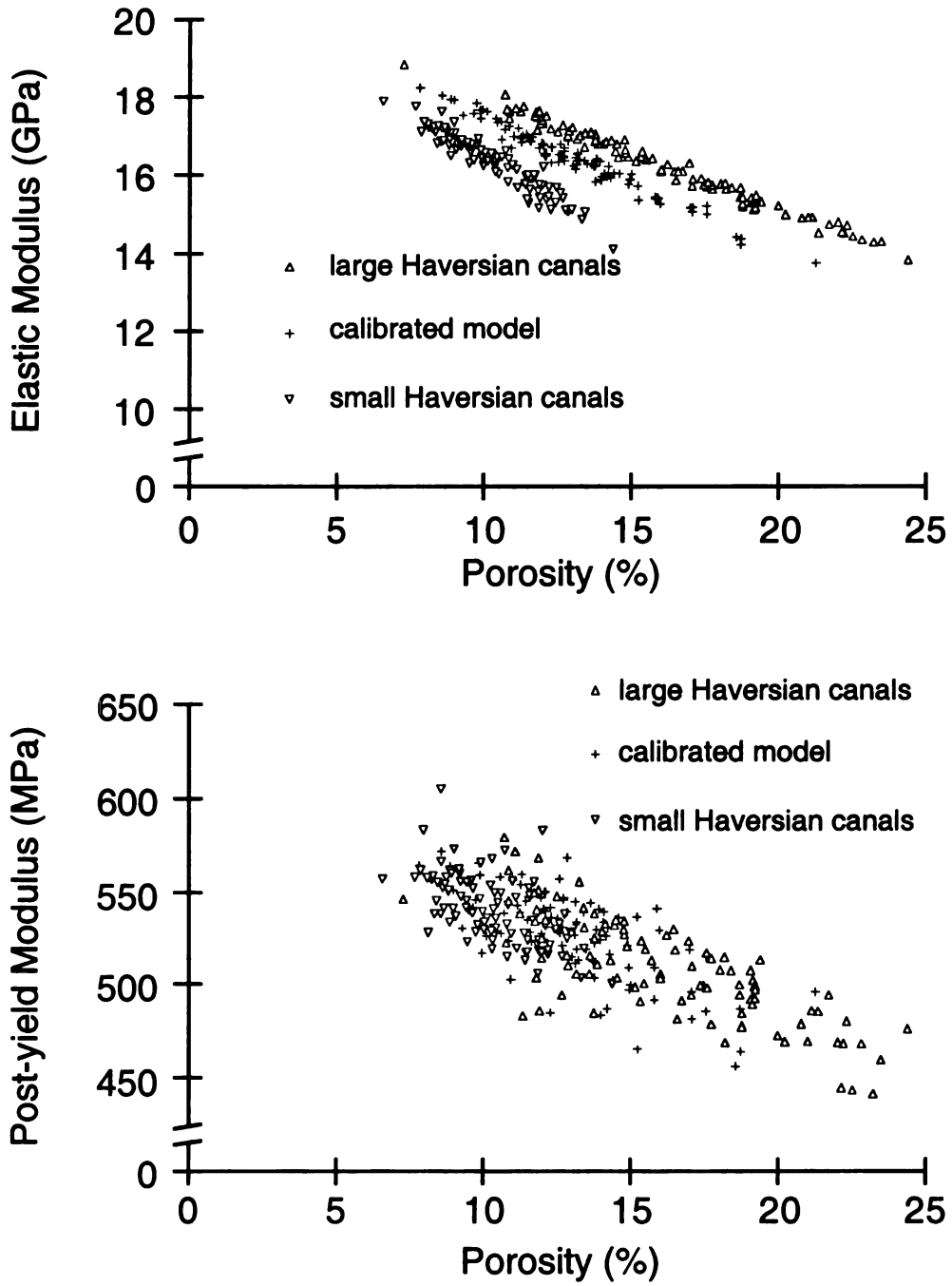

Figure 7.6. Relationship between elastic (top) and post-yield (bottom) modulus and porosity for models with Haversian canal diameters equal to 40% (small Haversian canals), 50% (calibrated model), and 60% (large Haversian canals) of the osteon diameter. Elastic modulus increased with Haversian canal diameter at a fixed porosity. Plastic modulus was not affected by changes in Haversian canal diameter.

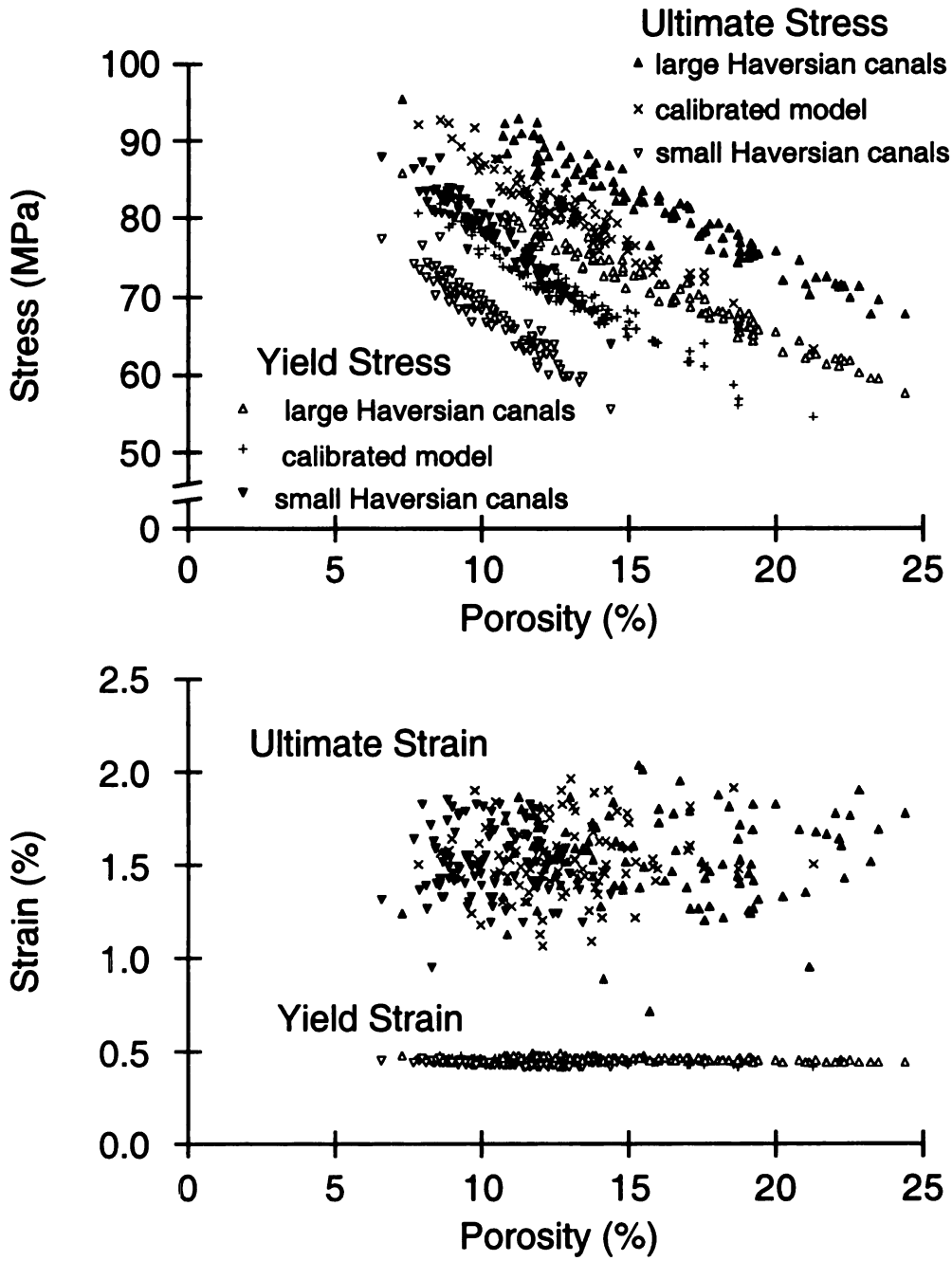

Figure 7.7. Relationship between yield and ultimate stress (top) and strain (bottom) and porosity for models with Haversian canal diameters equal to 40% (small Haversian canals), 50% (calibrated model), and 60% (large Haversian canals) of the osteon diameter. Like elastic modulus, both yield and ultimate stress increased with increasing Haversian canal diameter. Yield and ultimate strains were not affected by changes in Haversian canal diameter.

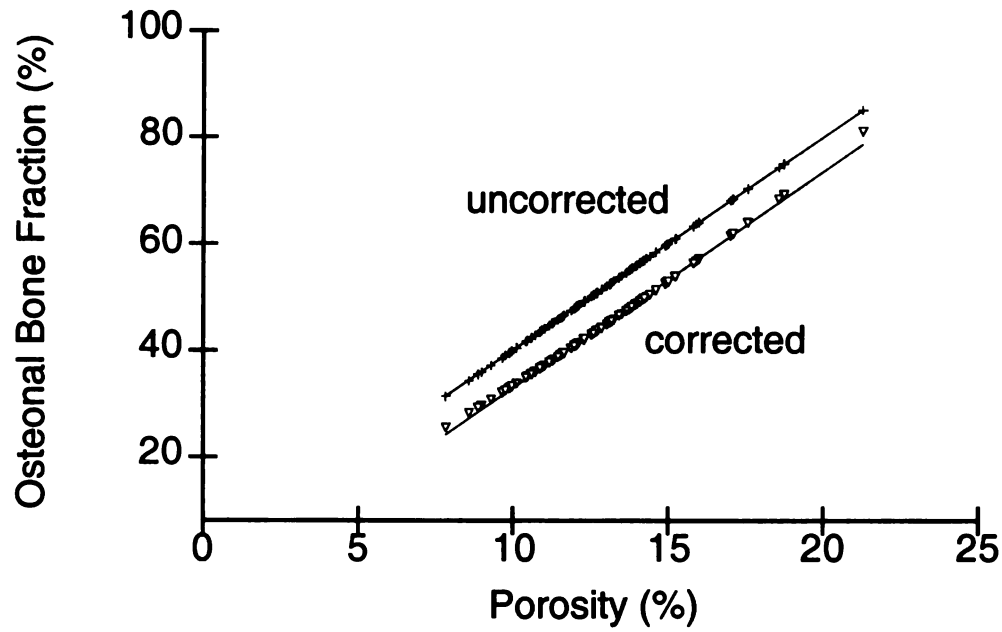

Figure 7.8. Osteonal bone fraction—corrected and uncorrected—vs. porosity of the calibrated model. There was a high correlation ($r^2 > 0.98$) for both regressions indicating that porosity was a sufficient parameter to quantify the microstructure of the model.

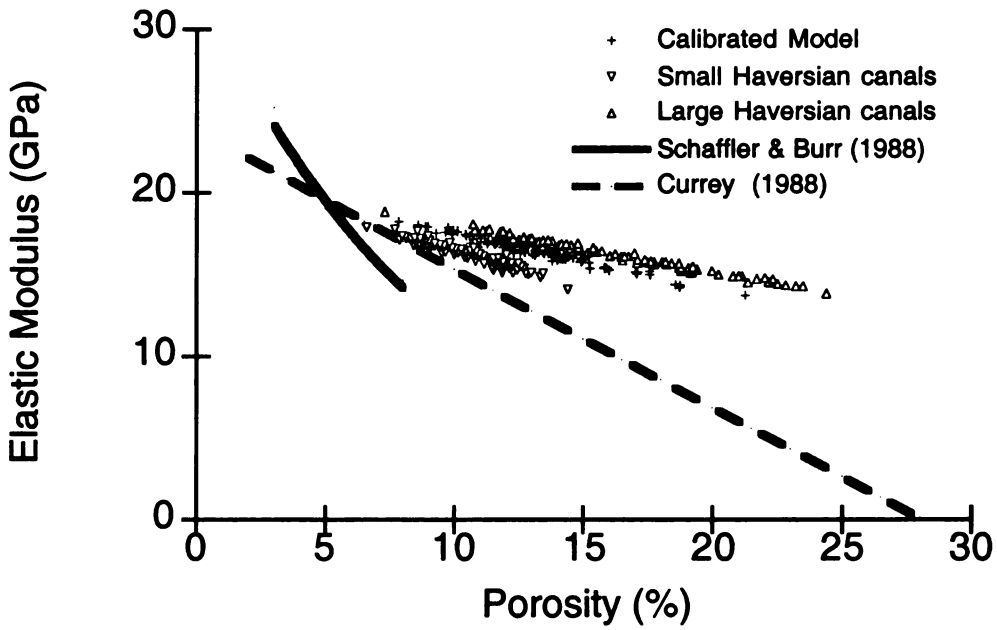

Figure 7.9. Elastic modulus predicted from the calibrated model and models with different Haversian canal sizes and regression lines from Schaffler and Burr (189) and Currey (188). The model agrees reasonably well with the latter regression between 7% and 12% porosity, particularly for the case of the small Haversian canals.

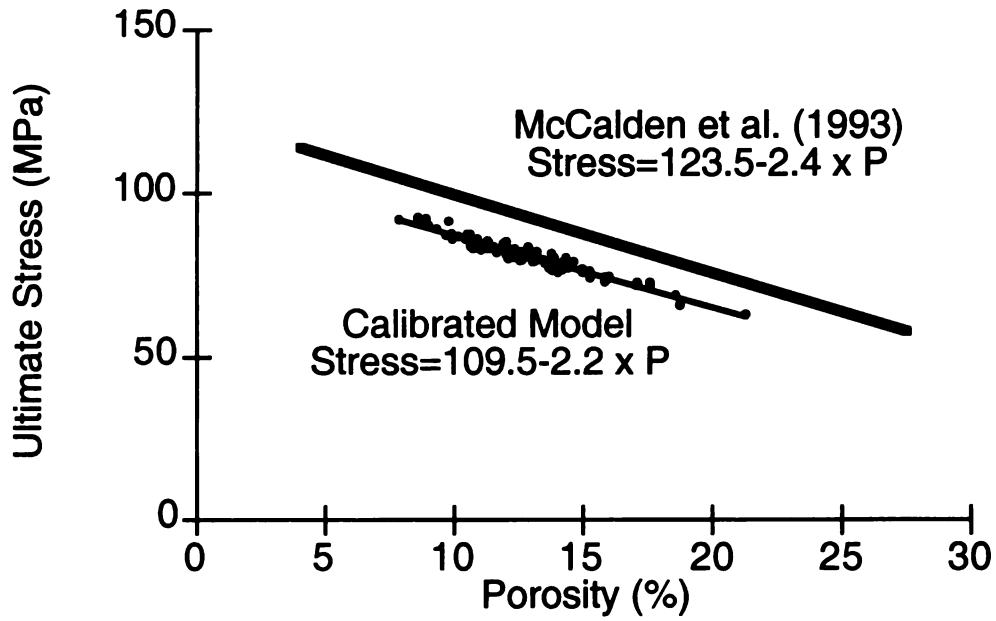

Figure 7.10. Apparent ultimate stress predicted from the calibrated model and the linear regression from McCalden *et al.* (19). The model agrees well with the regression over the porosity range modeled.

Chapter Eight. Conclusions

Summary of major results

The overall goal of this work was to relate changes in the constituent structure of bone to changes in the mechanical properties. A series of experiments were performed on intact, heat-treated and demineralized bovine and human cortical bone. A continuum damage model of cortical bone microstructure was developed and then used to predict the apparent mechanical properties of bone. The following are some of the major results of this dissertation:

1. The elastic modulus of intact and deorganified bone were equivalent, thus the elastic modulus was completely determined by the mineral component of bone. Deorganification substantially reduced the ultimate stress and strain, indicating that collagen played an important role in the failure properties of bone, particularly in tension. The structure of the mineral phase of bone was unaltered by heating to 350° C for two days, suggesting that heat-treated bone may be a viable bone substitute in compressive load-bearing applications, if these results can be extended to include fatigue loading.
2. The mechanical properties of isolated bone collagen were heterogeneous among species and anatomical sites. Thus the choice of species and anatomical site is important when investigating the post-yield properties of isolated collagen and intact bone.
3. The amount of pentosidine cross-linking in human bone collagen increased with age. Ribose treatment caused further increases *in vitro* and significantly altered the mechanical properties of isolated bone collagen. Specifically, the ductility of collagen was reduced in ribose treated samples compared to untreated controls.
4. The pentosidine level in intact bone increased with age, as it did in demineralized bone. The ductility of intact bone was also reduced in ribose treated samples compared to untreated controls. These results suggest that the ductility of bone is determined in large

part by the collagen component and that the age-related decrease in the ductility of bone is caused in part by an increase in pentosidine cross-links in bone collagen.

5. A continuum damage model of bone microstructure was developed. The model was capable of accurately predicting the monotonic stress-strain response, and the role of various microstructural elements in the mechanical properties of bone.

Combined, these results demonstrate that the mechanical properties of cortical bone depend on both ultrastructure—the scale of individual collagen and hydroxyapatite components—and microstructure—the scale of osteons, lamellae and Haversian canals. More specifically, it has been demonstrated that the elastic modulus of bone depends strongly on the elastic modulus of the underlying hydroxyapatite while the ductility depends on the underlying collagen.

These results were first hypothesized by Burstein *et al.* (156) more than 20 years ago, and have now been demonstrated experimentally. Furthermore, it is clear from the experimental results that neither collagen nor hydroxyapatite exhibits stress-strain behavior similar to intact bone, specifically the non-linear knee and strain-hardening post-yield region are absent from both constituents. Thus the knee and post-yield regions must result from the collagen-hydroxyapatite interface, or the structure at a higher composite level. Since elastically deforming osteons were not capable of reproducing the stress-strain curve of bone in the continuum damage model (elastic-plastic osteon deformation was required), the collagen-hydroxyapatite interface must be responsible for the non-linear behavior observed in bone. Thus a primary area of future work should be understanding this interface—its structure and mechanical properties. A complete understanding of the structure-function relationship of bone tissue requires knowledge of the hierarchical composite structure of bone and how the various hierarchical levels affect mechanical properties.

Recommendations for future research

The results from this dissertation suggest further research in three broad areas: experiments on cortical bone, experiments on trabecular bone, and theoretical modeling of bone tissue.

The first suggested area of future research is additional experiments on cortical bone tissue. These experiments have the long-term goal of understanding the relationship between collagen and hydroxyapatite and how they determine the mechanical properties of bone tissue. Specific experiments that should be performed include:

- Determining the composition, structure, and mechanical properties of the collagen-hydroxyapatite interface (*i.e.* the organic material that remained after the heat treatment described in Chapter 3). The results of this dissertation suggest that this interface is the key element in changing the stress-strain behavior of collagen and hydroxyapatite—neither of which exhibits post-yield deformation—to the stress-strain behavior of bone—which does exhibit post-yield deformation.
- Determining the age- and disease-related variation in pentosidine cross-linking and the ductility of cortical bone. The results here demonstrated that increasing pentosidine cross-linking *in vitro* reduces the ductility of bone, but these results must be confirmed for *in vivo* changes in cross-linking.
- Measuring the monotonic mechanical properties of isolated crystals of hydroxyapatite and collagen fibers. While the need for this information is obvious, the experiments required are difficult. An alternative approach is to measure the mechanical properties of a mineralized collagen fibril and determine the mechanical properties of collagen and hydroxyapatite by creating a model of the fibril and solving the inverse problem. Possible models include a continuum damage model, similar to that described in Chapter 7, and a shear lag model.

Additional experiments on cortical bone should be done to provide improved input parameters for the theoretical model described in Chapter 7. These include:

- Measuring the monotonic mechanical properties of isolated osteons and fragments of interstitial bone. Results from this experiment could be used to verify the mechanical properties used in the theoretical model.
- Measuring the mechanical properties of the cement line, that is, the force-displacement relationship for an osteon being pushed out of the surrounding interstitial bone. This information is necessary in order to expand the theoretical model to include the cement line as a microstructural element.

The second area of future work is experiments on trabecular bone. The most common sites for age- and disease-related bone injuries are comprised of trabecular bone. Therefore, the now-established relationship between collagen cross-linking and the mechanical properties of cortical bone should be extended to trabecular bone specimens and then, whole vertebral bodies. Once the role of cross-linking is understood for trabecular bone, new assays of bone quality and new drug treatments that maintain or improve the ductility of bone may be possible.

The third area of future work is theoretical modeling of bone tissue. Specifically, the continuum damage model described in Chapter 7 should be expanded to include additional microstructural features like cement lines, porosity in the interstitial bone and individual lamellae. Similar models, with a smaller size scale, should then be developed to understand the interactions between collagen and hydroxyapatite, and the role of ultrastructural parameters like collagen cross-linking and hydroxyapatite crystal size and orientation. Models of collagen, hydroxyapatite and their interface are particularly important, as they may aid in determining the mechanical properties of these elements by solving the inverse problem.

Research in these three areas shares a common goal of improving our understanding of how the composite structure of bone affects its mechanical properties.

While each of these areas of research is independent, it is important to consider results from all three areas *in toto*, as this will provide the most insight into the structure-function relationship of bone.

Appendix A. Using the load frame LVDT to measure strain in demineralized cortical bone specimens

A soft-tissue extensometer[1] was used to measure strain directly from demineralized bone specimens in the experiments described in Chapter 4 and Chapter 5. The soft-tissue extensometer was accurate when compared to a traditional clip-on style extensometer while both were attached to a plastic sample, but the soft-tissue extensometer separated from some of the demineralized bone specimens during tension tests. The displacement measured from the load frame LVDT was therefore used in addition to the soft-tissue extensometer in order to calculate strain in the demineralized bone specimens. This appendix describes the procedure used to calculate strain using the soft-tissue extensometer and the load frame LVDT.

Displacement was recorded for each mechanical test using the soft-tissue extensometer and the load frame LVDT. Extensometer is a misnomer, as it actually measured displacement and not strain. Extensometer-measured strain was calculated by dividing the displacement data by the gage length of 5 mm. After recording load-displacement data (Figure A.1), the displacement measured with the LVDT was scaled to match the displacement measured with the soft-tissue extensometer (Figure A.2) using the equation:

$$\delta_i^{LVDT-adjusted} = \frac{\overline{\delta^{extensometer}}}{\overline{\delta^{LVDT}}} \delta_i^{LVDT} \qquad (1)$$

where $\delta_i^{LVDT-adjusted}$ is the i^{th} adjusted LVDT-measured displacement value, $\overline{\delta^{extensometer}}$ and $\overline{\delta^{LVDT}}$ are the average extensometer- and LVDT-measured displacements in the region that the extensometer was attached to the specimen, respectively, and δ_i^{LVDT} is the i^{th} original (unadjusted) LVDT-measured displacement value. After scaling the LVDT displacement data, strain was calculated by dividing the scaled data by the *gage length* of the soft-tissue extensometer (5 mm), that is:

[1] Model 632.29c-30, MTS Corp., Eden Prarie, MN.

$$\varepsilon_i^{LVDT} = \frac{\delta_i^{LVDT-adjusted}}{gage\ length} \tag{2}$$

where ε_i^{LVDT} is the strain calculated from the LVDT-measured displacement data. Stress-strain curves were then plotted using the strain calculated from the load frame LVDT (Figure A.3).

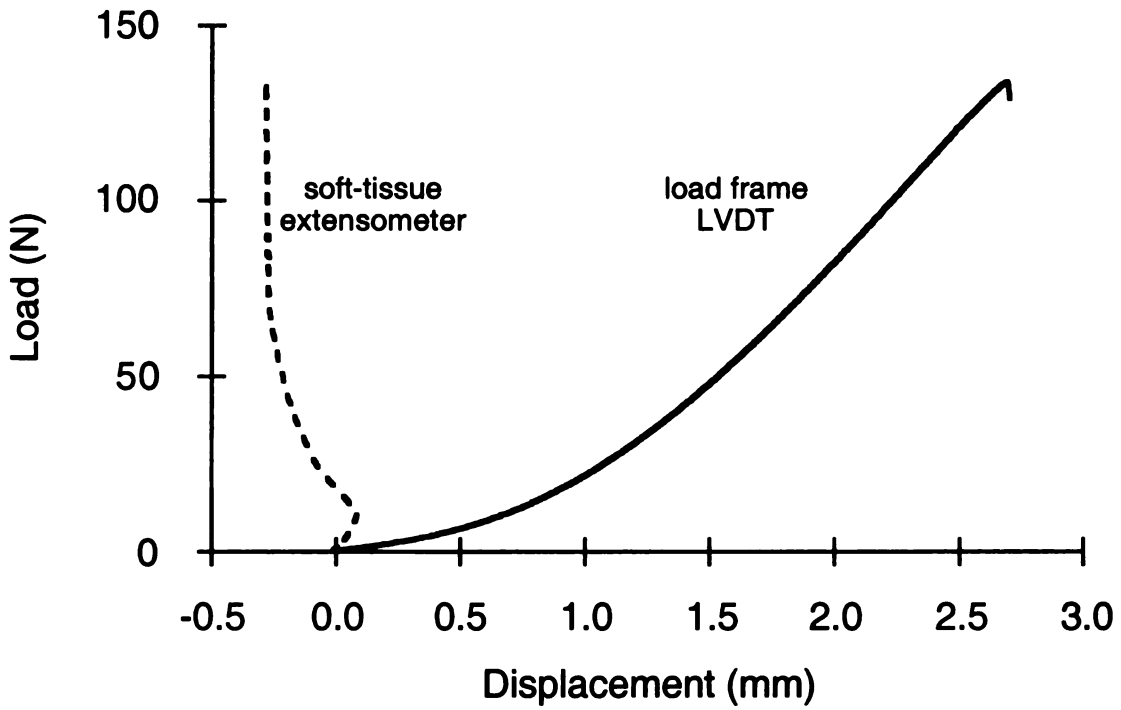

Figure A.1. Typical load displacement plot for demineralized cortical bone specimen. The extensometer was accurate initially, but separated from the specimen. The displacement data measured from the load frame LVDT was scaled to match the initial soft-tissue extensometer data. Note that the two devices measured displacement over different gage lengths: 5 mm for the soft-tissue extensometer and approximately 20 mm for the load frame LVDT.

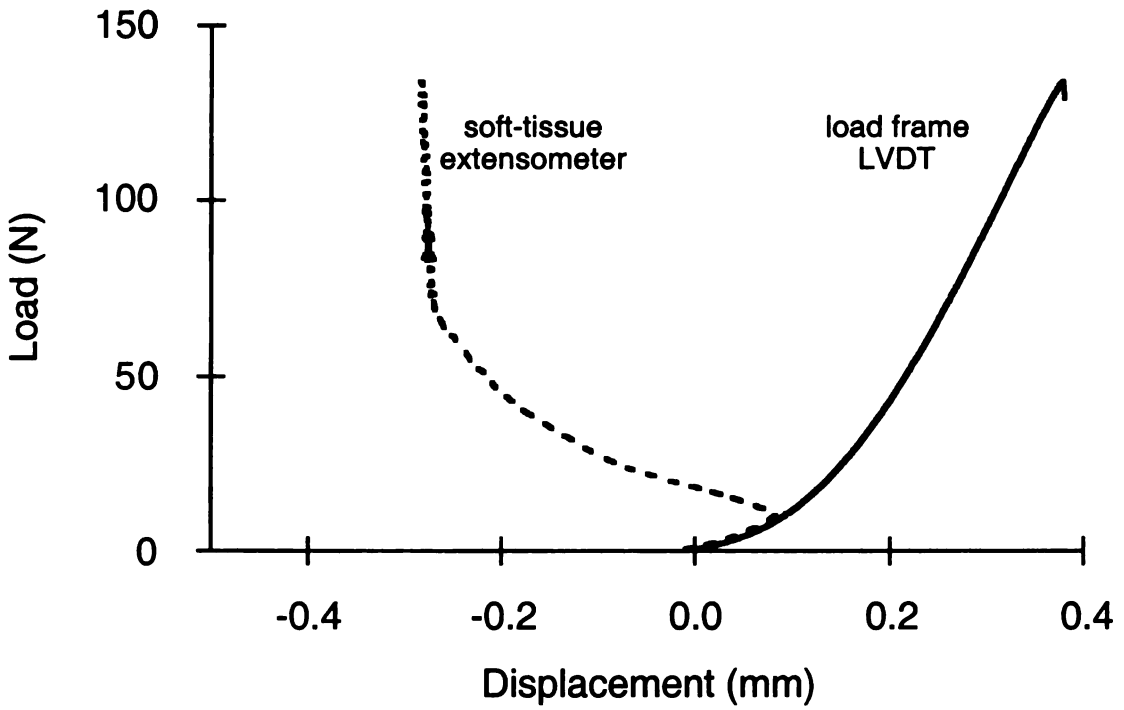

Figure A.2. Load-displacement plot with the displacement measured from the load frame LVDT scaled to match the soft-tissue extensometer data. This changes the effective gage length of the load frame LVDT data to 5 mm.

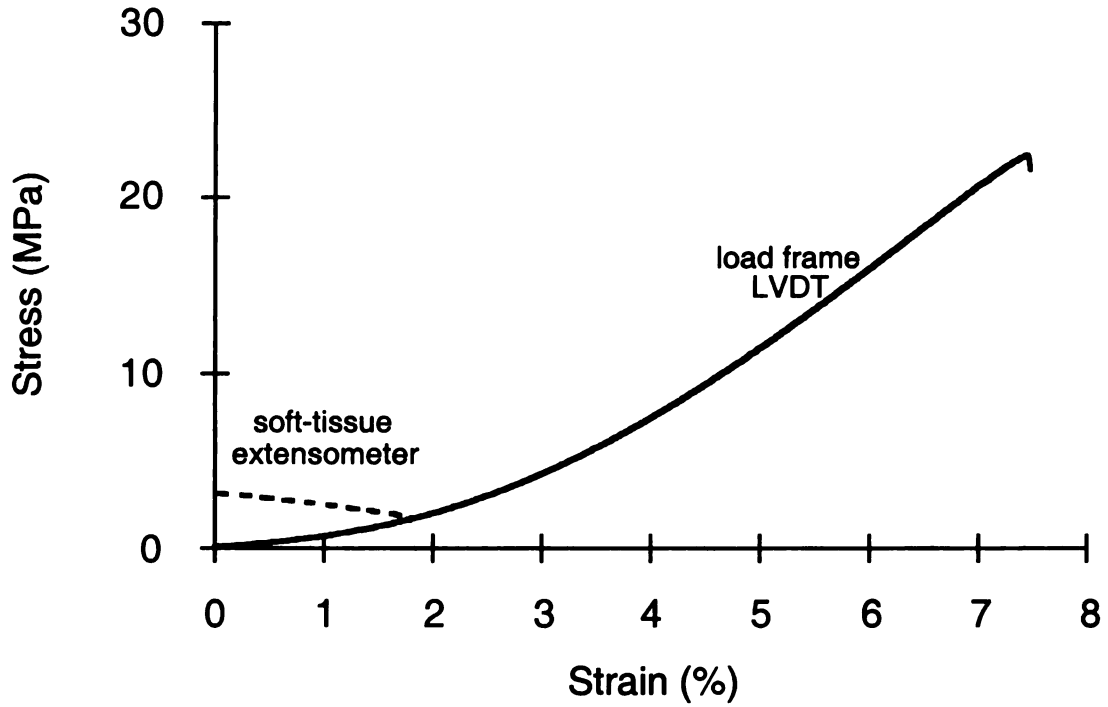

Figure A.3. Typical stress-strain curve using adjusted load frame LVDT displacement data to calculate strain. Note the good agreement between the two strain measuring techniques from 0 to about 2% strain.

Appendix B. Age related variation in the mechanical properties of demineralized and intact bone

Introduction

The aim of this appendix is to describe the age-related variation in the mechanical properties of demineralized and intact human cortical bone. The comparison between untreated and ribose-treated samples of demineralized and intact human femoral bone demonstrated that artificially increasing pentosidine levels decreased the ductility of both materials (Chapters 5 and 6, respectively). But the role of natural, age-related increases in pentosidine level has not been determined. The data presented here are taken from the control groups of the experiments described in Chapter s 5 and 6.

Methods

The specimen preparation, mechanical testing and data reduction were described in detail previously (Chapters 4-6). Briefly, for the demineralized bone: 10 specimens of demineralized human femoral cortical bone (from 10 cadavers aged 49 to 84 years; mean ± SD of 69 ± 14 years) were tested to failure in tension at approximately 0.3%/second; and for the intact bone: 12 specimens of human femoral cortical bone (from 12 cadavers aged 49 to 85 years; mean ± SD of 68 ± 13 years) were tested to failure in tension at approximately 0.1%/second. Mechanical properties were plotted against age and regression analysis was performed to determine age-related changes in mechanical properties.

Results

In the demineralized bone, elastic modulus and ultimate stress decreased with age by approximately 50 MPa and 25 MPa per decade of life, respectively ($r^2 = 0.54$ and $p < 0.02$ for both regressions; Figures B.1 and B.2). Strain-to-failure was not correlated with age in the 35 year age range investigated ($p = 0.33$; Figure B.3). Summary statistics for all mechanical properties for demineralized bone were reported previously (Chapter 5) and are repeated here for convenience (Table B.1).

For the intact bone, no significant correlations were observed between any mechanical property (elastic modulus, yield stress and strain, ultimate stress, strain-to-failure and post-yield strain) and age in the 36 year age range investigated ($r^2 < 0.16$; $p > 0.20$ for all regressions; Figures B.4-B.6). Converting the abscissa to a logarithmic scale did not result in significant regressions. Thus, all mechanical properties can be described by a mean and standard deviation (Table B.2).

Discussion

The absence of any linear relationships between mechanical properties and age is surprising but can be explained quite simply. The age-related variation in the mechanical properties of bone are widely reported (10, 17, 19, 23, 190-194). The most probable reasons for the lack of mechanical property-age correlations here is the small size of the data set and the short age range spanned by the set. Most investigators who have measured age-related variations have examined more than 100 specimens (*e.g.* 178 femoral specimens from 33 cadavers (23) and 235 femoral specimens from 47 cadavers (19)) that span a larger age range (*e.g.* 21-86 years (23) and 20-102 years (19)) than that included here. In the earlier study, in which mechanical properties are listed by decade of the donor at the time of death, elastic modulus, yield stress and ultimate stress do not vary between ages 50 and 79, but rather, the downward trend is observed only when the younger (20-50) and oldest (80-89) age groups are included in the comparison(23). Thus, had these authors been limited to the age range included in this study (49-84 years) they would not have been able to demonstrate the age-related variations in the mechanical properties of bone. Additionally, a more recent study, reported no significant relationship between elastic modulus and age (19) suggesting that the very small decrease reported previously (-1.5% per decade of life; (23)) was erroneous. The results for elastic modulus reported here therefore agree with previous findings. The lack of a relationship between other mechanical properties and age in this data set is thus due to low sample size and statistical power.

Table B.1. Mechanical properties of demineralized human femoral cortical bone from 10 cadavers aged 49 to 84 years.

Mechanical Property	Value
Elastic Modulus (MPa)	277 ± 92 (184-475)
Ultimate Stress (MPa)	14.0 ± 4.6 (8.7-22.4)
Strain-to-failure (%)	8.1 ± 1.3 (6.4-10.1)

All values are mean ± SD (range).

Table B.2. Mechanical properties of intact human femoral cortical bone from 12 cadavers aged 49 to 85 years.

Mechanical Property	Value
Elastic Modulus (GPa)	17.7 ± 1.5 (14.6-19.4)
Yield Stress (MPa)	66.8 ± 7.7 (49.8-75.8)
Yield Strain (%)	0.41 ± 0.03 (0.35-0.44)
Ultimate Stress (MPa)	95.0 ± 5.6 (86.0-102.9)
Strain-to-failure (%)	1.63 ± 0.54 (0.96-2.5)
Post-Yield Strain (%)	1.23 ± 0.54 (0.56-2.2)

All values are mean ± SD (range).

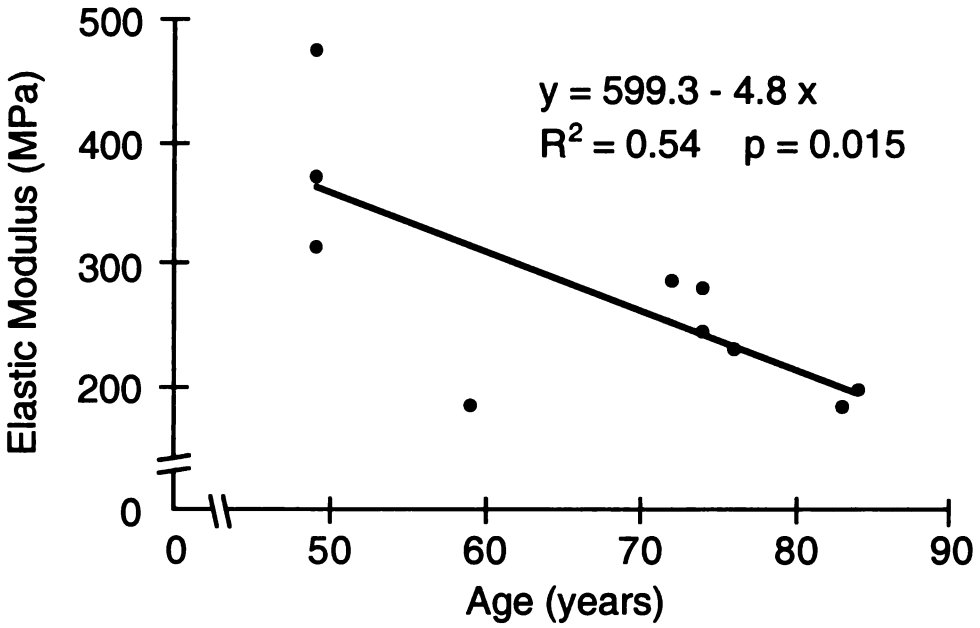

Figure B.1. Elastic modulus of demineralized human femoral cortical bone vs. age. Elastic modulus decreased by nearly 50 MPa per decade of life.

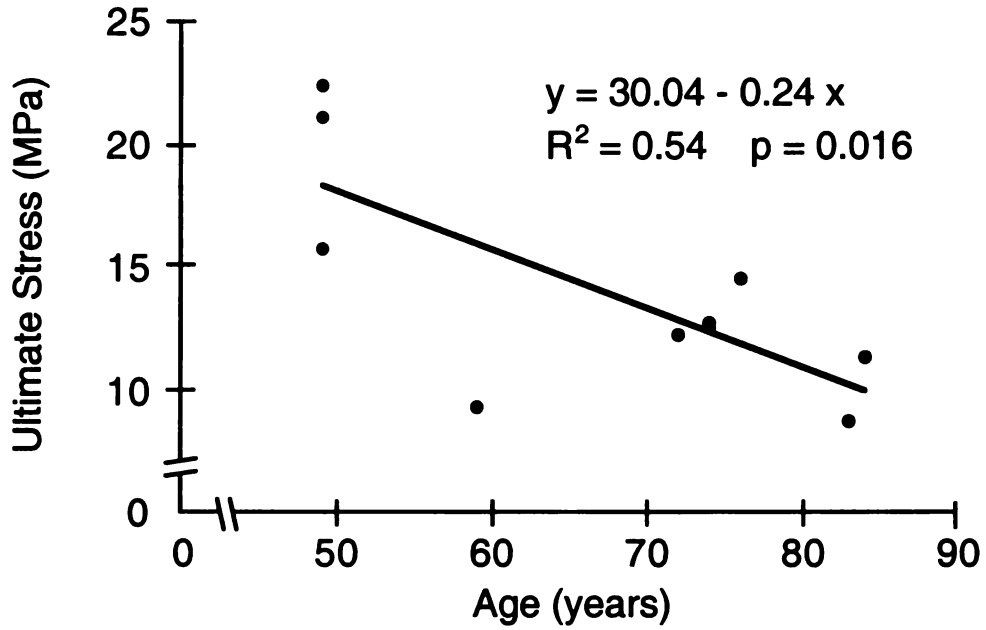

Figure B.2. Ultimate stress of demineralized human femoral cortical bone vs. age. Ultimate stress decreased at a rate of 24 MPa per decade of life.

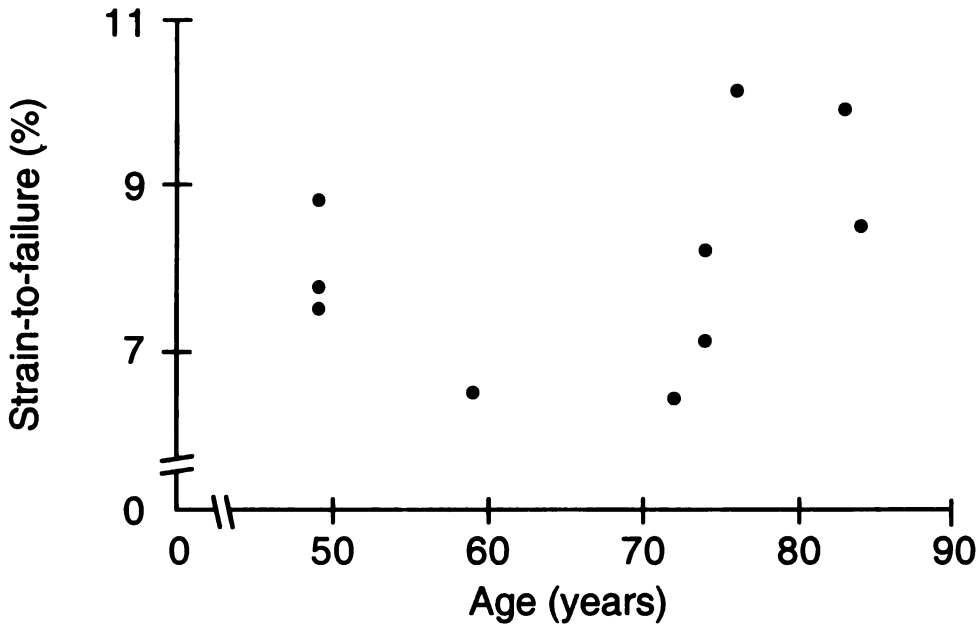

Figure B.3. Strain-to-failure of demineralized human femoral cortical bone vs. age. The average value was 8.1% and did not change significantly with age ($p = 0.33$).

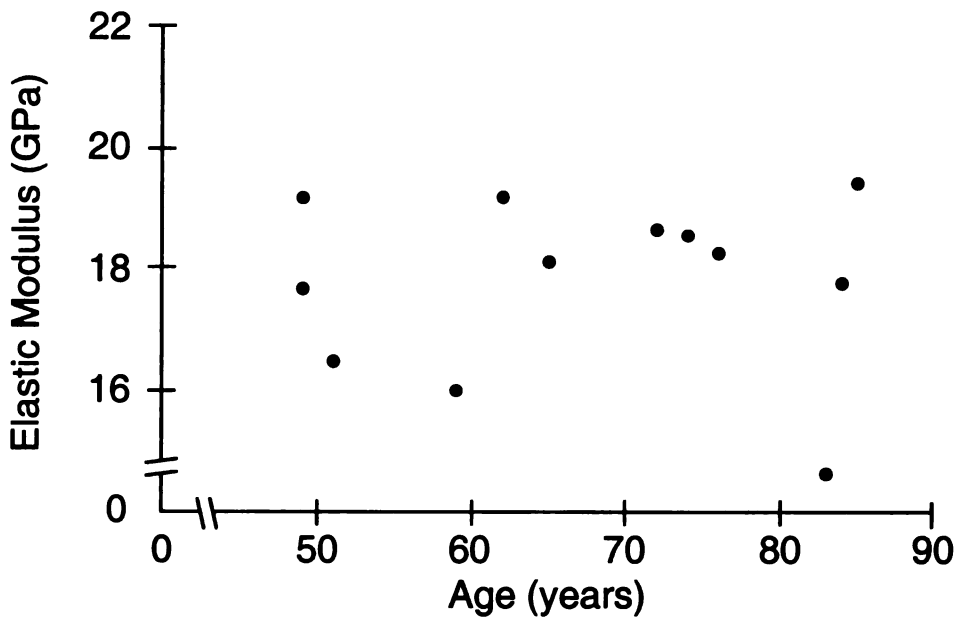

Figure B.4. Elastic modulus of intact human femoral cortical bone vs. age. The average elastic modulus was 17.7 GPa, and did not change significantly with age.

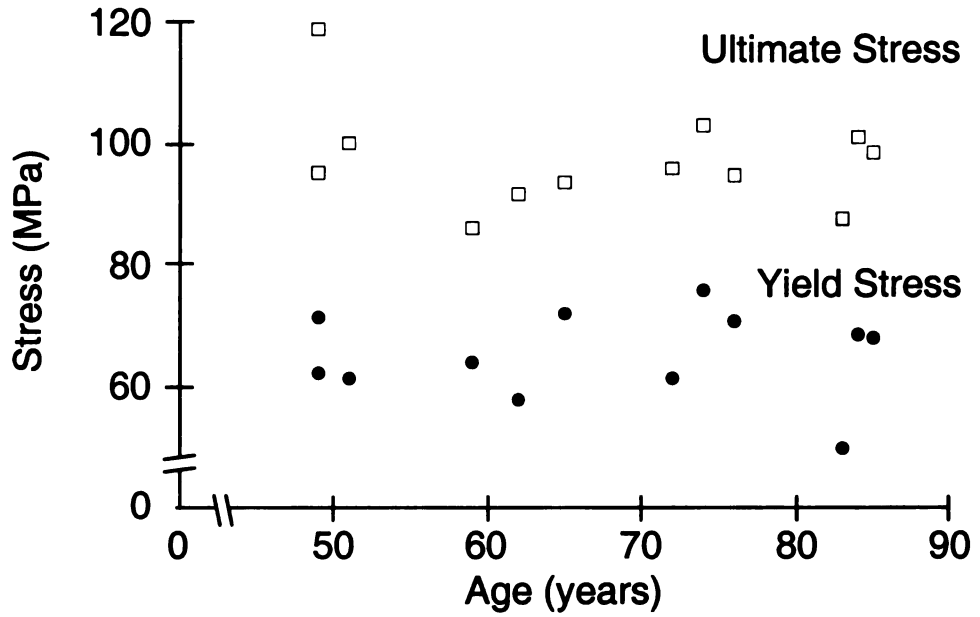

Figure B.5. Yield and ultimate stress of human femoral cortical bone vs. age. The average values were 66.8 MPa and 95 MPa respectively. Neither parameter changed significantly with age ($p = 0.99$ and $p = 0.42$, respectively).

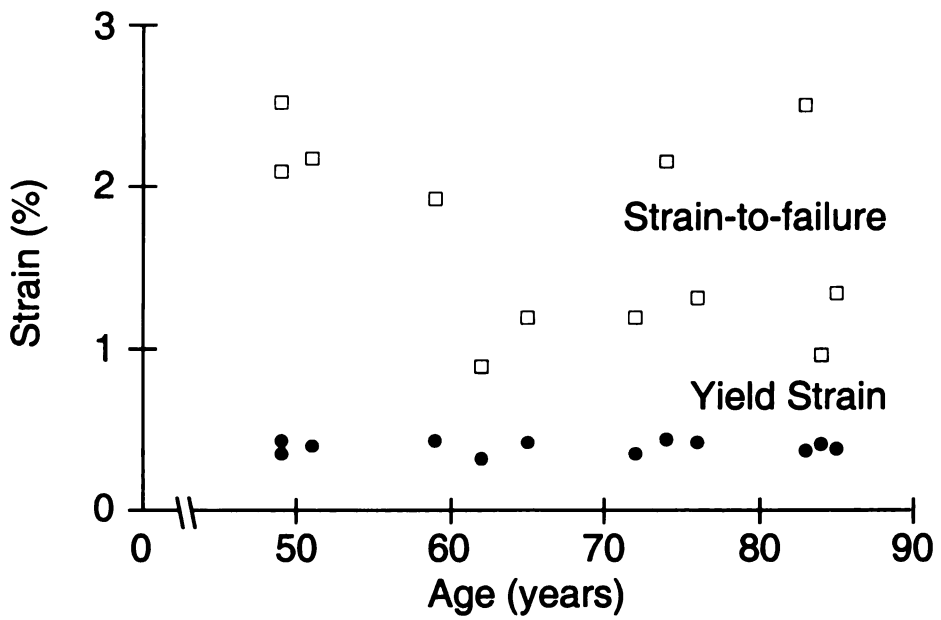

Figure B.6. Yield strain and strain-to-failure of human femoral cortical bone vs. age. The average values were 0.41% and 1.63% respectively. Neither parameter changed significantly with age ($p = 0.95$ and $p = 0.20$, respectively).

Appendix C. Variation in the mechanical properties of demineralized and intact bone associated with pentosidine cross-linking

Introduction

The aim of this appendix is to describe how non-enzymatic pentosidine cross-linking affects the mechanical properties of demineralized and intact human cortical bone. The data presented here are taken from the control groups of the experiments described in Chapter s 5 and 6. It has been demonstrated that increasing pentosidine levels *in vitro* alters the mechanical properties, specifically the ductility, of both demineralized and intact bone. While the relative *in vitro* increases in the pentosidine level of intact bone was approximately the same as the *in vivo* age-related increase, the average age of the cadavers used was high (68 years) and thus the absolute change was much larger than can be expected *in vivo*. The next step in demonstrating the role of non-enzymatic cross-linking in the mechanical properties of bone is to determine how pentosidine levels within the *in vivo* range affect the mechanical properties of bone. Towards this end, regression analysis was used to quantify how mechanical properties change with *in vivo* pentosidine levels in demineralized and intact human cortical bone.

Methods

The specimen preparation, mechanical testing and data reduction were described in detail previously (Chapters 4-6). Briefly, for the demineralized bone: 10 specimens of demineralized human femoral cortical bone (from 10 cadavers aged 49 to 84 years; mean ± SD of 69 ± 14 years) were tested to failure in tension at approximately 0.3%/second; and for the intact bone: 12 specimens of human femoral cortical bone (from 12 cadavers aged 49 to 85 years; mean ± SD of 68 ± 13 years) were tested to failure in tension at approximately 0.1%/second. The amount of pentosidine cross-linking was measured using HPLC. Regression analysis was used to determine the relationship between mechanical properties and pentosidine level.

Results

For the demineralized bone, both elastic modulus and ultimate stress decreased with increasing pentosidine level ($r^2 = 0.64$; $p = 0.005$ for elastic modulus; Figure C.1; $r^2 = 0.55$; $p = 0.013$ for ultimate stress; Figure C.2). Surprisingly, strain-to-failure did not depend on pentosidine level (Figure C.3) even though it did decrease with *in vitro* increases in pentosidine cross-linking (Chapter 5).

For the intact bone, no significant correlations were observed between any mechanical property (elastic modulus, yield stress and strain, ultimate stress, strain-to-failure and post-yield strain) and age in the 36 year age range investigated ($r^2 < 0.16$; $p \geq 0.20$ for all regressions; Figures C.1-C.3).

Discussion

Since age and pentosidine level were correlated (Figures 5.1 and 6.1) the discussion for this appendix is included in Chapters 5 and 6 and Appendix B.

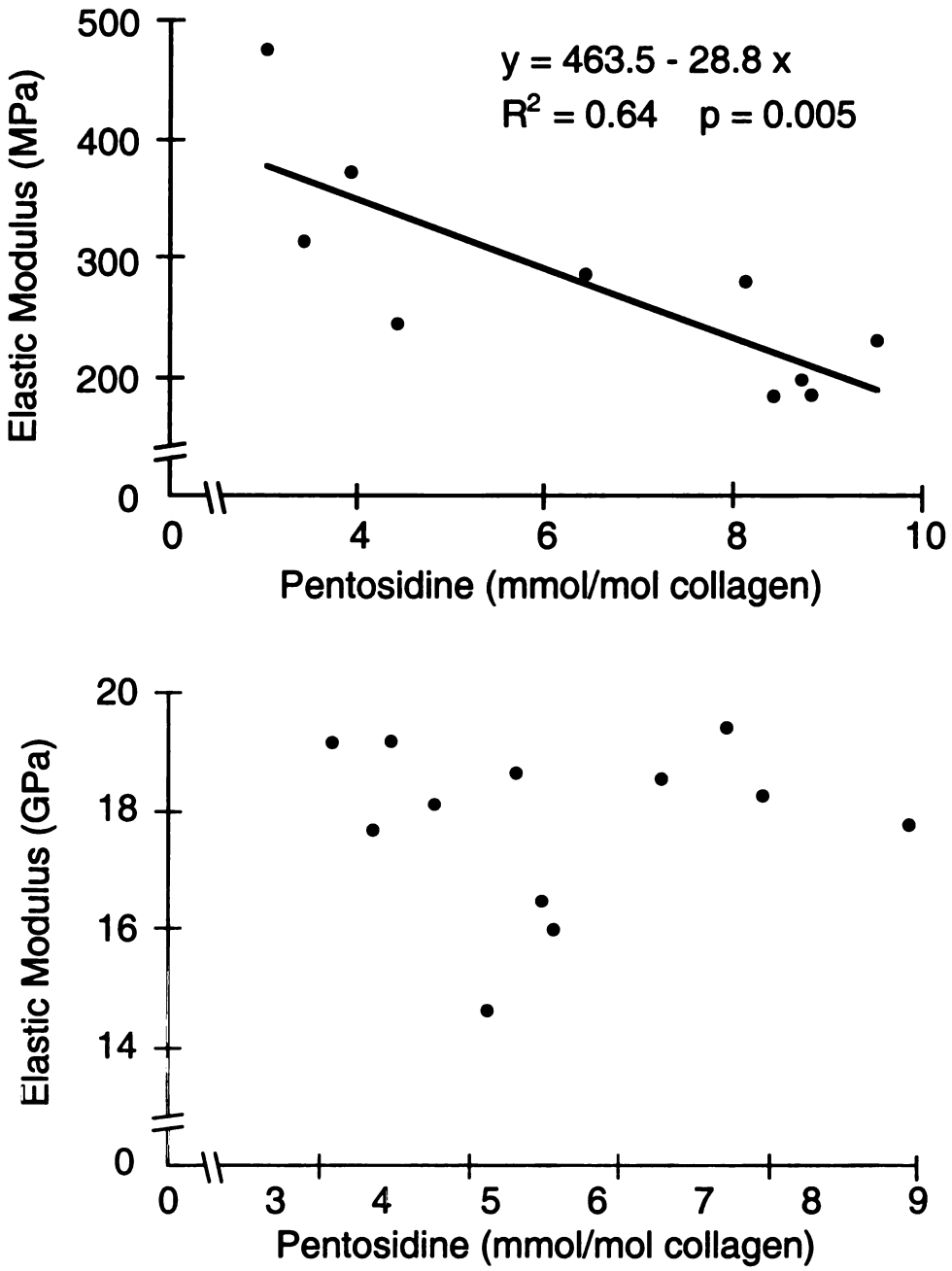

Figure C.1. Elastic modulus of demineralized (top) and intact (bottom) human femoral cortical bone vs. pentosidine level. For the demineralized bone, elastic modulus decreased with increasing pentosidine cross-link density ($p = 0.005$). For the intact bone, the average elastic modulus was 17.7 GPa, and did not change significantly with age ($p = 0.92$).

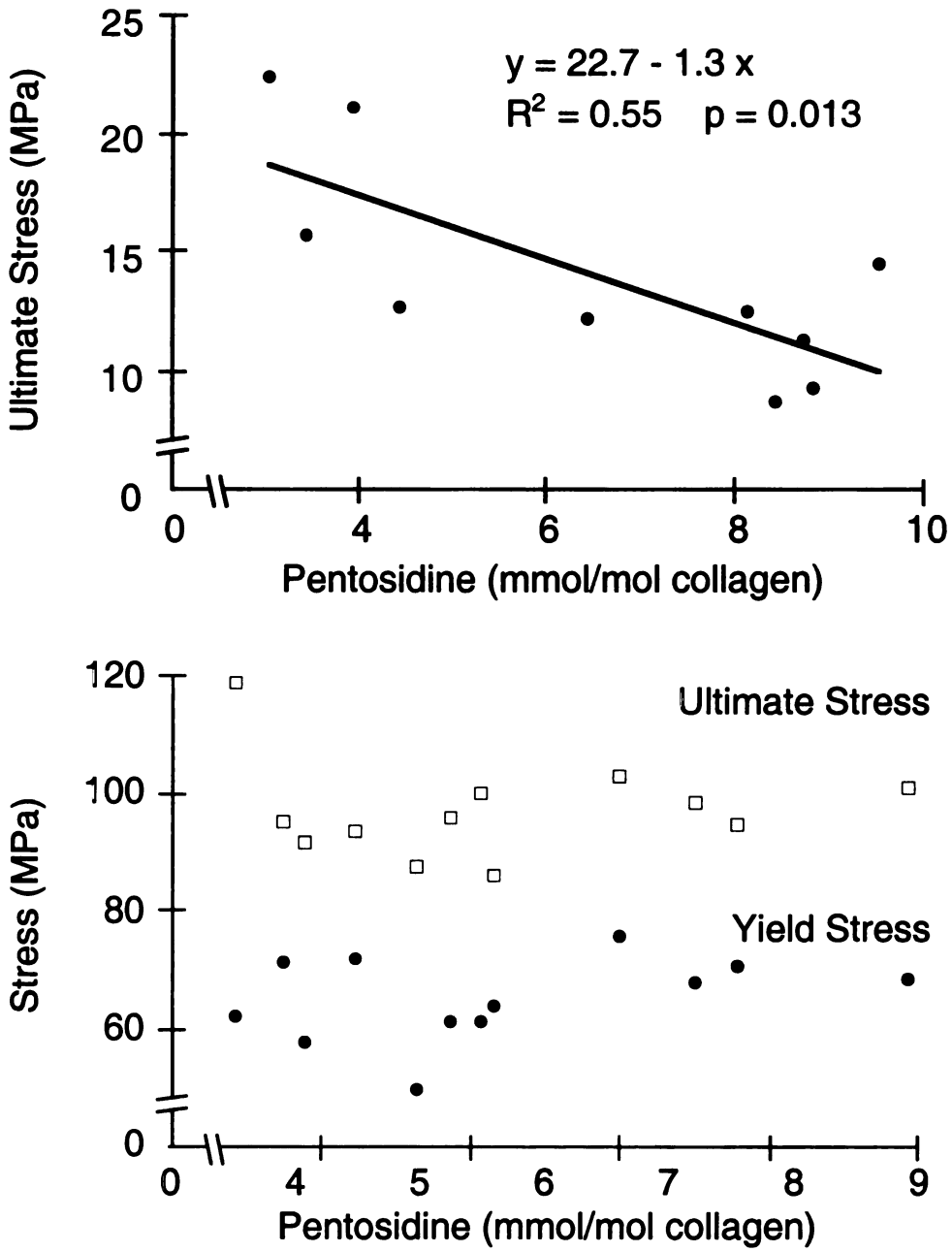

Figure C.2. Ultimate stress of demineralized human femoral cortical bone (top) and yield and ultimate stress of human femoral cortical bone (bottom) vs. pentosidine level. For demineralized bone, ultimate stress decreased with increasing pentosidine cross-link density ($p = 0.013$). For the intact bone, neither yield nor ultimate stress was related to cross-link density ($p = 0.25$ and $p = 0.88$, respectively); the average values were 66.8 MPa and 95 MPa, respectively.

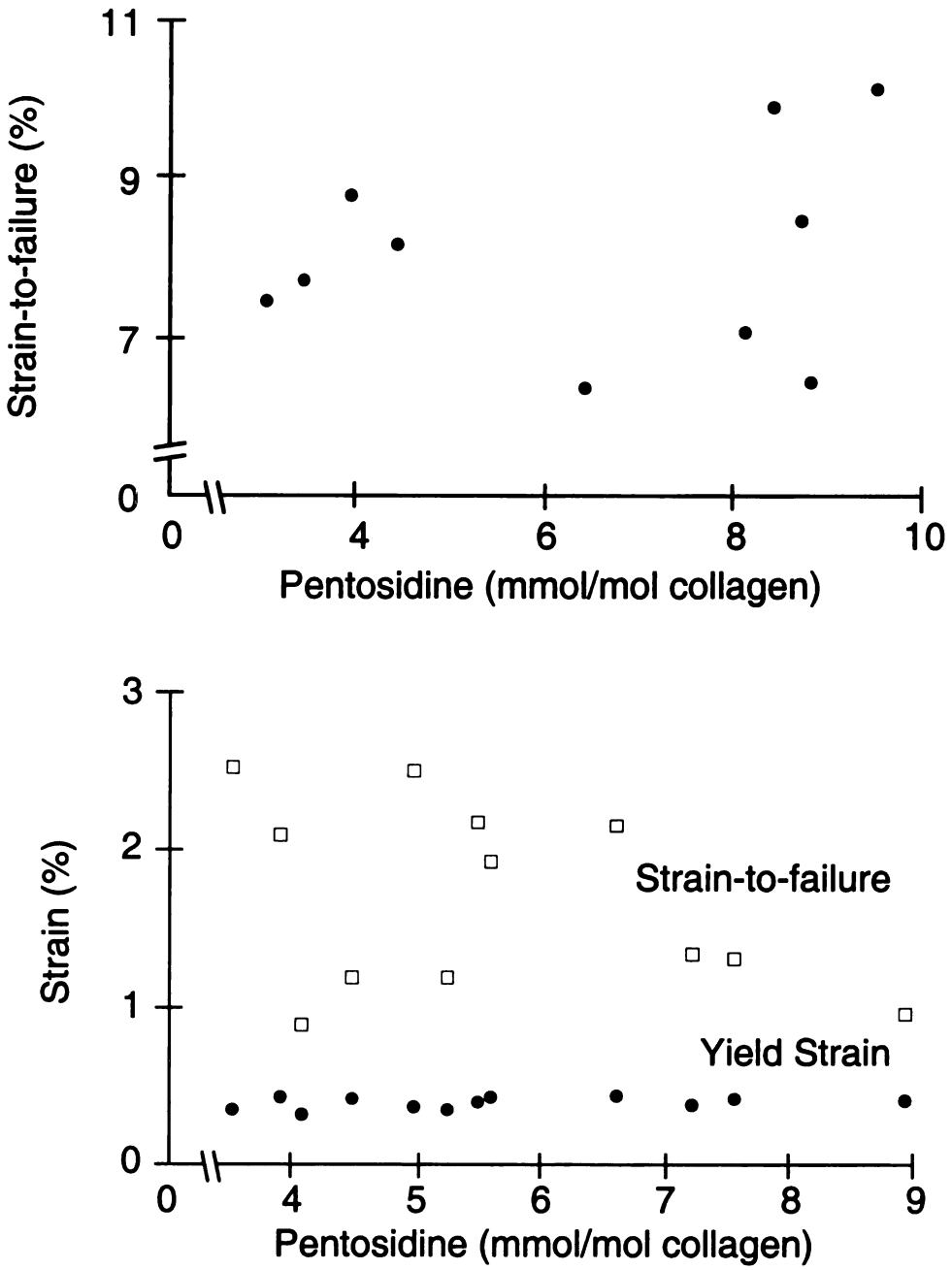

Figure C.3. Strain-to-failure of demineralized human femoral cortical bone (top) and yield strain and strain-to-failure (bottom) of human femoral cortical bone vs. pentosidine level. None of the parameters changed significantly with pentosidine cross-linking level ($p > 0.20$). The average values were 8.7%, 0.41% and 1.63% respectively.

Appendix F. Standard operating procedure for ashing cortical bone

University of California Berkeley

Orthopaedic Biomechanics Laboratory

Standard Operating Procedure

Ashing Cortical Bone

Date: 10-27-95

Author: Joseph Catanese III

Principle Investigator: Tony M. Keaveny

Summary: This document outlines the protocol for ashing cortical bone specimens. The ashed specimens can then be weighed (for calculating ash density).

Key Words: cortical bone, ashing, ash weight, furnace

Materials: dry cortical bone specimens, crucible boats, furnace (Thermolyne 1300)

1. Place dry specimen in a labeled, dry, clean crucible boat.
2. Place crucible boat in furnace with furnace at room temperature (turned off).
3. Close furnace door.
4. Turn furnace on.
5. Set furnace temperature to 700° C.
6. Allow specimen to remain at 700° C for 18 hours.
7. Open furnace and allow furnace to cool for one hour.
8. Carefully remove crucible and specimen. Note that specimens will be extremely brittle.

Appendix G. Standard operating procedure for decalcifying cortical bone

University of California Berkeley

Orthopaedic Biomechanics Laboratory

Standard Operating Procedure

Decalcifying Cortical Bone

Date: 10-27-95

Author: Joseph Catanese III

Principle Investigator: Tony M. Keaveny

Summary: This document outlines the protocol for decalcifying cylindrical cortical bone specimens. The decalcified bone specimens can then be weighed (for calculating organic content) or prepared for mechanical testing.

Key Words: cortical bone, declacification, hydroxyapatite removal, collagen, EDTA

Materials: cortical bone samples, buffered EDTA solution, plastic specimen vial, refrigerator, paraffin wax, oven, 100 ml beaker

I. DECALCIFICATION PROCEDURE

1. Melt dental or paraffin wax.
2. Cover each end of specimen in wax (Jonas *et al.*, 1993). For mechanical testing, a minimum of 10 mm must be covered on each end to allow for end capping or gripping on the test machine.
3. Allow wax to dry completely, approximately 20 minutes.
4. Submerse sample in 19% (0.5 M) solution of EDTA at 4°C (Jonas *et al.*, 1993). To maintain a solution to specimen volume ratio of 15:1, 3.5 ml of solution should be used for each sample (Kiviranta *et al.*, 1980). Solution does not need to be shaken or stirred (Kiviranta *et al.*, 1980).

5. Replace EDTA solution with fresh solution every 24 hours for 10 days (Jonas *et al.*, 1993).
6. After 10 days, rinse sample with isotonic saline solution and then submerse in isotonic saline solution for 24 hours at in refrigerator at 4°C.

I. PREPARING 19% (0.5M) ETDA SOLUTION

1. Mix 0.1 Mole of Tris HCl buffer in 1 L of deionized H_2O.
2. Add NaOH tablets until pH is raised to 8 or 9.
3. Add 0.5 Moles of EDTA to solution and stir. This will cause the pH to drop.
4. Add NaOH until pH is restored to 7.4-7.6 and all solids are dissolved.
5. Add 0.01g (1%wt/volume) Sodium Azide (NaN_3) to solution and stir.

Note: Molecular weights are listed on the chemical jars. Some are listed as "F.W." (formula weight).

I. PREPARING ISOTONIC SALINE SOLUTION

1. Mix 26.31g NaCl to 3 L deionized H_2O
2. Add 0.03g (1%wt/volume) Sodium Azide (NaN_3) to solution and stir.

I. REFERENCES

Hasegawa, K. B., D.B.; Turner, C.H. (1994). Contribution of Collagen and Mineral to Anisotropy of Osteonal Bone. *40th Transactions of the Orthopaedic Research Society*, 54, 10.

Jonas, J., Burns, J., Abel, E. W., Cresswell, M. J., Strain, J. J., & Paterson, C. R. (1993). A technique for the tensile testing of demineralised bone. *J Biomech*, 26(3), 271-6.

Kiernan, J. A. (1981). *Histological and Histochemical Methods*. Oxford: Pergamon Press.

Kiviranta, I., Tammi, M., Lappalainen, R., Kuusela, T., & Helminen, H. J. (1980). The rate of calcium extraction during EDTA decalcification from thin bone slices as assessed with atomic absorption spectrophotometry. *Histochemistry*, 68(2), 119-27.

Walsh, W. R. (1990). *Electrokinetic and Mechanical Properties of Bone.* Ph.D. Thesis, Rutgers.

Appendix H. Standard operating procedure for deorganifying cortical bone

University of California Berkeley

Orthopaedic Biomechanics Laboratory

Standard Operating Procedure

Deorganifying Cortical Bone

Date: 10-27-95

Author: Joseph Catanese III

Principle Investigator: Tony M. Keaveny

Summary: This document outlines the protocol for deorganifying cortical bone specimens. The deorganified bone specimens can then be weighed (for calculating ash density, or amount of organic material removed) or prepared for mechanical testing.

Key Words: cortical bone, deorganification, ash weight, furnace, collagen removal

---

Materials: dry cortical bone samples, crucible boats, furnace (Thermolyne 1300)

1. Place dry specimen in a labeled, dry, clean crucible boat.
2. Place crucible boat in furnace with furnace at room temperature (turned off).
3. Close furnace door.
4. Turn furnace on.
5. Set furnace to 150° C.
6. Wait one hour for furnace and specimen to reach temperature.
7. Set furnace to 165 °C.
8. Wait 15 minutes for furnace and specimen to reach temperature.
9. Repeat furnace adjustments in 15° C increments every 15 minutes until a final temperature of 350° C is reached.
10. Allow specimen to remain at 350° C for 72 hours.

11. Reduce temperature in furnace in 15° C increments every 15 minutes until a final temperature of 150° C is reached.
12. Turn furnace off and allow to cool for two hours (to room temperature) with the door closed.
13. Open furnace.
14. Carefully remove crucible and specimen. Note that specimens will be extremely brittle.

Appendix I. Standard operating procedure for measuring the ash density of cortical bone

University of California Berkeley

Orthopaedic Biomechanics Laboratory

Standard Operating Procedure

Measuring the Ash Density of Cortical Bone

Created: October 27, 1995

Modified: February 5, 1997

Author: Joseph Catanese, III

Principle Investigator: Tony M. Keaveny

Summary: This document outlines the protocol for measuring ash density of cortical bone specimens. Ash density is defined as the mass of mineral in a sample divided by the dry weight of the sample.

Key Words: cortical bone, ashing, ash weight, ash density, oven, furnace

Materials: cortical bone specimens, crucible boats, furnace (Thermolyne 1300), oven, thermocouple, thermocouple reader, thermometer, Mettler balance, tweezers, forceps, crucible tongs

I. MEASURING DRY WEIGHT

1. Dry the bone specimens.

1.1 Set oven temperature to 49°C (120°F). The temperature selector dial on the oven is not calibrated. Temperature can be read with the thermometer on top of the oven or with the thermocouple and thermocouple reader. Getting the correct temperature requires several adjustments and the oven needs approximately 30 minutes to reach a steady state temperature after making an adjustment. Be sure to set the oven temperature before preparing specimens for drying.

1.2 Dry each specimen with gauze or an air jet.

1.3 Place each specimen in a labeled crucible boat.

1.4 Place all crucible boats with specimens into oven.

2. Measure the dry weight of each specimen.

2.1 Remove the specimens after 24 hours in the oven.

2.2 Weigh each specimen directly on the weighing pan (*i.e.* without the crucible) of the Mettler balance.

2.3 Return the specimens to their crucibles and place the crucibles in the oven.

2.4 Calculate the daily change in mass using the following formula:

$$\Delta mass_{day} = \left| \frac{mass_{today} - mass_{yesterday}}{mass_{today}} \right| \times 100\%.$$

2.5 Repeat steps 2.1-2.4 until the daily change in mass is less than 1% for every specimen. The final mass recorded for each specimen is the dry mass of that specimen.

II. MEASURING ASH WEIGHT

1. Ash the specimens.

1.1 Turn furnace on and set temperature to 700°C. Furnace temperature is set by rotating the black dial while holding the "set" button down.

1.2 After furnace has reached steady state temperature, place all crucibles with specimens into the furnace.

1.3 After 18 hours in the furnace, remove specimens and turn furnace off.

2. Calculate the ash density of the specimens.

2.1 After one hour, carefully remove each specimen from the crucible with tweezers or forceps and weight directly on the weighing pan of the Mettler balance. This is the ash mass.

2.2 Calculate ash density for each specimen using the following formula:

$$\rho_{ash} = \frac{mass_{ash}}{mass_{dry}} \times 100\%.$$

Note: For cortical bone, ash density should be between 68% and 72%.

References

1. Vesalius, A., "De humani corporis fabrica libra septum," Basel (1543).

2. McMurrich, J. P., "Leonardo Da Vinci the anatomist." The Williams & Wilkins Co., Baltimore (1930).

3. Wolff, J., "The law of bone remodelling." Springer-Verlag, Berlin ; New York. XII, 126 (1986).

4. Goulet, R. W., S. A. Goldstein, M. J. Ciarelli, J. L. Kuhn, M. B. Brown, and L. A. Feldkamp, "The relationship between the structural and orthogonal compressive properties of trabecular bone," *J Biomech*, **27**:375-89 (1994).

5. Havers, C., "Osteologica nova," London (1691).

6. van Leeuwenhoek, A., "The select works of Anthony van Leeuwenhoek, containing his microscopical discoveries in many of the works of nature." Samuel Hoole. London, 1798.

7. Carando, S., M. Portigliatti Barbos, A. Ascenzi, and A. Boyde, "Orientation of collagen in human tibial and fibular shaft and possible correlation with mechanical properties," *Bone*, **10**:139-42 (1989).

8. Cartwright, A. G., "The effect of histological variation on the tensile strength of cortical bone," *Biomed Eng*, **10**:442-6 (1975).

9. Evans, F. G., "Relations between torsion properties and histology of adult human compact bone," *J Biomech*, **11**:157-65 (1978).

10. Evans, F. G., "Mechanical properties and histology of cortical bone from younger and older men," *Anatomical Record*, **185**:1-11 (1976).

11. Oxnard, C. E., "Bone and bones, architecture and stress, fossils and osteoporosis," *J Biomech*, **26 Suppl 1**:63-79 (1993).

12. Martin, R. B., and J. Ishida, "The relative effects of collagen fiber orientation, porosity, density, and mineralization on bone strength," *J Biomech*, **22**:419-26 (1989).

13. Martin, R. B., and D. L. Boardman, "The effects of collagen fiber orientation, porosity, density, and mineralization on bovine cortical bone bending properties," *J Biomech*, **26**:1047-54 (1993).

14. Ascenzi, A., A. Boyde, P. Bianco, and M. Portigliatti Barbos, "Relationship between mechanical properties and structure in secondary bone," *Connect Tissue Res*, **15**:73-6 (1986).

15. Ascenzi, A., S. Improta, M. Portigliatti Barbos, S. Carando, and A. Boyde, "Distribution of lamellae in human femoral shafts deformed by bending with inferences on mechanical properties," *Bone*, **8**:319-25 (1987).

16. Evans, F. G., and R. Vincentelli, "Relations of the compressive properties of human cortical bone to histological structure and calcification," *J. Biomech.*, **7**:1-10 (1974).

17. Currey, J. D., "Changes in the impact energy absorption of bone with age," *J. Biomech.*, **12**:459-69 (1979).

18. Currey, J. D., "Physical characteristics affecting the tensile failure properties of compact bone," *J. Biomech.*, **23**:837-44 (1990).

19. McCalden, R. W., J. A. McGeough, M. B. Barker, and C. M. Court-Brown, "Age-related changes in the tensile properties of cortical bone. The relative importance of changes in porosity, mineralization, and microstructure," *J. Bone Joint Surg. [Am]*, **75**:1193-205 (1993).

20. Eyre, D. R., I. R. Dickson, and K. Van Ness, "Collagen cross-linking in human bone and articular cartilage. Age-related changes in the content of mature hydroxypyridinium residues," *Biochem. J.*, **252**:495-500 (1988).

21. Reid, S. A., and A. Boyde, "Changes in the mineral density distribution in human bone with age: image analysis using backscattered electrons in the SEM," *J. Bone Miner. Res.*, **2**:13-22 (1987).

22. Legros, R., N. Balmain, and G. Bonel, "Age-related changes in mineral of rat and bovine cortical bone," *Calcif. Tissue Int.*, **41**:137-44 (1987).

23. Burstein, A. H., D. T. Reilly, and M. Martens, "Aging of bone tissue: mechanical properties," *J. Bone Joint Surg. [Am]*, **58**:82-6 (1976).

24. Posner, A. S., A. Perloff, and A. F. Diorio, "Refinement of the hydroxyapatite structure," *Acta Crystalographica*, **11**:308-309 (1958).

25. Armstrong, W. D., "Composition and Structure of Bone Mineral," *In* Biology of hard tissue: proceedings. A. M. Budy, editor. New York Academy of Sciences, Interdisciplinary Communications Program, New York. 1967, 362 p.

26. Nelson, D. G., and J. D. Featherstone, "Preparation, analysis, and characterization of carbonated apatites," *Calcif. Tissue Int.*, **34 Suppl 2**:S69-81 (1982).

27. Rey, C., J. L. Miquel, L. Facchini, A. P. Legrand, and M. J. Glimcher, "Hydroxyl groups in bone mineral," *Bone*, **16**:583-6 (1995).

28. Rey, C., H. M. Kim, L. Gerstenfeld, and M. J. Glimcher, "Structural and chemical characteristics and maturation of the calcium-phosphate crystals formed during the calcification of the organic matrix synthesized by chicken osteoblasts in cell culture," *J. Bone Miner. Res.*, **10**:1577-88 (1995).

29. Ziv, V., and S. Weiner, "Bone crystal sizes: a comparison of transmission electron microscopic and X-ray diffraction line width broadening techniques," *Connect. Tissue Res.*, **30**:165-75 (1994).

30. Steve-Bocciarelli, D., "Morphology of crystallites in bone," *Calcif. Tissue Res.*, **5**:261-9 (1970).

31. Ichijo, T., Y. Yamashita, and T. Terashima, "Observations on structural features and characteristics of biological apatite crystals. 5. Three-dimensional observation on ultrastructure of human enamel crystals," *Bull. Tokyo Med. Dent. Univ.*, **40**:135-46 (1993).

32. Lowenstam, H. A., and S. Weiner, "On Biomineralization." Oxford University Press, New York. 324 (1989).

33. Ashbee, K., "Fundamental Principles of Fiber Reinforced Composites." Technomic, Lancaster (1993).

34. Sendeckyj, G. P., "Mechanics of composite materials," *In* Composite materials v. 2. Academic Press, New York. xv, 503 p (1974).

35. Agarwal, B. D., and L. J. Broutman, "Analysis and performance of fiber composites." John Wiley & Sons, Inc., New York. 449 (1990).

36. Fernández-Morán, H., and A. Engström, "Electron microscopy and x-ray diffraction of bone," *Biochimica et Biophysica Acta*, **23**:260-263 (1957).

37. Engström, A., "Apatite-collagen organization in calcified tendon," *Exp. Cell Res.*, **43**:241-5 (1966).

38. Speckman, T. W., and W. P. Norris, "Bone crystallites as observed by use of the electron microscope," *Nature*, 179:753 (1957).

39. Johansen, E., and H. F. Parks, "Electron microscopic observations on the three-dimensional morphology of apatite crystallites of human dentine and bone," *J. Biophys. Biochem. Cytol.*, **7**:743-746 (1960).

40. Weiner, S., and P. A. Price, "Disaggregation of bone into crystals," *Calcif. Tissue Int.*, **39**:365-75 (1986).

41. Kim, H., C. Rey, and M. J. Glimcher, "X-ray diffraction, electron microscopy, and Fourier transform infrared spectroscopy of apatite crystals isolated from chicken and bovine calcified cartilage," *Calcif. Tissue Int.*, **59**:58-63 (1996).

42. Weiner, S., and W. Traub, "Organization of hydroxyapatite crystals within collagen fibrils," *FEBS Letters*, **206**:262-6 (1986).

43. Weiner, S., and W. Traub, "Crystal size and organization in bone," *Connect. Tissue Res.*, **21**:259-65 (1989).

44. Arsenault, A. L., and M. D. Grynpas, "Crystals in calcified epiphyseal cartilage and cortical bone of the rat," *Calcif. Tissue Int.*, **43**:219-25 (1988).

45. Holden, J. L., J. G. Clement, and P. P. Phakey, "Age and temperature related changes to the ultrastructure and composition of human bone mineral," *J. Bone Miner. Res.*, **10**:1400-9 (1995).

46. Kim, H. M., C. Rey, and M. J. Glimcher, "Isolation of calcium-phosphate crystals of bone by non-aqueous methods at low temperature," *J. Bone Miner. Res.*, **10**:1589-601 (1995).

47. Robinson, R. A., and M. L. Watson, "Collagen-crystal relationships in bone as seen in the electron microscope," *Anat. Rec.*, **114**:383-409 (1952).

48. Landis, W. J., M. C. Paine, and M. J. Glimcher, "Electron microscopic observations of bone tissue prepared anhydrously in organic solvents," *J. Ultrastruct. Res.*, **59**:1-30 (1977).

49. Arsenault, A. L., "A comparative electron microscopic study of apatite crystals in collagen fibrils of rat bone, dentin and calcified turkey leg tendons," *Bone and Mineral*, **6**:165-77 (1989).

50. Fratzl, P., N. Fratzl-Zelman, K. Klaushofer, G. Vogl, and K. Koller, "Nucleation and growth of mineral crystals in bone studied by small-angle X-ray scattering," *Calcif. Tissue Int.*, **48**:407-13 (1991).

51. Fratzl, P., M. Groschner, G. Vogl, H. Plenk, Jr., J. Eschberger, N. Fratzl-Zelman, K. Koller, and K. Klaushofer, "Mineral crystals in calcified tissues: a comparative study by SAXS," *J. Bone Miner. Res.*, **7**:329-34 (1992).

52. Matsushima, N., M. Akiyama, and Y. Terayama, "Quantitative analysis of the orientation of mineral in bone from small-angle x-ray scattering patterns," *Japanese Journal of Applied Physics*, **21**:186-189 (1982).

53. Guinier, A., "X-ray diffraction in crystals, imperfect crystals, and amorphous bodies." W.H. Freeman, San Francisco. X, 378 p. (1963).

54. Weiner, S., and W. Traub, "Bone structure: from angstroms to microns," *Faseb J.*, **6**:879-85 (1992).

55. Traub, W., T. Arad, and S. Weiner, "Growth of mineral crystals in turkey tendon collagen fibers," *Connect. Tissue Re.s*, **28**:99-111 (1992).

56. Traub, W., T. Arad, and S. Weiner, "Origin of mineral crystal growth in collagen fibrils," *Matrix*, **12**:251-5 (1992).

57. Morgulis, S., "Studies on the chemical composition of bone ash," *J. Biol. Chem.*, **93**:455-466 (1931).

58. Peckham, S. C., F. L. Losee, and I. Ettleman, "Ethylenediamine vs. KOH-Glycol in the removal of the organic matter of dentin," *J. Dent. Res.*, **35**:947-49 (1956).

59. Gabriel, S., *Z. Physiol. Chem.*, **18** (1894).

60. Skinner, H. C., E. S. Kempner, and C. Y. Pak, "Preparation of the mineral phase of bone using ethylenediamine extraction," *Calcif. Tissue Res.*, **10**:257-68 (1972).

61. Hurley, L. A., and F. L. Losee, "Anorganic Bone—Chemistry, Anatomy, and Biological Reactions," *Military Medicine*:101-104 (1957).

62. Wheeler, T. E., and G. W. Hyatt, "A study of the residual nitrogen in bone following extraction with ethylenediamine," *JBJS*, **42-A**:1435-41 (1960).

63. Williams, J. B., and J. W. Irvine, "Preparation of the inorganic matrix of bone," *Science*, **119**:771-772 (1954).

64. Swedlow, D. B., P. Frasca, R. A. Harper, and J. L. Katz, "Scanning and transmission electron microscopy of calcified tissues," *Biomater Med Devices Artif Organs*, **3**:121-53 (1975).

65. Termine, J. D., E. D. Eanes, D. J. Greenfield, M. U. Nylen, and R. A. Harper, "Hydrazine-deproteinated bone mineral. Physical and chemical properties," *Calcif. Tissue Res.*, **12**:73-90 (1973).

66. Guizzardi, S., M. Raspanti, D. Martini, R. Scandroglio, P. Govoni, and A. Ruggeri, "Low-temperature heat-deproteinated compact bone to heal large bone defects," *Biomaterials*, **16**:931-6 (1995).

67. Raspanti, M., S. Guizzardi, V. De Pasquale, D. Martini, and A. Ruggeri, "Ultrastructure of heat-deproteinated compact bone," *Biomaterials*, **15**:433-7 (1994).

68. Sakae, T., H. Mishima, and Y. Kozawa, "Changes in bovine dentin mineral with sodium hypochlorite treatment," *J. Dent. Res.*, **67**:1229-34 (1988).

69. Callens, F., P. Moens, and R. Verbeeck, "An EPR study of intact and powdered human tooth enamel dried at 400 degrees C," *Calcif. Tissue Int.*, **56**:543-8 (1995).

70. Moradian-Oldak, J., S. Weiner, L. Addadi, W. J. Landis, and W. Traub, "Electron imaging and diffraction study of individual crystals of bone, mineralized tendon and synthetic carbonate apatite," *Connect .Tissue Res.*, **25**:219-28 (1991).

71. Landis, W. J., J. Moradian-Oldak, and S. Weiner, "Topographic imaging of mineral and collagen in the calcifying turkey tendon," *Connect. Tissue Res.*, **25**:181-96 (1991).

72. Armstrong, W. D., and L. Singer, "Composition and constitution of the mineral phase of bone," *Clin. Orthop.*, **38**:179-90 (1965).

73. Termine, J. D., and A. S. Posner, "Amorphous/crystalline interrelationships in bone mineral," *Calcif. Tissue Res.*, **1**:8-23 (1967).

74. Sweeney, A. W., R. P. Kroon, and R. K. Byers, "Mechanical characteristics of bone and its constituents," *ASME 65-WA/HUF-7*: 1-17 (1965).

75. Mack, R. W., "Bone - A natural two-phase material." University of California, San Francisco-Berkeley (1964).

76. Tomazic, B. B., W. E. Brown, and E. D. Eanes, "A critical evaluation of the purification of biominerals by hypochlorite treatment," *J. Biomed. Mater. Res.*, **27**:217-25 (1993).

77. Aerssens, J., R. Van Audekercke, P. Geusens, L. P. Schot, A. A. Osman, and J. Dequeker, "Mechanical properties, bone mineral content, and bone composition (collagen, osteocalcin, IGF-I) of the rat femur: influence of ovariectomy and nandrolone decanoate (anabolic steroid) treatment," *Calcif. Tissue Int.*, **53**:269-77 (1993).

78. Balmain, N., R. Legros, and G. Bonel, "X-ray diffraction of calcined bone tissue: a reliable method for the determination of bone Ca/P molar ratio," *Calcif. Tissue Int.*, **34 Suppl 2**:S93-8 (1982).

79. Kurosawa, H., H. Aoki, and M. Akao, "Tissue reactions to calcined bone graft," *Biomaterials*, **7**:132-6 (1986).

80. Callens, F. J., R. M. Verbeeck, D. E. Naessens, P. F. Matthys, and E. R. Boesman, "Effect of carbonate content on the ESR spectrum near g = 2 of carbonated calciumapatites synthesized from aqueous media," *Calcif. Tissue Int.*, **44**:114-24 (1989).

81. Ramachandran, G. N., and G. Kartha, *Proc. Indian Acad. Sci.*, **42**:215 (1955).

82. Ramachandran, G. N., and G. Kartha, *Nature*, **174**:269 (1954).

83. Hofmann, H., P. P. Fietzek, and K. Kuhn, "Comparative analysis of the sequences of the three collagen chains alpha 1(I), alpha 2 and alpha 1(III) Functional and genetic aspects," *J. Mol. Biol.*, **141**:293-314 (1980).

84. Boedtker, H., and P. Doty, "On the nature of the structural element of collagen," *J. Am. Chem. Soc.*, **77**:248-9 (1955).

85. Miller, A., "Collagen: the organic matrix of bone," *Philos. Trans. R. Soc. Lond. B. Biol. Sci.*, **304**:455-77 (1984).

86. Hodge, A. J., and J. A. Petruska, *In* Aspects of protein structure. G. N. Ramachandran, editor. Academic Press, London. 1963, 239.

87. Olsen, B. R., "Electron microscope studies on collagen," *Z. Zellforsch*, **59**:199 (1963).

88. Lees, S., "A mixed packing model for bone collagen," *Calcif. Tissue Int.*, **33**:591-602 (1981).

89. Hulmes, D. J., and A. Miller, "Quasi-hexagonal molecular packing in collagen fibrils," *Nature*, **282**:878-80 (1979).

90. Grynpas, M. D., D. R. Eyre, and D. A. Kirschner, "Collagen type II differs from type I in native molecular packing," *Biochim. Biophys. Acta*, **626**:346-55 (1980).

91. Brodsky, B., and E. Eikenberry, "Supramolecular collagen assemblies," *Ann. N.Y. Acad. Sci.*, **460**:73-84 (1985).

92. Bonar, L. C., S. Lees, and H. A. Mook, "Neutron diffraction studies of collagen in fully mineralized bone," *J. Mol. Biol.*, **181**:265-70 (1985).

93. Katz, E. P., and S. T. Li, "The intermolecular space of reconstituted collagen fibrils," *J. Mol. Biol.*, **73**:351-69 (1973).

94. Yamauchi, M., E. P. Katz, K. Otsubo, K. Teraoka, and G. L. Mechanic, "Cross-linking and stereospecific structure of collagen in mineralized and nonmineralized skeletal tissues," *Connect. Tissue Res.*, **21**:159-67; discussion 168-9 (1989).

95. Lees, S., "Considerations regarding the structure of the mammalian mineralized osteoid from viewpoint of the generalized packing model," *Connect. Tissue Res.*, **16**:281-303 (1987).

96. Marotti, G., "A new theory of bone lamellation," *Calcif. Tissue. Int.*, **53 Suppl 1**:S47-55; discussion S56 (1993).

97. Gebhardt, W., "Ueber funktionell wichtige Anordnungsweisen der groeberen und feineren Bauelemente des Wirbeltierknochens," *Arch. Entwickl. Mech. Org.*, **11**:383-498 (1901).

98. Gebhardt, W., "Ueber funktionell wichtige Anordnungsweisen der groeberen und feineren Bauelemente des Wirbeltierknochens," *Arch. Entwickl. Mech. Org.*, **12**:1-167 (1901).

99. Gebhardt, W., "Ueber funktionell wichtige Anordnungsweisen der groeberen und feineren Bauelemente des Wirbeltierknochens II. Spezieller til. Der bau der Haversschen lamellensysteme und seine funktionelle bedeutung," *Arch. Entwickl. Mech. Org.*, **20**:187-322 (1905).

100. Weiner, S., T. Arad, I. Sabanay, and W. Traub, "Rotated plywood structure of primary lamellar bone in the rat: orientations of the collagen fibril arrays," *Bone*, **20**:509-14 (1997).

101. Giraud-Guille, M. M., "Twisted plywood architecture of collagen fibrils in human compact bone osteons," *Calcif. Tissue Int.*, **42**:167-80 (1988).

102. Ruth, E. B., "Bone studies I. fibrillar structure of adult human bone," *Amer. J. Anat.*, **80**:35-53 (1947).

103. Ranvier, J., "Traité technique d'histologie." Savy, Paris (1889).

104. Ziegler, O., "Studien uber die feinere struktur des rohrenknochens und dessen polarisation," *Dtsh. z. chir.*, **85** (1906).

105. Rouiller, C., "Collagen fibres in connective tissue," *In* The bchemistry and physiology of bone. G. H. Bourne, editor. Academic Press, New York. 1956, 104-47.

106. Marotti, G., M. A. Muglia, and C. Palumbo, "Structure and function of lamellar bone," *Clin. Rheumatol.*, **13 Suppl 1**:63-8 (1994).

107. Marotti, G., "The original contribution of the scanning electron microscope to the knowledge of bone structure," *In* Ultrastructure of skeletal tissues : bone and cartilage in health and disease. E. Bonucci and P. M. Motta, editors. Kluwer Academic, Boston. 19-39, (1990).

108. Marotti, G., and M. A. Muglia, "A scanning electron microscope study of human bony lamellae. Proposal for a new model of collagen lamellar organization," *Arch. Ital. Anat. Embriol.*, **93**:163-75 (1988).

109. Portigliatti Barbos, M., P. Bianco, A. Ascenzi, and A. Boyde, "Collagen orientation in compact bone: II. Distribution of lamellae in the whole of the human femoral shaft with reference to its mechanical properties," *Metab. Bone. Dis. Relat. Res.*, **5**:309-15 (1984).

110. Boyde, A., and M. H. Hordell, "Scanning electron microscopy of lamellar bone," *Z. Zellforsch. Mikrosk. Anat.*, **93**:213-31 (1969).

111. Engström, A., and B. Engfeldt, "Lamellae structure of osteons demonstrated by microradiography," *Experientia*, **9**:25 (1953).

112. Currey, J., "The mechanical adaptations of bones." Princeton University Press, Princeton. 293 (1984).

113. Ortner, D. J., and D. W. Von Endt, "Microscopic and electron microprobe characterization of the sclerotic lamellae in human osteons," *Isr. J. Med. Sci.*, **7**:480-2 (1971).

114. Frasca, P., "Scanning-electron microscopy studies of 'ground substance' in the cement lines, resting lines, hypercalcified rings and reversal lines of human cortical bone," *Acta Anat. (Basel)*, **109**:115-21 (1981).

115. Burr, D. B., M. B. Schaffler, and R. G. Frederickson, "Composition of the cement line and its possible mechanical role as a local interface in human compact bone," *J. Biomech.*, **21**:939-45 (1988).

116. Schaffler, M. B., D. B. Burr, and R. G. Frederickson, "Morphology of the osteonal cement line in human bone," *Anat. Rec.*, **217**:223-8 (1987).

117. Braidotti, P., "Studio dell'adattamento funzionale dell'osso normale e patologico nei suoi aspetti di macro e micromeccanica." University di Roma, Rome (1992).

118. Ascenzi, A., and E. Bonucci, "The compressive properties of single osteons," *Anat. Rec.*, **161**:377-91 (1968).

119. Reid, S. A., "A study of lamellar organisation in juvenile and adult human bone," *Anat. Embryol. (Berl)*, **174**:329-38 (1986).

120. Frasca, P., R. A. Harper, and J. L. Katz, "Collagen fiber orientations in human secondary osteons," *Acta. Anat. (Basel)*, **98**:1-13 (1977).

121. Ascenzi, A., and E. Bonucci, "The tensile properties of single osteons," *Anat. Rec.*, **158**:375-86 (1967).

122. Carter, D. R., and D. M. Spengler, "Mechanical properties and composition of cortical bone," *Clin. Orthop.*, **135**:192-217 (1978).

123. Lees, S., J. D. Heeley, and P. F. Cleary, "A study of some properties of a sample of bovine cortical bone using ultrasound," *Calcif. Tissue Int.*, **29**:107-17 (1979).

124. Park, J. B., "Biomaterials science and engineering." Plenum Press, New York. 459 (1984).

125. Hall, B. K., "Matrix and Cell Specific Products," *In* Bone. Vol. 6. B. K. Hall, editor. Telford Press, Caldwell, N.J. (1990).

126. Hodge, A. J., "Molecular models illustrating the possible distributions of 'holes' in simple systematically staggered arrays of type I collagen molecules in native-type fibrils," *Connect. Tissue Res.*, **21**:137-47 (1989).

127. Younger, E. M., and M. W. Chapman, "Morbidity at bone graft donor sites," *J. Ortho. Trauma.*, **3**:192-5 (1989).

128. Nolan, P., P. Templeton, R. A. Mollan, and D. J. Wilson, "Osteoinductive potential of human demineralised bone and a bioceramic in abdominal musculature of the rat," *J. Anat.*, **174**:97-102 (1991).

129. Marinak, K. W., J. T. Mellonig, and H. J. Towle, "The osteogenic potential of two human demineralized bone preparations using a xenogeneic model," *J. Periodontol.*, **60**:12-8 (1989).

130. Bos, G. D., V. M. Goldberg, J. M. Zika, K. G. Heiple, and A. E. Powell, "Immune responses of rats to frozen bone allografts," *J. Bone Joint Surg. [Am]*, **65**:239-46 (1983).

131. Bonfiglio, M., and W. S. Jeter, "Immunological responses to bone," *Clin. Orthop.*, **87**:19-27 (1972).

132. Bucholz, R. W., A. Carlton, and R. Holmes, "Interporous hydroxyapatite as a bone graft substitute in tibial plateau fractures," *Clin. Orthop.*, **240**:53-62 (1989).

133. Light, M., and I. O. Kanat, "The possible use of coralline hydroxyapatite as a bone implant," *J. Foot Surg.*, **30**:472-6 (1991).

134. Doherty, M. J., G. Schlag, N. Schwarz, R. A. Mollan, P. C. Nolan, and D. J. Wilson, "Biocompatibility of xenogeneic bone, commercially available coral, a bioceramic and tissue sealant for human osteoblasts," *Biomaterials*, **15**:601-8 (1994).

135. Begley, C. T., M. J. Doherty, R. A. Mollan, and D. J. Wilson, "Comparative study of the osteoinductive properties of bioceramic, coral and processed bone graft substitutes," *Biomaterials*, **16**:1181-5 (1995).

136. Guillemin, G., A. Meunier, P. Dallant, P. Christel, J. C. Pouliquen, and L. Sedel, "Comparison of coral resorption and bone apposition with two natural corals of different porosities," *J. Biomed. Mater. Res.*, **23**:765-79 (1989).

137. Holmes, R., V. Mooney, R. Bucholz, and A. Tencer, "A coralline hydroxyapatite bone graft substitute. Preliminary report," *Clin. Orthop.*, **188**:252-62 (1984).

138. Turner, T. M., D. R. Sumner, R. M. Urban, R. Igloria, and J. O. Galante, "Maintenance of proximal cortical bone with use of a less stiff femoral component in hemiarthroplasty of the hip without cement. An investigation in a canine model at six months and two years," *J. Bone Joint Surg. [Am.]*, **79**:1381-90 (1997).

139. Reilly, D. T., and A. H. Burstein, "Review article. The mechanical properties of cortical bone," *J. Bone Joint Surg. [Am]*, **56**:1001-22 (1974).

140. Keaveny, T. M., and W. C. Hayes, "A 20-year perspective on the mechanical properties of trabecular bone," *J Biomech. Eng.*, **115**:534-42 (1993).

141. Burr, D. B., C. Milgrom, D. Fyhrie, M. Forwood, M. Nyska, A. Finestone, S. Hoshaw, E. Saiag, and A. Simkin, "*In vivo* measurement of human tibial strains during vigorous activity," *Bone*, **18**:405-10 (1996).

142. Lanyon, L. E., W. G. Hampson, A. E. Goodship, and J. S. Shah, "Bone deformation recorded *in vivo* from strain gauges attached to the human tibial shaft," *Acta Orthop. Scand.*, **46**:256-68 (1975).

143. Apfelbaum, F., H. Diab, I. Mayer, and J. D. B. Featherstone, "An FTIR study of carbonate in synthetic apatites," *J. Inorg. Biochem.*, **45**:277-82 (1992).

144. Mayer, I., R. Schlam, and J. D. Featherstone, "Magnesium-containing carbonate apatites," *J. Inorg. Biochem.*, **66**:1-6 (1997).

145. American Society for Testing and Materials, "C39-88$^{\varepsilon 1}$: Standard Test Method for Compressive Strength of Cylindrical Concrete Specimens. ASTM, Philadelphia, PA. 20-24 (1986).

146. American Society for Testing and Materials, "C773-88: Standard Test Method for Compressive (Crushing) Strength of Fired Whiteware Materials. ASTM, Philadelphia, PA. 251-253 (1988).

147. Gong, J. K., J. S. Arnold, and S. H. Cohn, "Composition of trabecular and cortical bone," *Anat. Rec.*, **149**:325-32 (1964).

148. Landis, W. J., J. J. Librizzi, M. G. Dunn, and F. H. Silver, "A study of the relationship between mineral content and mechanical properties of turkey gastrocnemius tendon," *J. Bone Miner. Res.*, **10**:859-67 (1995).

149. Featherstone, J. D., S. Pearson, and R. Z. LeGeros, "An infrared method for quantification of carbonate in carbonated apatites," *Caries Res.*, **18**:63-6 (1984).

150. Kitsugi, T., T. Yamamuro, H. Takeuchi, and M. Ono, "Bonding behavior of three types of hydroxyapatite with different sintering temperatures implanted in bone," *Clin. Orthop.*, **234**:280-90 (1988).

151. Muller-Mai, C. M., S. I. Stupp, C. Voigt, and U. Gross, "Nanoapatite and organoapatite implants in bone: histology and ultrastructure of the interface," *J Biomed Mater Res*, **29**:9-18 (1995).

152. Landis, W. J., and M. J. Glimcher, "Electron diffraction and electron probe microanalysis of the mineral phase of bone tissue prepared by anhydrous techniques," *J. Ultrastruct. Res.*, **63**:188-223 (1978).

153. Pereira, R. F., E. L. Hume, K. W. Halford, and D. J. Prockop, "Bone fragility in transgenic mice expressing a mutated gene for type I procollagen (COL1A1) parallels the

age-dependent phenotype of human osteogenesis imperfecta," *J. Bone Miner. Res.*, **10**:1837-43 (1995).

154. Jepsen, K. J., S. A. Goldstein, J. L. Kuhn, M. B. Schaffler, and J. Bonadio, "Type-I collagen mutation compromises the post-yield behavior of Mov13 long bone," *J. Orthop. Res.*, **14**:493-9 (1996).

155. Byers, P. H., "Osteogenesis Imperfecta," *In* Connective tissue and its heritable disorders : molecular, genetic, and medical aspects. P. M. Royce and B. U. Steinmann, editors. Wiley-Liss, New York. 1993, xiii, 709 p.

156. Burstein, A. H., J. M. Zika, K. G. Heiple, and L. Klein, "Contribution of collagen and mineral to the elastic-plastic properties of bone," *J. Bone Joint Surg. [Am]*, **57**:956-61 (1975).

157. Broz, J. J., S. J. Simske, and A. R. Greenberg, "Material and compositional properties of selectively demineralized cortical bone," *J. Biomech.*, **28**:1357-68 (1995).

158. Bowman, S. M., J. Zeind, L. J. Gibson, W. C. Hayes, and T. A. McMahon, "The tensile behavior of demineralized bovine cortical bone," *J. Biomech.*, **29**:1497-1501 (1996).

159. Wright, T. M., F. Vosburgh, and A. H. Burstein, "Permanent deformation of compact bone monitored by acoustic emission," *J. Biomech.*, **14**:405-9 (1981).

160. Ward, I. M., and D. W. Hadley, "An introduction to the mechanical properties of solid polymers." J. Wiley & Sons, Chichester, New York. xi, 334 p. (1993).

161. Yeni, Y. N., C. U. Brown, and T. L. Norman, "Influence of bone composition and apparent density on fracture toughness of the human femur and tibia," *Bone*, **22**:79-84 (1998).

162. Yeni, Y. N., C. U. Brown, Z. Wang, and T. L. Norman, "The influence of bone morphology on fracture toughness of the human femur and tibia," *Bone*, **21**:453-9 (1997).

163. Bank, R. A., M. T. Bayliss, F. P. Lafeber, A. Maroudas, and J. M. Tekoppele, "Ageing and zonal variation in post-translational modification of collagen in normal human articular cartilage. The age-related increase in non-enzymatic glycation affects biomechanical properties of cartilage," *Biochem. J.*, **330**:345-51 (1998).

164. Uchiyama, A., T. Ohishi, M. Takahashi, K. Kushida, T. Inoue, M. Fujie, and K. Horiuchi, "Fluorophores from aging human articular cartilage," *J. Biochem. (Tokyo)*, **110**:714-8 (1991).

165. Sell, D. R., and V. M. Monnier, "Structure elucidation of a senescence cross-link from human extracellular matrix. Implication of pentoses in the aging process," *J. Biol. Chem.*, **264**:21597-602 (1989).

166. Bank, R. A., E. J. Jansen, B. Beekman, and J. M. te Koppele, "Amino acid analysis by reverse-phase high-performance liquid chromatography: improved derivatization and detection conditions with 9-fluorenylmethyl chloroformate," *Anal. Biochem.*, **240**:167-76 (1996).

167. Currey, J. D., "Three analogies to explain the mechanical properties of bone," *Biorheology*, **2**:1-10 (1964).

168. Melton, L. J. d., S. H. Kan, M. A. Frye, H. W. Wahner, W. M. O'Fallon, and B. L. Riggs, "Epidemiology of vertebral fractures in women," *Am. J. Epidemiol.*, **129**:1000-11 (1989).

169. Vogel, H. G., "Influence of maturation and aging on mechanical and biochemical properties of connective tissue in rats," *Mechanisms of Ageing and Development*, **14**:283-292 (1980).

170. Currey, J. D., K. Brear, P. Zioupos, and G. C. Reilly, "Effect of formaldehyde fixation on some mechanical properties of bovine bone," *Biomaterials*, **16**:1267-71 (1995).

171. Hashin, Z., and S. Shtrikman, "A variational approach to the theory of the elastic behavior of multiphase materials," *J. Mech. Phys. Solids*, **11**:1273 (1963).

172. Piekarski, K., "Analysis of bone as a composite material," *International Journal of Engineering Science*, **11**:557-65 (1973).

173. Katz, J. L., "Hard tissue as a composite material. I. Bounds on the elastic behavior," *J. Biomech.*, **4**:455-73 (1971).

174. Bonfield, W., and C. H. Li, "Anisotropy of non-elastic flow in bone," *J. Appl. Phys.*, **38**:2450 (1967).

175. Katz, J. L., "Composite material models for cortical bone," *In* Mechanical properties of bone : presented at the Joint ASME-ASCE Applied Mechanics, Fluids Engineering, and Bioengineering Conference, Boulder, Colorado, June 22-24, 1981. Vol. 45. S. C. Cowin, editor. American Society of Mechanical Engineers, New York, N.Y. (345 E. 47th St., New York 10017). 1981, 171-184.

176. Crolet, J. M., B. Aoubiza, and A. Meunier, "Compact bone: numerical simulation of mechanical characteristics," *J. Biomech.*, **26**:677-87 (1993).

177. Hogan, H. A., "Micromechanics modeling of Haversian cortical bone properties," *J. Biomech.*, **25**:549-56 (1992).

178. Aoubiza, B., J. M. Crolet, and A. Meunier, "On the mechanical characterization of compact bone structure using the homogenization theory," *J. Biomech.*, **29**:1539-47 (1996).

179. Sedlin, E. D., "A rheologic model for cortical bone. A study of the physical properties of human femoral samples," *Acta Orthop. Scand.* Suppl 83:1-77 (1965).

180. Fondrk, M. T., "An experimental and analytical investigation into the nonlinear constitutive equations of cortical bone," *In* Mechanical and Aerospace Engineering. Case Western Reserve University, Cleveland. 501 (1989).

181. Courtney, A., "Mechanical Properties of the Proximal Femur: Changes with Age," *In* Division of Applied Sciences. Harvard, Cambridge. 128 (1994).

182. Krajcinovic, D., J. Trafimow, and D. Sumarac, "Simple constitutive model for a cortical bone," *J. Biomech.*, **20**:779-84 (1987).

183. Black, J., R. Mattson, and E. Korostoff, "Haversian osteons: size, distribution, internal structure, and orientation," *J. Biomed. Mater. Res.*, **8**:299-319 (1974).

184. Rho, J. Y., T. Y. Tsui, and G. M. Pharr, "Elastic properties of human cortical and trabecular lamellar bone measured by nanoindentation," *Biomaterials*, **18**:1325-30 (1997).

185. Townsend, P. R., R. M. Rose, and E. L. Radin, "Buckling studies of single human trabeculae," *J. Biomech.*, **8**:199-201 (1975).

186. Ascenzi, A., M. G. Ascenzi, A. Benvenuti, and F. Mango, "Pinching in longitudinal and alternate osteons during cyclic loading," *J. Biomech.*, **30**:689-95 (1997).

187. Martin, R. B., "Porosity and specific surface of bone," *Crit. Rev. Biomed. Eng.*, **10**:179-222 (1984).

188. Currey, J. D., "The effect of porosity and mineral content on the Young's modulus of elasticity of compact bone," *J. Biomech.*, **21**:131-9 (1988).

189. Schaffler, M. B., and D. B. Burr, "Stiffness of compact bone: effects of porosity and density," *J. Biomech.*, **21**:13-6 (1988).

190. Lindahl, O., and A. G. Lindgren, "Cortical bone in man. II. Variation in tensile strength with age and sex," *Acta Orthop. Scand.*, **38**:141-7 (1967).

191. Mather, B. S., "Variation with age and sex in strength of the femur," *Med. Biol. Eng.*, **6**:129-32 (1968).

192. Zioupos, P., and J. D. Currey, "Changes in the stiffness, strength, and toughness of human cortical bone with age," *Bone*, **22**:57-66 (1998).

193. Currey, J. D., K. Brear, and P. Zioupos, "The effects of ageing and changes in mineral content in degrading the toughness of human femora," *J. Biomech.*, **29**:257-60 (1996).

194. Melick, R. A., and D. R. Miller, "Variations of tensile strength of human cortical bone with age," *Clin. Sci.*, **30**:243-8 (1966).

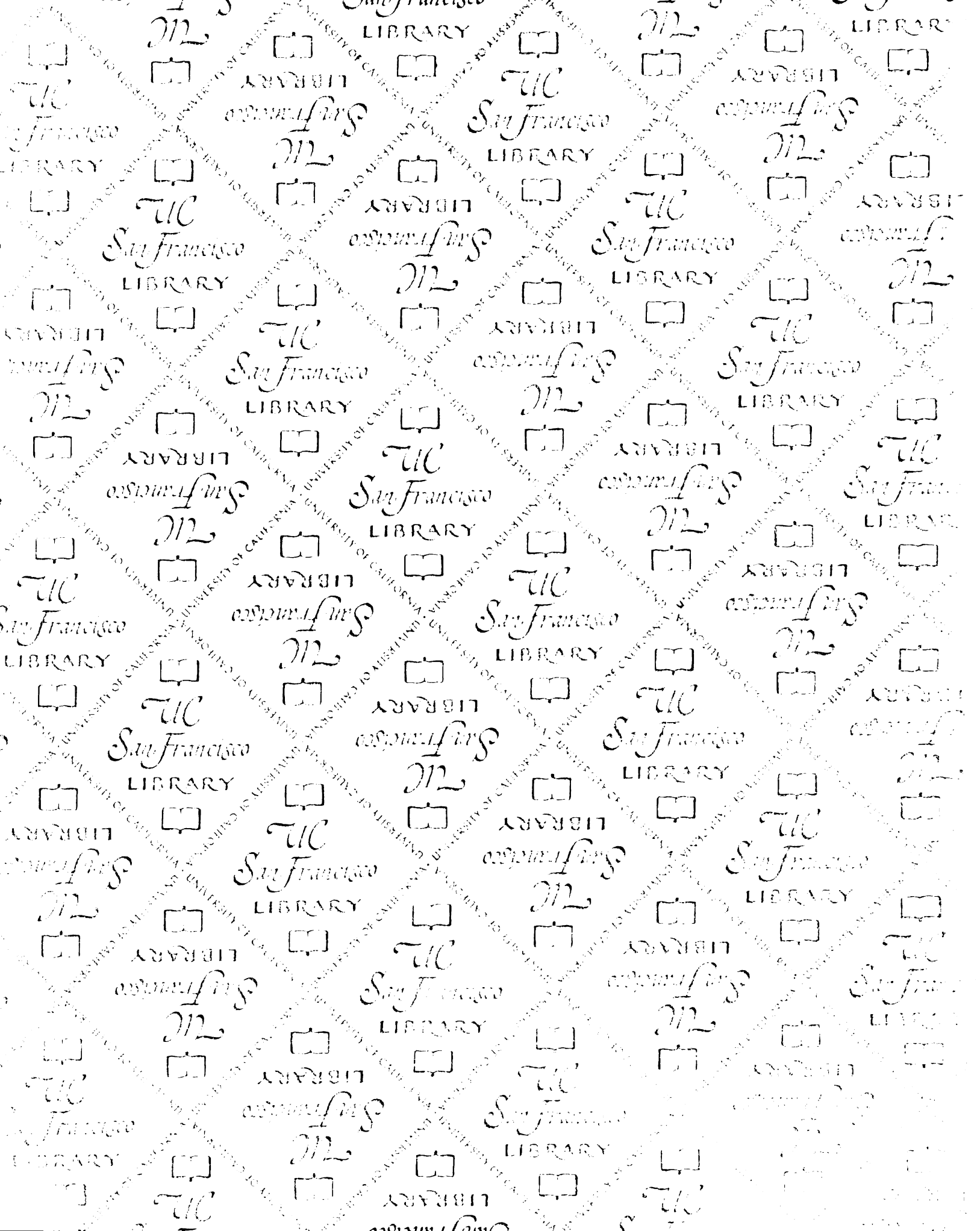
UC
San Francisco
LIBRARY
UNIVERSITY OF CALIFORNIA